Anisotropic Flow and Flow Fluctuations at the Large Hadron Collider

Anisotrope flow en flow schommelingen bij de grote hardronenbotser

Zhou, You

Publication date:
2016

Citation for published version (APA):
Zhou, Y. (2016). *Anisotropic Flow and Flow Fluctuations at the Large Hadron Collider: Anisotrope flow en flow schommelingen bij de grote hardronenbotser*. (Utrecht University ed.).
http://inspirehep.net/record/1429417/files/fulltext_Taaofw.pdf

Anisotropic Flow and Flow Fluctuations at the Large Hadron Collider

A catalogue record is available from the Utrecht University Library.

ISBN:

Typeset using LaTeX and printed by Ipskamp Drukkers, Enschede, The Netherlands.

Anisotropic Flow and flow fluctuations at the Large Hadron Collider

Anisotrope flow en flow schommelingen bij de grote hadronenbotser

(met een samenvatting in het Nederlands)

Proefschrift

ter verkrijging van de graad van doctor aan de Universiteit Utrecht op gezag van de rector magnificus, prof.dr. G.J. van der Zwaan, ingevolge het besluit van het college voor promoties in het openbaar te verdedigen op woensdag 6 januari 2016 des ochtends te 10.30 uur

DOOR

You Zhou

geboren op 24 juli 1985 te Jiangsu, P.R. China

Promotor: Prof. dr. R. Snellings

Co-promotor: Dr. P. Christakoglou

Dit werk is een onderdeel van het onderzoeksprogramma van de "Stichting voor Fundamenteel Onderzoek der Materie" (FOM), financieel gesteund door de "Nederlandse Organisatie voor Wetenschappelijk Onderzoek" (NWO), Grant number 680-47-217.

Contents

3

Chapter 1

Introduction

1.1 Quantum Chromodynamics

The Standard Model, is the theory that describes the elementary particles and their interactions. An integral part of the standard model is Quantum Chromodynamics (QCD) that describes the interactions between quarks and gluons, the building blocks of the ordinary matter. QCD is a non-Abelian theory that is represented by the SU(3) symmetry group. The carrier of the strong force is the gluon, a massless particle with spin 1, characterized by a new quantum number colour. There are two phenomena that one can only find in QCD: confinement and asymptotic freedom

Colour confinement refers to the fact that quarks and gluons cannot be isolated, and therefore cannot be observed directly [2]. Quarks are confined within colourless particles called hadrons: mesons are composed of quarks and antiquarks ($q\bar{q}$) and baryons are composed of three quarks (qqq or $\bar{q}\bar{q}\bar{q}$). The strong interaction is governed by:

$$V(r) = -\frac{4}{3}\frac{\alpha_s}{r} + \kappa r, \tag{1.1}$$

where α_s is the coupling strength, κ the string tension and r the distance between a quark and an antiquark. The second term shows that if this distance increases, the attractive force increases, preventing the isolation of quarks. This leads to the fact that all quarks are confined within hadrons, and one can not observe a free quark in nature. If the energy supplied to the $q, \bar{q}$ pair increases, at some point, it becomes energetically preferable for a new $q, \bar{q}$ pair to be created from the vacuum. These new quarks will, together with the existing $q, \bar{q}$ pair, create a new set of hadrons.

Asymptotic freedom on the other hand implies that at very short distances or large momentum transfers the coupling strength becomes asymptotically weaker [3]. The coupling strength α_s in QCD is not constant, and depends on the momentum transferred in the interaction according to:

$$\alpha_s \approx \frac{2\pi}{\beta_0 \ln(Q^2/\Lambda_{QCD})} \tag{1.2}$$

In this expression, $\beta_0 = 11 - \frac{2}{3}n_f$, and n_f is the number of active quark flavour, Q^2 the momentum transfer, Λ_{QCD} shows the characteristic energy scale of QCD. Figure 1.1 shows the Q dependence of α_s, as measured experimentally (see [4]).

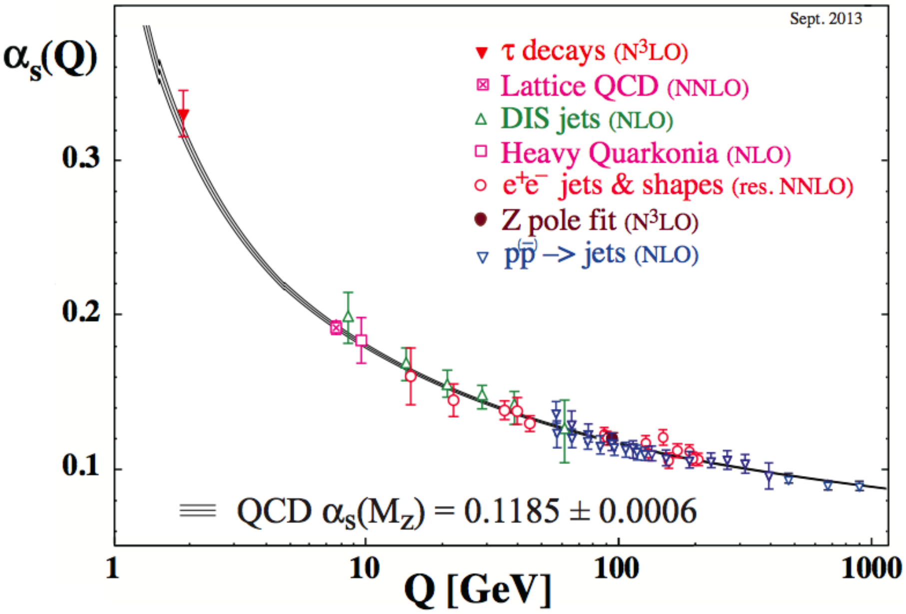

Figure 1.1: Summary of measurements of $\alpha_s(Q)$ as a function of the respective energy scale Q. Figure is taken from [4].

For large values of Q^2 (referred to as "hard collisions") we can use perturbative QCD (pQCD) calculations which provide testable predictions for processes occurring at short distances. However for small Q^2, one can only use numerical methods. Lattice QCD is such a well-established non-perturbative approach.

At ordinary temperatures and energy densities, normal matter is confined within a radius that corresponds to the QCD scale. At a sufficiently high temperature (energy), the hadrons start to "melt" into deconfined quarks and gluons. The new (colour) degrees of freedom are manifested by a rapid change of thermodynamic parameters such as energy density, or pressure with increasing temperature and as a consequent change in the equation of state (EoS) [174]. These expectations are indeed confirmed by Lattice QCD calculations. According to these calculations, at sufficient large temperatures and energy densities, one expects a transition from normal nuclear matter to a deconfined phase. This is illustrated in Figure 1.2 (left) which shows Lattice QCD calculations for the temperature T dependence of the pressure p, energy density ϵ and entropy density s, all divided by T^4. The plot indicates that around $T \sim 154$ MeV a rapid increase in all three normalized quantities takes place. This sudden rise is attributed to a transition from hadronic to deconfined matter. In addition, a rapid increase of the speed of sound $c_s^2(T)$ is observed in Fig. 1.2 (right), due to the fact that $c_s^2 = \frac{\partial P}{\partial \epsilon}$. At high temperatures, most of the thermodynamic parameters reach a significant fraction of the ideal massless

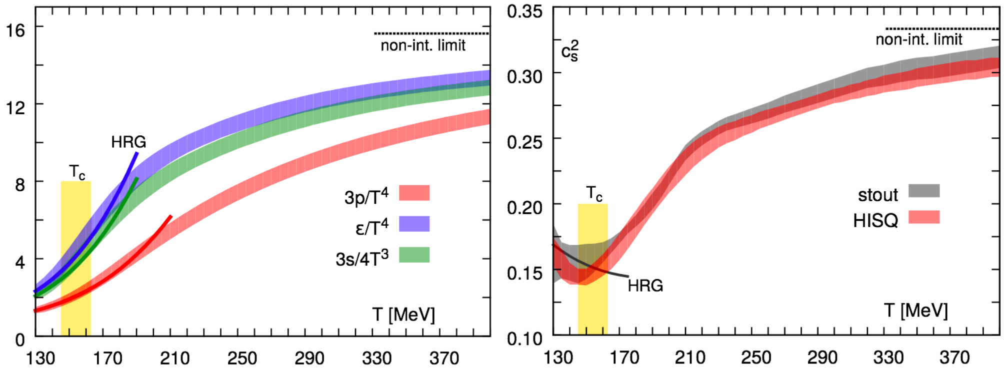

Figure 1.2: The energy density ϵ, pressure p, entropy density s (left) and the speed of sound squared $c_s^2(T)$ (right) normalised by T^4 as a function of the temperature. Figures are from [7].

gas limit of quarks and gluons, indicated by the arrow. This new state of matter at high temperatures is usually referred to as the quark-gluon plasma (QGP).

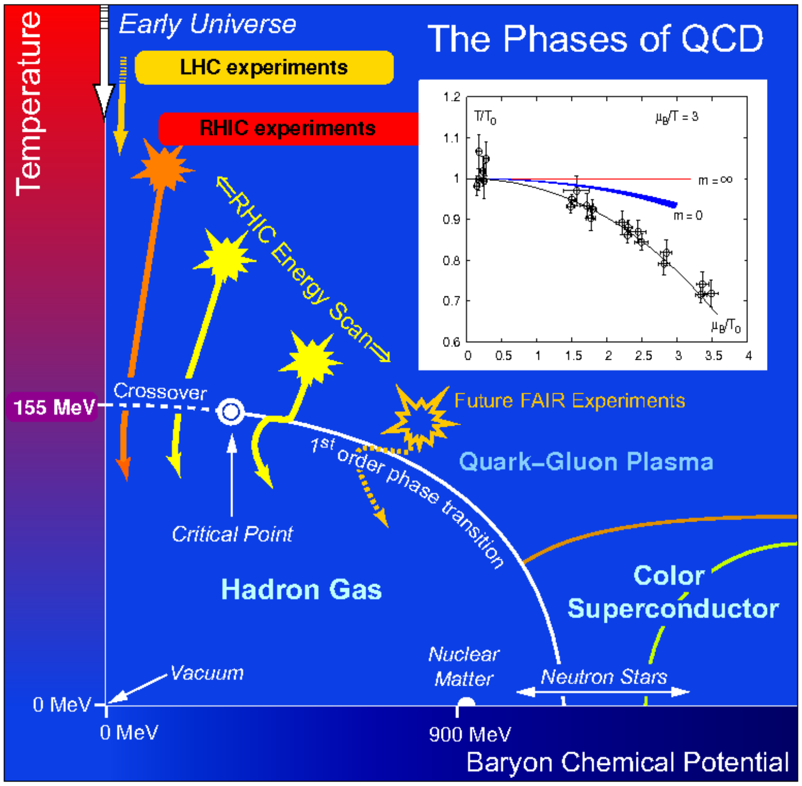

Figure 1.3: Schematic QCD phase diagram

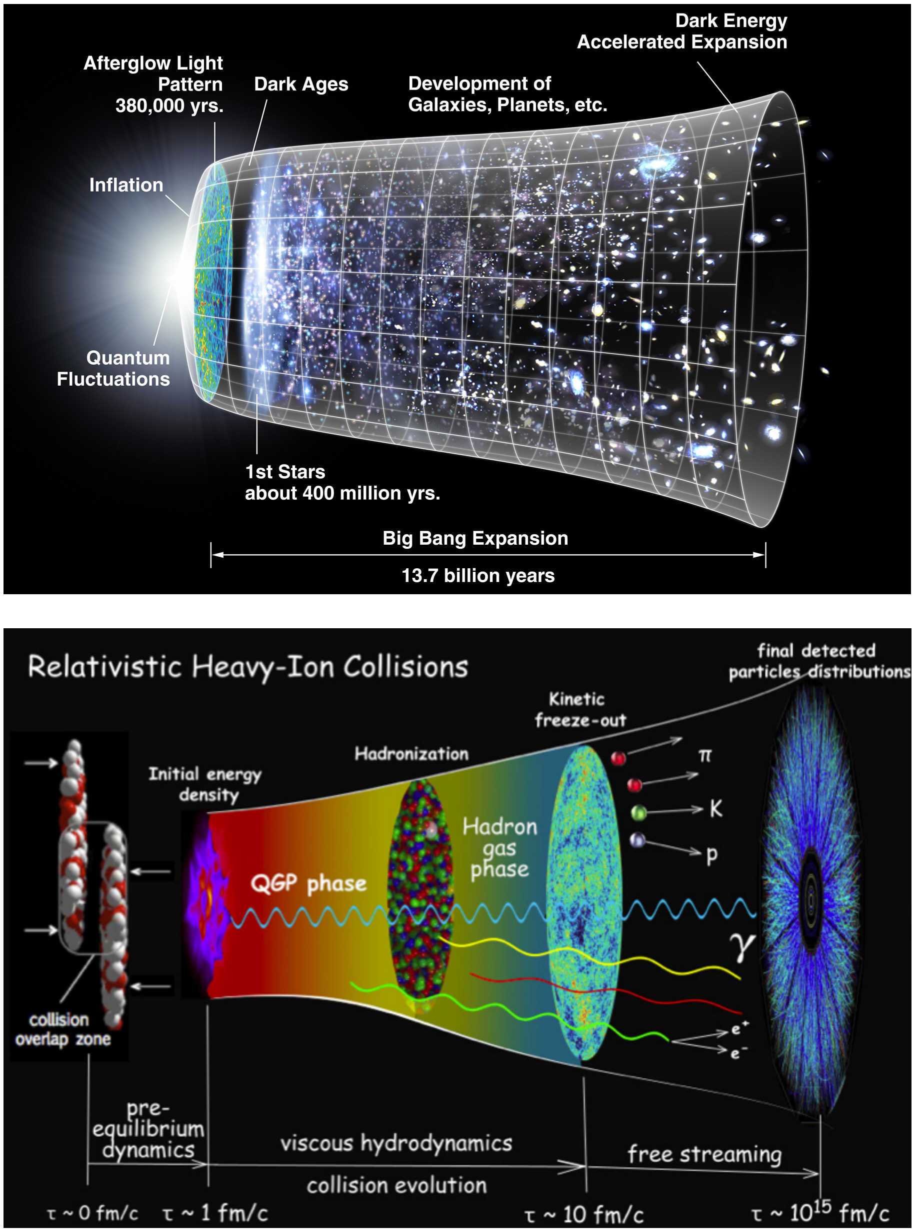

Figure 1.4: Illustration of the evolution of the Big Bang (top credit: NASA) and the Little Bang (bottom credit: Chun Shen)

1.2 Relativistic heavy-ion collisions

It is believed that the universe, a few micro-seconds after the Big-Bang, went through this state of matter, making its study of fundamental importance. As illustrated in Fig. 1.4 (top), the universe started from a single point, at approximately 13.8 billion years ago based on modern measurements [5,6], after which it expanded and cooled down. During this expansion a transition from a QGP phase to a hadronic phase happened, which allowed for the formation of hadrons.

To study this new state mater we collide heavy-ions at ultra-relativistic energies, where one creates QGP matter in the laboratory under controlled conditions. The study of heavy-ion collisions has been intense for more than three decades. Historically, it started with the Alternating Gradient Synchrotron (AGS) at energies $\approx$ 10 GeV/c per nucleon, superseded by the Super Proton Synchrotron (SPS) at roughly 17.2 GeV, followed by the Relativistic heavy-ion Collider (RHIC) with 200 GeV and up to 2.76 TeV at the Large Hadron Collider (LHC).

All these accelerator facilities, allowed scientists to map the phase diagram of QCD matter, shown in Fig. 1.3. This phase diagram is usually represented in the temperature versus baryon-chemical potential plane. At large baryon chemical potential a (first-order) phase transition between hadron gas and QGP phase is expected. During such a transformation of a thermodynamic system, similar to the transition between solid, liquid and gaseous states of matter, certain properties (e.g. temperature, density) of the system change discontinuously. This first-order phase transition might at smaller baryon-chemical potential end at a critical point. In the region below the critical point, the transition is expected to become continuous, usually referred to as a cross-over.

1.2.1 Experimental observables: Soft physics

As discussed before, the phase transition is expected to occur at $T_c \sim 154$ MeV, corresponding to an energy density of $\epsilon_c \approx$ 0.15-0.5 GeV/fm^3 [7], which could be already be achieved at RHIC and LHC energies. Therefore, experimental measurements in relativistic heavy-ion collisions could shed light on the properties of the QGP. The existence of this QGP phase can be probed with several experimental measurements. However, it has to be pointed out that no single measurement can be used as a 'smoking gun' signal of the phase transition. Therefore, one usually combines a number of measurements, compares them with theory calculations and reaches the corresponding physics conclusions. A few of the experimental measurements that contributed to our understanding of the system that is created in heavy-ion collisions are briefly presented in the next paragraphs.

Particle yields

The particle production in high-energy collisions has been found to be in approximate thermal and chemical equilibrium [10–12]. In central heavy-ion collisions, both light and strange flavour yields are determined by thermal parameters (e.g. chemical potential μ_B, chemical freeze-out temperature T_{ch}). Measurements at different collision energies revealed that the parameters extracted from thermal fits to particle yields (or the ratio

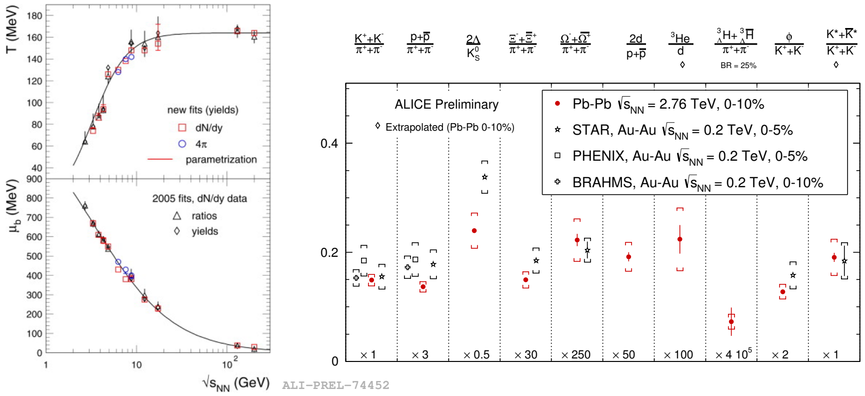

Figure 1.5: (Left) The energy dependence of temperature and baryon chemical potential at chemical freeze-out, from [9]. (Right) Particle ratios in Au–Au collisions at $\sqrt{s_{\mathrm{NN}}}$ = 200 GeV and at $\sqrt{s_{\mathrm{NN}}}$ = 2.76 TeV in Pb–Pb collisions, taken from [14].

of particle yields) follow smooth curves as a function of collision energy [9], see Fig. 1.9 (left). It is seen in Fig. 1.9 that the chemical potential μ_B decreases monotonically as a function of collisions energy $\sqrt{s_{\mathrm{NN}}}$. At the same time, the chemical freeze-out temperature increases from AGS to SPS energies, then saturates at $T \sim 160$ MeV where the collisions energy is relatively high and μ_B is rather small. This temperature is found to be very close to the critical temperature T_{C} predicted by Lattice QCD. Despite the successful description of experimental measurements (especially at RHIC) with thermal model fits, it remains unclear what the relation between the chemical freeze-out temperature and the QCD critical temperature is.

Thermal models successfully described the particle yields measured in Au–Au collision at top RHIC energy, with a fairly small $\chi^2/\mathrm{NDF} \approx 1$. At the LHC the description of particle ratios is quite successful. However, the observed low p/π ratio at the LHC, which is a factor of 1.5 lower than expectation, triggered a lot of discussions. This low p/π ratio could be understood as a consequence of a lower chemical freeze-out temperature ($T_{ch} \sim 140$ MeV), however, it also leads to a overestimation of K/π ratio by a similar large factor. More recently, it was realised that the consistency with equilibrium expectations is essentially restored if one includes the protons and K^* in the thermal fit [13]. A fit on the extended set of particle species with an equilibrium model gives a reasonably good description of particle ratios, with a $\chi^2/\mathrm{NDF} \approx 2$, slightly higher than what was obtained at RHIC, mainly due to the low p/π ratio [14]. One possible explanation for the difference between data and expectations of the thermal model is the annihilation of protons in the hadronic phase near the phase boundary [13]. However, several other mechanisms have also been proposed to better describe the yields measured at LHC, leading to significant different estimations of the chemical freeze-out temperature, T_{ch} that ranges from 130 to 165 MeV [14]. It is not clear yet which is the correct mechanism and how this chemical freeze-out temperature relates to the critical temperature in QCD phase transition. Thus, additional experimental measurements are needed to further constrain the particle production mechanisms.

Anisotropic flow

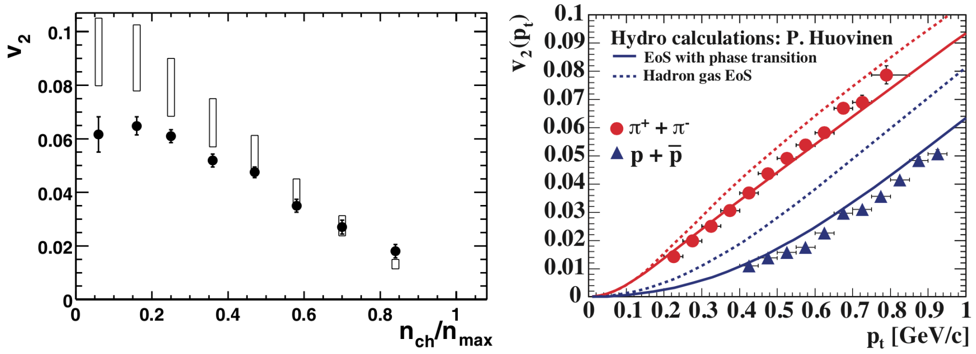

Figure 1.6: (Left) The elliptic flow of charged particles as a function of centrality (defined as $\mathrm{n_{ch}/n_{max}}$) in Au–Au collisions at $\sqrt{s_{\mathrm{NN}}} = 130$ GeV. The solid circles show the STAR data and the open rectangles show a range of v_2 values expected v_2 from the ideal hydrodynamic calculations. Figure is taken from [169]. (Right) v_2 of $\pi^{\pm}$ and $p(\bar{p})$ as function of transverse momentum. These calculations are compared to two scenarios of hydrodynamical model calculations, one with a hadron gas EoS and the other incorporating the QCD phase transition, which are presented by dashed and solid lines, respectively.

Prior to the heavy-ion runs at RHIC, it was a widely-held expectation that a weakly coupled system is formed in high-energy nuclear collisions. The created system would thermalise and behave like an ideal gas. However, the first measurement from RHIC did not support such expectation. The “elliptic flow” measurement, characterised by the second Fourier coefficient v_2 of the azimuthal angle particle distribution relative to the system's symmetry plane, which was surprisingly large [169], played a key role in this change. As illustrated in Fig. 1.6, the elliptic flow results were compatible with ideal hydrodynamic calculations, which in addition also nicely described the measured multiplicity and p_{T} spectra. This indicated that a strongly-coupled system was produced, and that the state of matter created in this system behaves more like a liquid instead of an ideal gas. Soon after the first measurements of the p_{T} integrated elliptic flow from the STAR Collaboration, the p_{T}-differential elliptic flow of charged particles [156] and identified particles [15] were reported by experiments at RHIC. In a (locally) thermalized system, like in hydrodynamics, the interplay between the radial expansion and anisotropic flow should lead to a specific dependence of the differential flow $v_2(p_{\mathrm{T}})$ on the mass of the particle [189]. Figure 1.6 (right) shows v_2 as function of p_{T} for $\pi^{\pm}$ and $p(\bar{p})$ at RHIC. As predicted by hydrodynamic calculations, the measured elliptic flow clearly depends on the mass of the particle at low p_{T}, v_2 at a fixed p_{T} decrease with increasing mass [15]. These results were quantitatively described by hydrodynamic calculations. Two different equations of state (EoS) were tested in early hydrodynamic calculations: a hadron gas EoS and an EoS with a phase transition from a QGP to a hadron gas. It was found that the calculation with an EoS incorporating the phase transition gives a better description of the data [189]. Later studies with $v_2(p_{\mathrm{T}})$ measurements of more particle species further confirmed the mass ordering observed at RHIC energies. These flow measurements not only strengthen the success of the hydrodynamic framework but also help to constrain the initial conditions,shear viscosity to entropy density ratio η/s (which depicts how 'perfect' the fluid is) and freeze-out conditions.

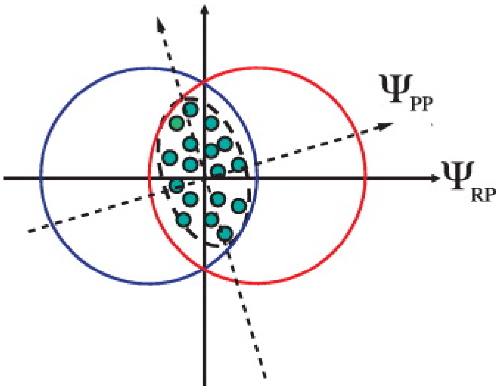

Figure 1.7: The sketch of Reaction Plane $\Psi_{\rm RP}$ and Participant Plane $\Psi_{\rm PP}$.

In addition, based on a Glauber calculations, it was realized that the geometry of the participant zone fluctuates, in terms of the value of the eccentricity as well as the orientation of the major axes, at fixed impact parameter [163]. The resulting anisotropy develops along the plane spanned by the minor axis of the participant zone and the beam direction, which is the so called participant plane, as depicted in Fig. 1.7. Two different definitions of the initial eccentricity were proposed: the 'original' eccentricity from the reaction plane $\varepsilon_{\rm RP}$ (or $\varepsilon_{\rm std}$), is defined by the almond shape of the spatial overlap region, calculated as $\varepsilon_{\rm RP} = \frac{y^2-x^2}{y^2+x^2}$, here $\langle\,\rangle$ denotes the average over the coordinates of the participants in a given event. On the other hand, the eccentricity determined by the participants is denoted as $\varepsilon_{\rm PP}$ (or ε_2), it is calculated via $\varepsilon_{\rm PP} = \frac{\sigma_y^2-\sigma_x^2}{\sigma_y^2+\sigma_x^2}$, here $\sigma_x = \langle x^2\rangle - \langle x\rangle^2$ and $\sigma_y = \langle y^2\rangle - \langle y\rangle^2$. If v_2 originates from $\varepsilon_{\rm RP}$, then a smaller v_2 was expected to be observed in Cu–Cu collisions which has smaller initial $\varepsilon_{\rm RP}$ compared to Au–Au collisions. In contrast, a large v_2 was measured [163], which revealed that it is the participant eccentricity ε_2, not the standard eccentricity $\varepsilon_{\rm RP}$, that is responsible for the development of elliptic flow. The strong geometry fluctuations in the initial state of Cu–Cu collisions generate a larger ε_2 and lead to the large v_2 measured in experiments. It was also noticed that the information on eccentricity fluctuations was not washed out, but survived during the system evolution, which might already indicate small viscous corrections. Monte Carlo studies [89] and subsequent measurements [24, 198] further confirmed that the initial geometry of the overlap region fluctuates event-by-event, leading to final state flow fluctuations. The initial state eccentricity fluctuations and final state flow fluctuations were investigated in detail when the 2- and multi-particle correlations, which have different sensitivities to fluctuations, became widely used [26–28].

The importance of incorporating viscosity into the hydrodynamic calculations was never completely ignored but was not taken into account, due to the successes of ideal

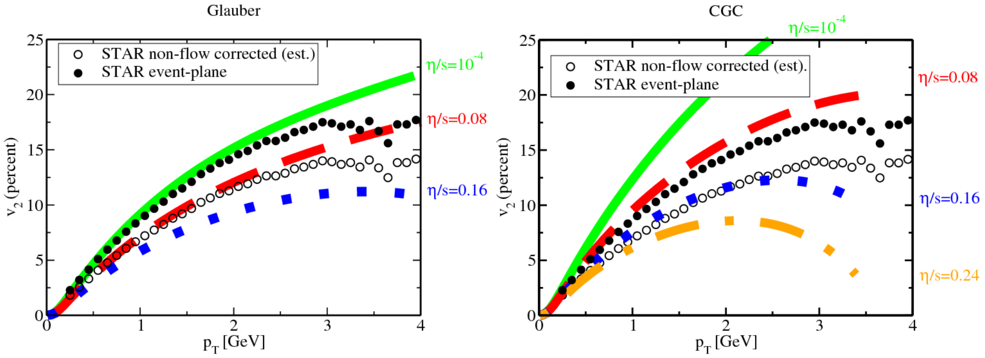

Figure 1.8: The comparisons of $v_2(p_T)$ from data and hydrodynamic calculations with (left) Glauber initial conditions and $\eta/s = 0.08$; (right) CGC initial conditions and $\eta/s = 0.16$.

hydrodynamic calculations and the lack of a formalism to incorporate the viscosity into practical hydrodynamic calculations. At a later stage, studies within the AdS/CFT correspondence, conjectured that the value of shear viscosity over entropy ratio has a lower bound. This is known as the Kovtum-Son-Starinets (KSS) lower bound of $1/4\pi$ [186]. This triggered further developments in the field of hydrodynamic calculations. Since 2008, such calculations quantitatively described the experimental $v_2(p_T)$ measurements [19, 148], using Glauber initial conditions and $\eta/s = 0.08$ or CGC initial conditions with $\eta/s = 0.16$, as presented in Fig. 1.8. Despite the good agreement between data and theoretical calculations, it needs to be pointed out that there is big uncertainty in the extracted η/s arising from the limited knowledge of initial conditions. Thus, better understanding of the initial conditions (its geometry as well as its fluctuations) are key to obtain precise transport properties like η/s.

In addition, the initial geometry fluctuations not only generate large flow fluctuations, but also non-zero value of odd Fourier harmonics, such as v_3 and v_5, which are expected to vanish in collisions of symmetric systems [161]. The first measurements of higher harmonic anisotropic flow were published in 2011 by ALICE [122]. Finite magnitudes of v_3, v_4 and v_5 were observed, and their contributions can be used to naturally explain the “double peak” structure of di-hadron correlations. In addition, the higher harmonic anisotropic flow coefficients were found to be more sensitive to η/s, which leads to additional strong constrains on the η/s in hydrodynamic calculations. It was found in 2012 that hydrodynamic calculations incorporating subhadronic quantum fluctuations [21] not only are in an excellent agreement with the precise anisotropic flow measurements for p_T-differential v_2, v_3, v_4 simultaneously [22] but also reproduce the event-by-event distributions of v_2, v_3, v_4 measured by the ATLAS Collaboration [23].

So far, the hydrodynamic framework is well supported by experimental data and widely accepted. It is believed that with Run2 at LHC and BES-II at RHIC, the high statistics data of heavy-ion collisions with help us to better determine the temperature dependent η/s, measure the bulk viscosity (which was assumed to be fairly small compared to the shear viscosity) and constrain both the initial state and its fluctuations. The latest results on anisotropic flow and flow fluctuations measurements at the LHC

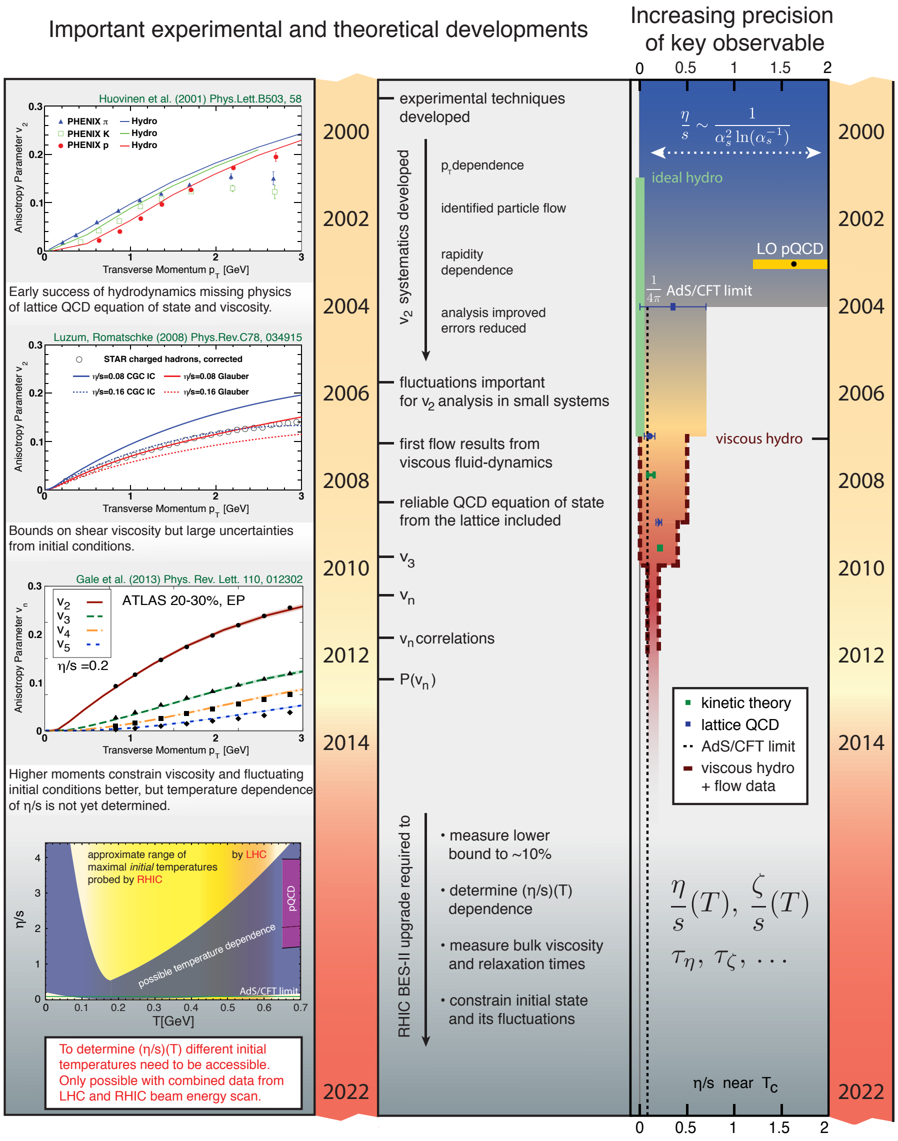

Figure 1.9: Timeline of both experimental and theoretical developments for the precise understanding of flow, properties of the quark-gluon plasma (like η/s), and the initial state and its fluctuations. Figure is from [29].

will be presented in this thesis.

1.2.2 Experimental observable: Hard probes

Nuclear modification factor R_{AA}

The study of the high p_{T} region brings new knowledge about the properties of the produced hot and dense matter in heavy-ion collisions. In pp collisions, hard scattered partons (quarks and gluons) fragment into jets of hadrons. In heavy-ion collisions, the hard scattering occurs before the formation of QGP, thus the scattered partons will experience the entire evolution of the system created in these collisions [30]. These partons interact strongly with the medium, leading to an attenuation of their energy, known as "jet quenching" [31]. It was proposed that the energy loss is stronger in a medium of deconfined matter than in hadronic matter, which makes the "jet quenching" a potential signature of the existence of the QGP [31].

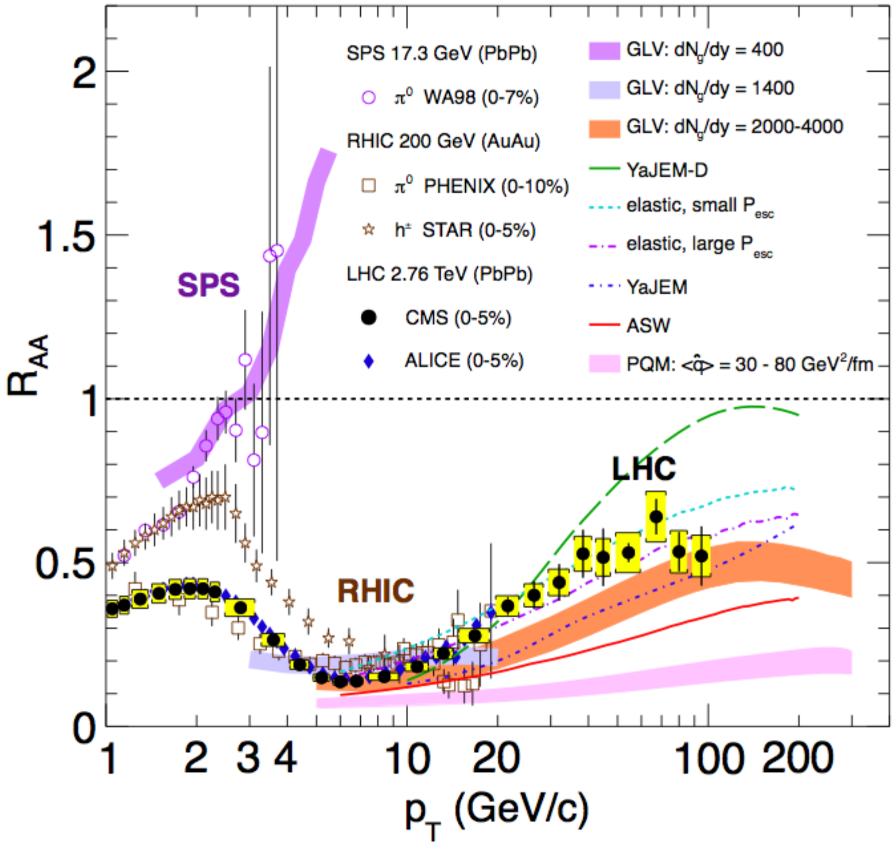

Figure 1.10: Transverse momentum dependence of nuclear modification factor R_{AA} for charged particles produced in central heavy-ion collisions at SPS, RHIC and LHC. Figure is from [42].

First evidence of the energy loss of partons was observed with the suppression of high p_{T} particle yields via the nuclear modification factor, defined as:

$$R_{\mathrm{AA}}(p_{\mathrm{T}}) = \frac{\mathrm{d}N_{ch}^{AA}(p_{\mathrm{T}})/\mathrm{d}p_{\mathrm{T}}}{\langle N_{coll}\rangle\,\mathrm{d}N_{ch}^{pp}(p_{\mathrm{T}})/\mathrm{d}p_{\mathrm{T}}} \tag{1.3}$$

where the superscripts AA and pp refer to the results obtained in heavy-ion and pp collisions, respectively, the $\mathrm{d}N_{ch}(p_{\mathrm{T}})$ represent the number of charged particles measured in certain kinematic range (p_{T}). In order to compare the yield of high p_{T} charged particles produced in AA and pp collisions, a scaling factor, the number of binary collisions N_{coll} calculated within the Glauber model, is needed to provide a proper normalisation for a given AA centrality. If a heavy-ion collision can be regarded as a simple superposition of N_{coll} nucleon-nucleon collisions (in which case nuclear modifications are absent), the ratio R_{AA} will be unity, whereas any deviation from unity will indicate a medium effect.

It is seen in Fig. 1.10 that at the SPS, the R_{AA} was slightly lower than unity for $2 < p_{\mathrm{T}} < 3$ GeV/c and then reaches unity for higher p_{T} [32]. However, at RHIC energy, R_{AA} increases monotonically reaches a maximum around $p_{\mathrm{T}} \sim 3$ GeV/c and then decreases. Hadron production for $6 < p_{\mathrm{T}} < 8$ GeV/c is suppressed by a factor of 4-5 in central Au–Au relative to pp collisions [33,34]. In 2010, the ALICE Collaboration published the first charged particle R_{AA} measurements at the LHC [35], extracted from the p_{T} spectra up to 20 GeV/c in 0-5% most central collisions. Compared to the measurements at lower energy heavy-ion collisions at RHIC, a slightly stronger suppression was reported: about a factor of 7 observed for the p_{T} range around 6∼7 GeV/c at LHC. This is followed by a progressive increase of R_{AA} with increasing p_{T}. This observation was confirmed by CMS measurements [36], which extended the p_{T} range up to 100 GeV/c. The R_{AA} measurements exhibit a clear increasing trend up to $p_{\mathrm{T}} \sim 40$ GeV/c and then seems to saturate with a R_{AA} value of about 0.5 to 0.6. The R_{AA} measurements in the other centrality classes were also reported by both the ALICE and CMS experiments. As expected, less suppression was observed when moving from central to peripheral Pb–Pb collisions, indicating weaker nuclear effects compared to central collisions.

Various model calculations have also been presented in the same figure [37–41], most of which can fairly well reproduce the R_{AA} measurements. However, it remains to be demonstrated whether these calculations can describe the measurements at different energies using the same set of parameters, and whether they can quantitatively reproduce other measurements at high p_{T} simultaneously.

Chapter 2

Experimental Setup

The main work presented in this thesis is based on the data recorded by A Large Ion Collider Experiment (ALICE) at the Large Hadron Collider (LHC).

2.1 Large Hadron Collider

The Large Hadron Collider (LHC) is the highest-energy particle collider ever constructed and is considered as one of the great engineering milestones of mankind. It was built at the European Organization for Nuclear Research (CERN) in Geneva to allowe physicists to test the predictions of different theories of high-energy physics, in particular to prove or disprove the existence of the theorized Higgs boson, which is pivotal to the Standard Model. After the first start up on 10 September 2008, LHC delivered proton–proton ($\sqrt{s_{\mathrm{NN}}}$ = 900 GeV, 2.36 TeV, 7 TeV and 8 TeV centre of mass), lead–lead ($\sqrt{s_{\mathrm{NN}}}$ = 2.76 TeV) and proton–lead ($\sqrt{s_{\mathrm{NN}}}$ = 5.02 TeV) for different physics purposes.

The LHC consists of a 27-kilometer ring of superconducting magnets with a number of accelerating structures to boost the energy of particles along the way (see Fig. 2.1). Two colliding particle beams travel in opposite directions in separate beam pipes, at the speed of $0.999999991c$ at $\sqrt{s_{\mathrm{NN}}}$ = 7 TeV before they are made to collide. The beams are guided by 1232 dipole magnets which are 15 meters in length and are focused by 392 quadrupole magnets, each 57 meters long. They circulate inside the LHC and make collisions at four locations around the accelerator ring, corresponding to the positions of four particle detectors – A Toroidal LHC ApparatuS (ATLAS) [66], Compact Muon Solenoid (CMS) [67], Large Hadron Collider beauty (LHCb) [68] and A Large Ion Collider Experiment (ALICE) [65]. The first two are general purpose detectors used to look for signs of new physics, including the origins of mass of elementary particles and extra dimensions. LHCb is a specialized b–physics experiment whose goal is to investigate the parameters of CP violation in the interactions of b-hadrons. The ALICE detector is designed to study the properties of the so called quark gluon plasma (QGP) which is believed to have been created in the first microseconds after the Big Bang. Details will be discussed in the following chapter.

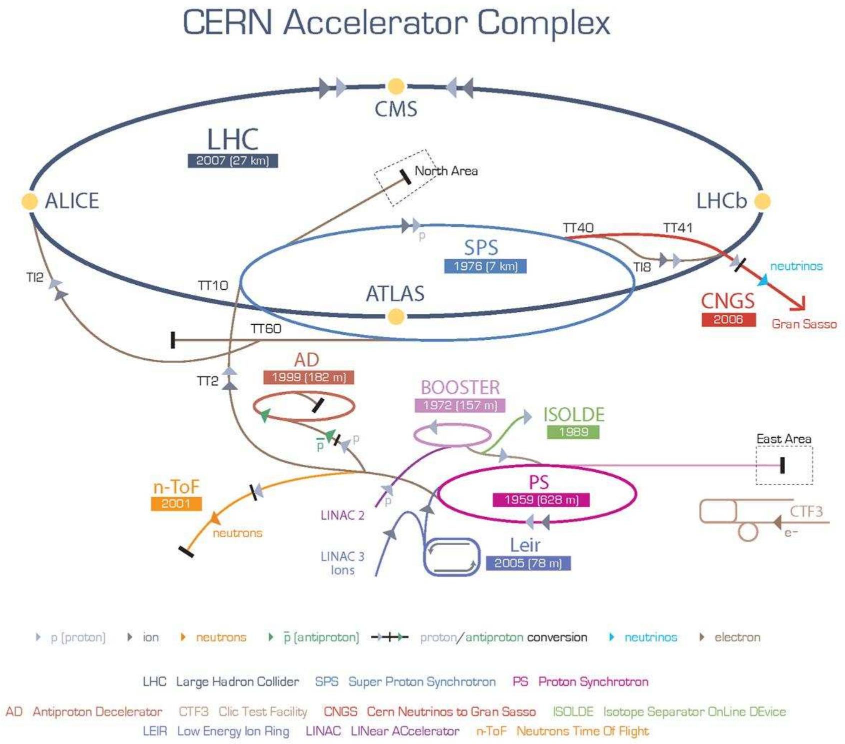

Figure 2.1: Large Hadron Collider

2.2 A Large Ion Collider Experiment (ALICE)

ALICE is a general-purpose, heavy-ion detector at the CERN LHC which is dedicated to study QCD, the strong interaction sector of the Standard Model. The main motivation is to study the properties of the hot and dense matter, the QGP, produced in heavy ion collision with the ALICE experiment. It will help people to understand the physics of the deconfined state of matter which existed until a few microseconds after the Big Bang, with comprehensive studies like Anisotropic Flow, Jets Quenching *et. al.*. The ALICE detector is optimized for tracking and identifying charged particles at midrapidity for a broad range of transverse momenta, from 100 MeV/c to 100 GeV/c. It works in a very high multiplicity environment, where the charged particle multiplicity was expected to be in the range from $dN/d\eta = 2000$ up to almost $dN/d\eta = 8000$ in central Pb–Pb collisions.

The overall dimensions of ALICE detector are $16 \times 16 \times 26\text{m}^3$, it weights approximately 10 000 tons. It consists of a central barrel part, which is placed inside of a large solenoid magnet, reused from the L3 experiment at LEP, with full azimuthal coverage at

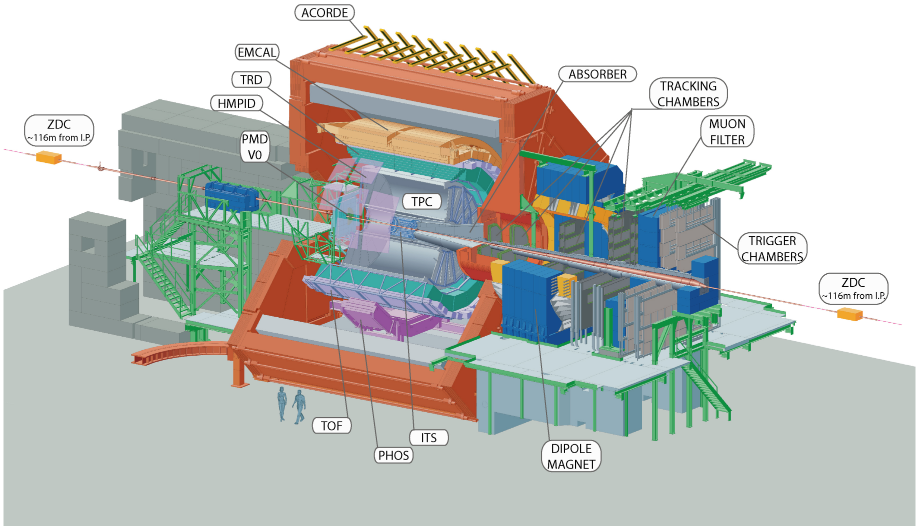

Figure 2.2: ALICE detector.

pseudorapidity $-0.9 < \eta < +0.9$ and a forward muon spectrometer. The ALICE detector contains many sub-detectors, from the inside out, they are the Inner Tracking System (ITS), the cylindrical Time-Projection Chamber (TPC), the Time-of-Flight (TOF), the Ring Imaging Cherenkov (HMPID), the Transition Radiation (TRD) detectors, the electromagnetic calorimeters which are the PHOS and the EMCal and several smaller detectors (ZDC, PMD, FMD, T0, V0). In this thesis, we discuss the sub-detectors system ITS, TPC, TOF, V0 which we used in the analysis. More details about ALICE detector can be found in [77].

2.2.1 Inner Tracking System (ITS)

The ALICE Inner Tracking System [77,80] is placed inside the inner TPC radius and it is the ALICE detector closest to the beam axis. The ITS is composed of 6 cylindrical layers with 3 different technologies, 2 innermost layers of Silicon Pixel Detectors (SPD), 2 layers of Silicon Drift Detectors (SDD) and 2 outermost layers of Silicon Strip Detectors (SSD), see Fig 2.3. The general information on the six silicon detector layers of the ITS can be found in Table. 2.1.

The main purpose of the ITS is the determination of the primary vertex with a resolution better than 100 μm and of the secondary vertices necessary for the reconstruction of hyperon and charm decays. It is also used as a standalone tracker in order to recover tracks that are not reconstructed by the TPC (for instance tracks crossing the dead regions in the TPC) and to reconstruct low momentum particles with p_{T} down to 100 MeV/c. In addition, the ITS provides particle identification performed by measuring

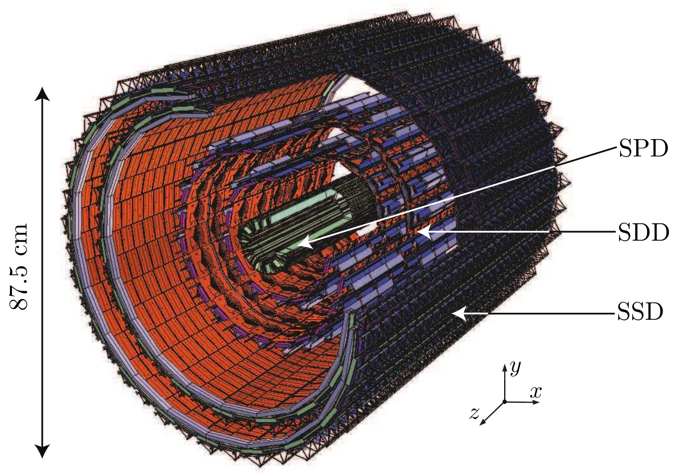

Figure 2.3: ALICE's Inner Tracking System (ITS), includes Silicon Pixel Detector (SPD), Silicon Drift Detector (SDD) and Silicon Strip Detector (SSD).

Table 2.1: Dimensions of the ITS detectors.

Layer	Type	r (cm)	$\pm z$ (cm)
1	pixel	3.9	14.1
2	pixel	7.6	14.1
3	drift	15.0	22.2
4	drift	23.9	29.7
5	strip	38.0	43.1
6	strip	43.0	48.9

the energy loss signal with a resolution of about 13 % in the the 4 outer most layers (SDD and SSD), see Fig. 2.4 (left). It also allows us to improve the momentum and angular resolution for particles reconstructed in the Time-Projection Chamber (TPC), by providing additional track points in the direction of the interaction vertex. Furthermore, reconstructing tracklets with the innermost layers of the SPD can be used for the determination of the collision centrality, with a resolution of about 0.5 % centrality bin width in the most central collisions, see Fig. 2.4 (right). Thus, the ITS contributes to practically all physics topics addressed by the ALICE experiment, as discussed in detail in [77].

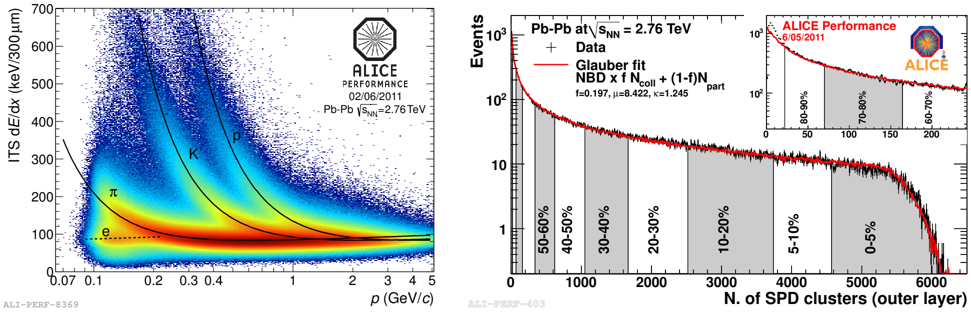

Figure 2.4: Energy loss of charged particles in PbPb collisions vs their momentum in ITS (left). Centrality determination via number of SPD clusters in ITS.

2.2.2 Time Projection Chamber (TPC)

The Time Projection Chamber (TPC) [77,78] is the main tracking detector of the central barrel. Combined with the ITS and TRD, it provides the charged particles momentum measurements with good two-track separation. The TPC also provides excellent measurements of charged particle energy loss (dE/dx) and momentum p, simultaneously. These two measurements can be used for particle identification (PID), using the Bethe-Bloch formula. Figure 2.6 illustrates energy loss vs p as measured by the ALICE TPC with the Bethe-Bloch parameterisation curves in black lines. It is also used to determine the collision vertex in the high multiplicity environment of heavy ion collisions. In addition, the TPC can also be used as a centrality estimator with a resolution of about 0.5 % centrality percentile width in the most central collisions [136], see Fig. 2.6 (right).

The TPC covers a pseudo-rapidity range of $|\eta|< 0.9$ for full track length within the TPC volume (the range also covered by the ITS, TRD and TOF detectors). It also provides full azimuthal coverage except for the dead zones in the TPC, this makes the TPC an ideal detector for anisotropic flow analysis, since these inefficiencies in the detector's azimuthal acceptance would result in non-negligible systematic biases for the azimuthal angle correlations analysis.

2.2.3 Time Of Flight (TOF)

The Time-Of-Flight detector [77,82] is a large area array covering a cylindrical surface of 141 m^2 with an inner radius of 3.7 m, a pseudo-rapidity interval $\eta|<0.9$ and full azimuthal coverage (important for anisotropic flow analysis). The TOF exploits the innovative Multi-gap Resistive Plate Chamber (MRPC) technology, capable of an intrinsic time resolution better than 50 ps with an efficiency close to 100% and a large operational plateau. The whole system is made of 1593 MRPCs arranged into 90 gastight modules which are grouped into 18 SuperModules (SM) each covering an azimuthal angle of 20 degrees.

The main purpose of the TOF is the particle identification in the intermediate momentum range, where the energy loss signal for pions, kaons and protons can not be

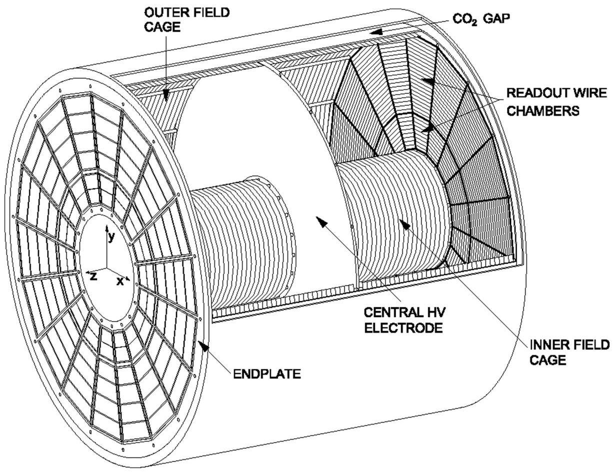

Figure 2.5: ALICE's Time Projection Chamber (TPC).

easily separated in the TPC. The time measurement from the TOF, in conjunction with the momentum and track length measured by the tracking detectors is used to calculate the particle mass. The TOF PID works up to about 2.5 GeV/c for pions and kaons, and up to 4 GeV/c for protons. A time resolution of 100 ps will provide 3σ π/K separation up to 2.2 GeV/c and K/p separation up to 4 GeV/c [83]. In fig. 2.8 is plotted β measured with the TOF as a function of momentum p, for Pb-Pb collisions at $\sqrt{s_{\mathrm{NN}}}$= 2.76 TeV. The different particle species are clearly visible. We will discuss the particle identification with more details in the next chapter.

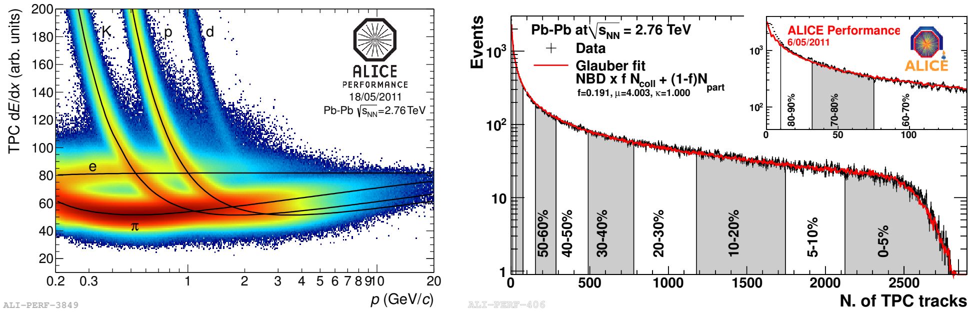

Figure 2.6: Energy loss of charged particles vs their momentum in Pb–Pb collisions in TPC (left). Centrality determination via number of tracks in TPC.

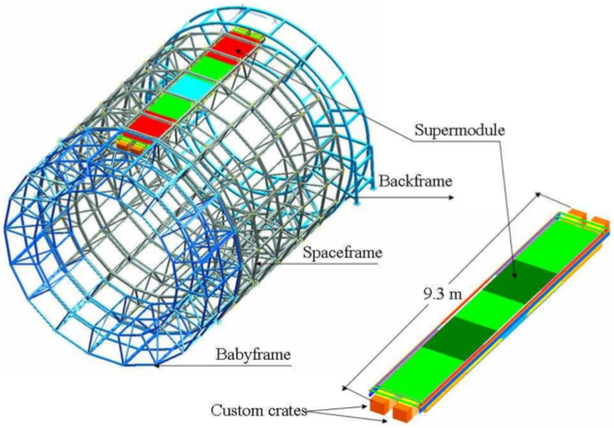

Figure 2.7: schematic view of the Time-Of-Flight detector (TOF).

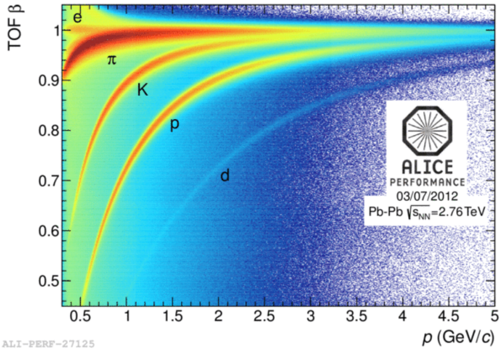

Figure 2.8: TOF measured β as a function of momentum

2.2.4 VZERO

The VZERO detector [77,84] is located in the forward rapidity region inside of the main magnet. It is composed of two arrays of scintillator counters, VZERO-A and VZERO-C, which cover the pseudorapidity ranges $2.8<\eta<5.1$ and $-3.7<\eta<-1.7$, respectively. Each of the VZERO arrays is segmented in four rings in the radial direction, and each ring is divided in eight sections in the azimuthal direction. They are segmented into 32 individual counters each distributed in four rings.

One of the primary roles of the VZERO system is to provide minimum bias (MB) triggers for both pp and Pb–Pb collisions. Besides, the VZERO system provides the integrated beam luminosity and the charged particle multiplicity measurement based on the energy deposited in the scintillators. Figure 2.10 (left) shows the distribution of the sum of amplitudes in the VZERO scintillators. The distribution is fitted with the

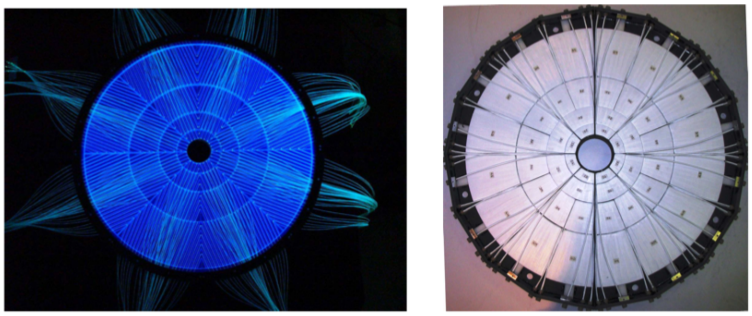

Figure 2.9: Front view of V0A (left) and V0C (right) arrays

Negative Binomial Distribution Glauber (NBD-Glauber) model fit shown as a line (the inset shows a zoom of the most peripheral region). The VZERO detector is chose as a centrality determination in the ALICE experiment since it gives the best resolution over the inspected centrality range, see Fig. 2.10 (right). Furthermore, the VZERO system can be used to reconstruct the event plane. The second harmonic event plane resolution $\mathscr{R}_2$ of VZERO-A and VZERO-C arrays as a function of centrality percentile is shown in Fig. 2.10 (right). More details about the Event Plane method and the VZERO performance can be found in Chapter 5.

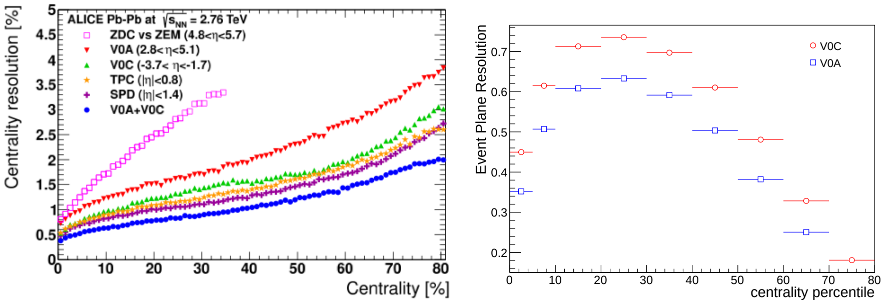

Figure 2.10: Centrality resolutions for all the estimators (left); second harmonic event plane resolution $\mathscr{R}_2$ of VZERO-A and VZERO-C arrays as a function of centrality percentile (right).

2.3 ALICE Framework

The ALICE offline framework [43,129,130], AliRoot , illustrated schematically in Fig. 2.11, provides common tools for processing of the ALICE data in an efficient way. Its implementation is based on Object-Oriented techniques for programming and designed to take advantage of the existing technologies for parallel computing. Complemented by the AliEn system, physicists get access to the computing GRID, a world-wide network of computing centers which consists of about 48k CPUs for ALICE Collaboration. The framework consists of several modules providing software for simulation, alignment, calibration, reconstruction, visualization and analysis of the experimental data.

Concerning the analysis presented in this thesis, a special framework, named the FLOW package, has been used. This package supplies an additional level of abstraction between the most popular flow analysis methods and the data source, be it ALICE reconstructed data, simulations or data coming from a different source entirely like toy models or data from other experiments. It allows simplified development of analysis methods as the developer only uses a transparent interface without the need to deal with detector specific details.

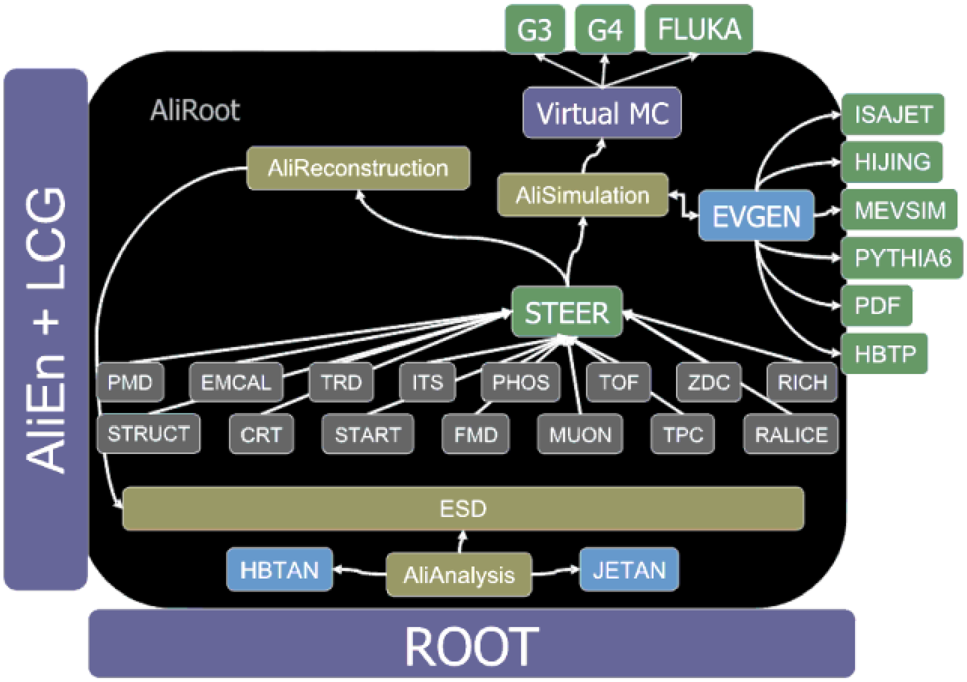

Figure 2.11: AliRoot framework

Chapter 3

Analysis Details

In this chapter we discuss the data sample and the event and track level selections applied in this analysis. The analyzed data samples were collected by the ALICE detector during the first Pb–Pb run at a center-of-mass energy $\sqrt{s_{\mathrm{NN}}} = 2.76$ TeV and during the p–Pb run at a center-of-mass energy $\sqrt{s_{\mathrm{NN}}} = 5.02$ TeV at the Large Hadron Collider.

3.1 Event Selection

3.1.1 Online and Offline Event Selection

Minimum bias Pb–Pb events were triggered by the coincidence of signals from the two V0 detectors. An additional offline selection was applied to reduce the number of beam-gas events, using the V0 timing information and the requirement of two tracks in the central detector. Electromagnetic interactions were removed by requiring an energy deposition above 500 GeV in each of the ZDCs [209].

The primary vertex position in ALICE is determined using the tracks reconstructed by the TPC or by the global tracking. The z position of the primary vertex is required to be within $|\mathrm{Vertex}_{\mathrm{z}}| < 10$ cm, chosen to ensure a uniform acceptance and reconstruction efficiency in the mid pseudo-rapidity region $|\eta| < 0.8$.

Further event selection, based on the study of the correlation between the multiplicity of tracks reconstructed using both the ITS and the TPC and the multiplicity obtained using TPC tracks are used to reject the pile-up events [1]. Figure 3.1 shows the correlation between the multiplicity measured by the TPC and the one measured with the combined ITS and TPC tracking. The left plot shows that some background events are clearly located outside of the correlation band. After applying pileup cuts, a clean sample was obtained which shows a linear correlation of the multiplicity from Global tracks and TPC only tracks (shown in Fig. 3.1 right).

The minimum bias p–Pb events were also triggered by the coincidence of signals for the two V0 detectors. The collision-vertex position is determined with tracks recon-

---

[1] There is a non-negligible probability that one single bunch crossing may produce several separate events, called pile-up events

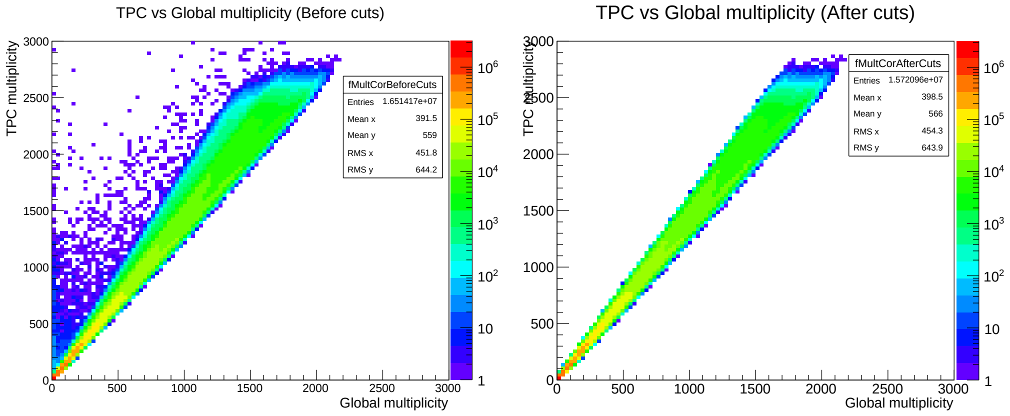

Figure 3.1: TPC multiplicity $v.s$ Global multiplicity (left) before and (right) after the pileup cuts.

structed in the ITS and TPC as described in [192]. The position of the reconstructed vertex along the beam direction is required to be $|\mathrm{Vertex_z}| < 10$ cm.

About 16 million minimum bias Pb–Pb events and 100 million p–Pb events which pass the above event selection criteria are used for the analysis in this thesis.

3.1.2 Centrality Determination

In heavy-ion collisions, the measurements are often presented in centrality classes. Ideally the centrality can be determined by the impact parameter b, the number of participating nucleons $\langle N_{part}\rangle$ (nucleons which undergo at least one AA collision) or the number of binary nucleon-nucleon collisions $\langle N_{coll}\rangle$. However, none of these quantities are known in experiments.

Experimentally, the centrality is defined as the percentile of the hadronic cross section corresponding to a particle multiplicity above a give threshold (N_{ch}):

$$c \approx \frac{1}{\sigma_{AA}} \int_{N_{ch}}^{\infty} \frac{\mathrm{d}\sigma}{\mathrm{d}N_{ch}^{'}} N_{ch}^{'}, \tag{3.1}$$

In Eq. 3.1 the cross-section can be replaced by the number of measured events n, corrected for the trigger efficiency and for the non-hadronic interaction background,

$$c \approx \frac{1}{N_{ev}} \int_{N_{ch}}^{\infty} \frac{\mathrm{d}n}{\mathrm{d}N_{ch}^{'}\mathrm{d}} N_{ch}^{'} \tag{3.2}$$

Here we assume that the particle multiplicity at mid rapidity increase monotonically with the centrality (or size of the overlap region in AA collisions). The charged particle multiplicity distributions could be obtained via the V0 amplitude (sum of V0-A and V0-C amplidudes) in ALICE, which is presented in Fig. 3.2. Within the framework of the

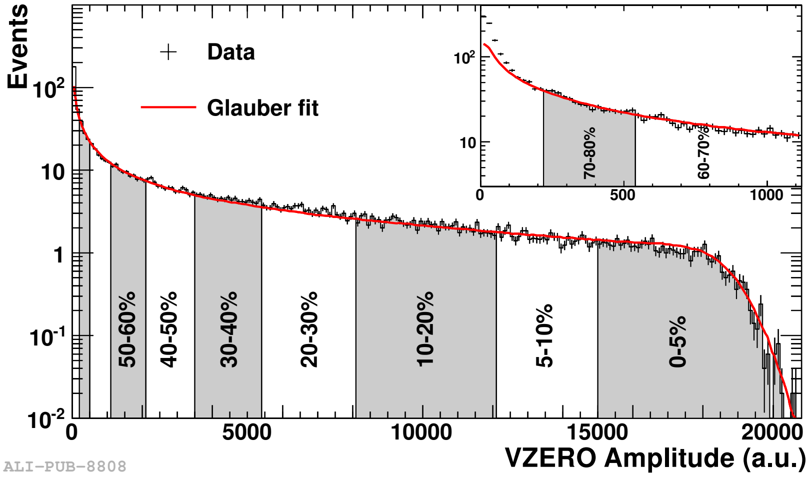

Figure 3.2: Distribution of the summed amplitudes in the V0 scintillator tiles (histogram); inset shows the low amplitude part of the distribution. The curve shows the result of the Glauber model fit to the measurement. The vertical lines separate the centrality classes used in the analysis, which in total correspond to the most central 80 % of hadronic collisions.

Glauber model, the particle production (multiplicity distributions) could be described using the two component model, which decomposes the nucleus–nucleus collisions into soft (probability proportional to N_{part}) and hard (probability proportional to N_{coll}) interactions. Each source is weighted with a factor f and its contributions is a random number of particles distributed according to the Negative Binomial Distribution (NBD) characterised by two parameters μ and κ. Then the multiplicity distributions shown in Fig. 3.2 are fitted by $fN_{part} + (1 - f)N_{coll}$ with this Glauber model. The full hadronic cross section is obtained by the integral of the Glauber fits and the centrality percentile of the event is the integral fraction of the measured V0 amplitude normalized to the total cross section. Alternatively, the multiplicity measurements from the TPC and the SPD could also be used to determinate the centrality, although the resolutions are slightly lower than using the V0 amplitudes (see Fig. 2.10 right.). More details can be found in [208].

In p–Pb collisions, the data sample is split in several multiplicity classes, defined by an analogous procedure to Pb–Pb collisions we discussed above. The measured multiplicity distribution is divided in percentiles of the hadronic cross-section. Fig. 3.3 shows the multiplicity distributions measured by V0-A, which is situated in the direction of the Pb beam, and is more sensitive to the fragmentation of the Pb nucleus. Following the similar procedure with centrality determination in Pb–Pb collisions, different multiplicity classes (0-20%, 20-40% *et. al.*) are obtained with a Glauber model fit. However, it is not clear how these multiplicity classes corresponds to the impact parameter in p–Pb collisions so far.

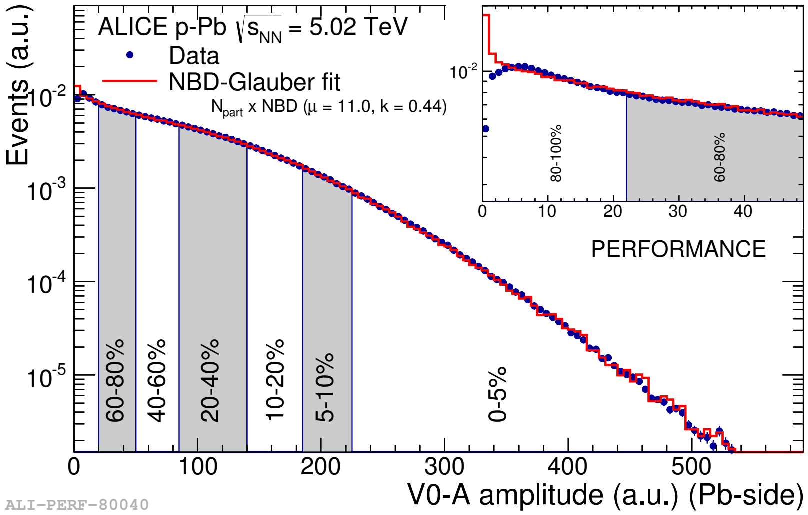

Figure 3.3: Distribution of the summed amplitudes in the V0A scintillator. The red curve shows the result of the Glauber model fit to the measurement.

3.2 Track Selection

3.2.1 Hybrid Tracks

In the 2010 data collection, some parts of the SPD were switched off, leading to inefficient regions for common track reconstruction. To ensure uniform distributions in the (η, φ) plane, a hybrid track approach of following types is used:

- global tracks with SPD hit(s) and an ITS refit
- global tracks w/o SPD hit and with an ITS refit, constrained to the primary vertex
- global tracks w/o ITS refit, constrained to the primary vertex.

The first type of tracks are used when available, and give the best transverse momentum resolution. When the first set of criteria are not fulfilled, then either of the two other sets are required. Since these tracks do not have an associated SPD hit, then the corresponding transverse momentum resolution is worse than the one obtained from the first type. In order to obtain better resolution in transverse momentum, the second and third type of tracks are constrained to the primary vertex of the event. Figure 3.5 shows the azimuthal angle distributions of these three types of tracks. The sum of these three types of tracks are shown in black markers, which clearly show a uniform acceptance in azimuthal angle.

In this analysis we select particles with transverse momentum $p_{\mathrm{T}} > 0.2$ GeV/c and pseudorapidity $|\eta| < 0.8$. The low p_{T} threshold is driven by the tracking capabilities of the ALICE detector, since the low p_{T} tracks do not reach the TPC. The selected pseudorapidity range is mainly due to the acceptance of the TPC in pseudorapidity, taking into account the requirement of a uniform acceptance.

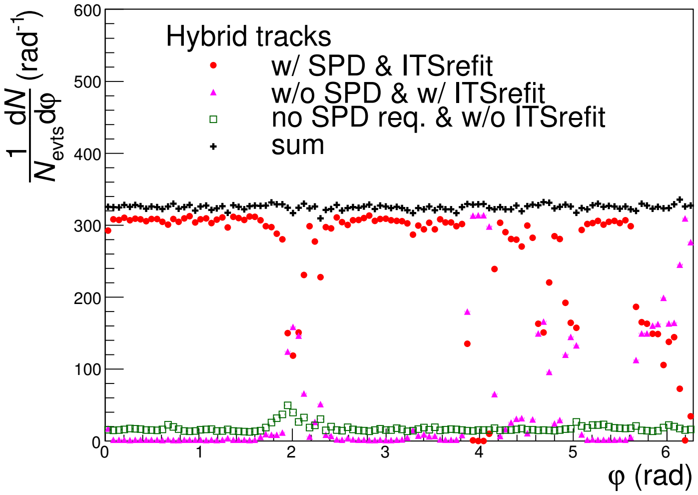

Figure 3.4: Azimuthal angle (φ) distribution of hybrid tracks in centrality 0-10 %.

When a charged track crosses the TPC, it will leave a signal in each pad row. The maximum number of clusters can be assigned to a track is 159 which is the total number of pad rows in the TPC. Those tracks with a large uncertainty of the estimated p_{T}, fake tracks and tracks not coming from the primary vertex generally have a low number of TPC clusters. Also the fake tracks typically have a large $\langle\chi^2\rangle$ per degree of freedom on the momentum fit. Therefore, the tracks used in this analysis are required to have a cut depends on its p_{T}: $N_{clusters,TPC} > 70 + 1.5p_{\mathrm{T}}$ together with $\langle\chi^2\rangle$ per TPC cluster ≤ 4 (with 2 degrees of freedom per cluster).

Tracks with a distance of closest approach (DCA) to the primary vertex within 2.4 cm in radial (xy) direction and 3.2 cm in the longitudinal (z) direction, are required for the hybrid tracks which are used in the analysis. This cut removes the contributions of secondary particles either from weak decay or from the interactions of particles with the material.

The track efficiency, defined as the ratio between the reconstructed and generated tracks:

$$\varepsilon(p_{\mathrm{T}}) = \frac{dN^{rec}/dp_{\mathrm{T,gen}}}{dN^{gen}/dp_{\mathrm{T,gen}}} \tag{3.3}$$

can be studied for Hybrid tracks via MC simulations. An example of such an efficiency curve as a function of the transverse momentum of the particle can be seen in Fig. 3.5. It is extracted by the analysis of simulated HIJING events, invoking also a realistic description of the ALICE detector setup using the GEANT3 transport code.

The tracking efficiency increases rapidly for low p_{T}, and is approximately constant (~0.8) at higher p_{T}. This is due to the loss of high p_{T} tracks that tend to be straight

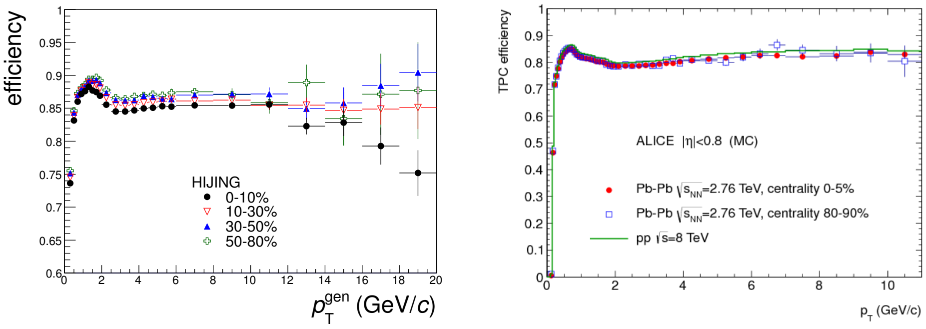

Figure 3.5: (Left) Track efficiency $\varepsilon(p_T)$ of hybrid tracks for various centrality classes using HIJING simulations; (Right) Track efficiency $\varepsilon(p_T)$ of TPConly tracks for Pb–Pb collisions in centrality classes 0-5%, 80-90% and pp collisions.

and can cross the dead zones of the TPC (i.e. regions that connect the 18 TPC sectors), the tracking efficiency is a few percent larger at $1 < p_T < 2$ GeV/c than at high p_T .

We use the hybrid tracks as a default option in the analysis discussed in this thesis, while tracks reconstructed only by the TPC (described below) are used for systematic studies.

Other Track Types

Standalone TPC constrained tracks use only TPC information from the first pass of tracking procedure constraint to the primary vertex from SPD. The kinematic cuts for standalone TPC tracks are $|\eta| < 0.8$ and $p_T > 0.2$. The tracks are required to have at least 70 reconstructed clusters and a $\langle\chi^2\rangle$ per TPC cluster ≤ 4. No kink daughter is accepted in standalone TPC tracks. In addition, the tracks with a DCA to the primary vertex larger than 2.4 cm in x-y direction and 3.2 cm in the z direction are rejected. With these cuts, we ensure a uniform distributions in φ, however due to this, the p_T resolution is slightly lower than for Hybrid tracks.

For the tracks reconstructed by both the TPC and the ITS detectors (know as global tracks) different quality cuts are applied. However, due to the non-uniform acceptance in φ distributions for these tracks, the correction will bring additional uncertainty. Therefore, these tracks are not ideal candidate for anisotropic flow analysis and willl not be used in this analysis.

Chapter 4

Flow Analysis Methodology

Relativistic heavy–ion collisions are an important tool to study the characteristics of the Quark–Gluon Plasma (QGP). The azimuthal anisotropy of the transverse momentum distribution in non–central heavy–ion collisions, suggested as a signature of collective flow by Ollitrault [170], is argued to be sensitive to the properties of the QGP.

A convenient way of characterizing the patterns of anisotropic flow is to use a Fourier expansion of the invariant triple differential distribution,

$$E\frac{d^3N}{d^3\mathbf{p}} = \frac{1}{2\pi}\frac{d^2N}{p_T dp_T dy}(1 + 2\sum_{n=1}^{\infty} v_n \cos[n(\varphi - \Psi_n)]), \tag{4.1}$$

where E is the energy, p is the momentum, p_T the transverse momentum, φ the azimuthal angle, y is the rapidity of the particle and the n^{th}-order symmetry plane (also called participant plane) is defined as Ψ_n. The different n^{th}-order flow coefficients [87] are represented with v_n and are given as follows:

$$v_n = \langle \cos[n(\varphi - \Psi_n)\rangle, \tag{4.2}$$

The second harmonic (v_2), the so-called elliptic flow, is the dominant coefficient reflecting mainly the elliptic shape of the overlap region. It has been the main focus of the experimental studies, at the CERN Super Proton Synchrotron (SPS) [105], the Brookhaven Relativistic Heavy Ion Collider (RHIC) [169], and the CERN Large Hadron Collider (LHC) [121]. For a recent summary see [127, 159]. More recently, it was realized that the higher harmonic anisotropic flow coefficients are also very important [161]. Hydrodynamic calculations predict that these higher harmonics, like triangular flow v_3, are more sensitive to the shear viscosity to entropy density ratio η/s of the QGP than v_2 [171].

In the following chapter, the most popular experimental flow analysis methods, Event Plane, Scalar Product and Q-Cumulant methods will be present.

4.1 Event Plane Method

4.1.1 Standard Event Plane Method

The standard Event Plane method [110] was, up to this moment, the most popular method in the anisotropic flow analysis [47]. In this method, the symmetry plane is reconstructed from the azimuthal distribution of particles in a detector. This estimate, called event plane, is given for each harmonic n by Eq. (4.3).

$$\mathrm{EP}_n = \frac{\arctan 2(Q_{n,y}, Q_{n,x})}{n} \tag{4.3}$$

where $Q_{n,x}$ and $Q_{n,y}$ are the x and y components of the Q-vector given by Eqs. (4.4) and (4.5), respectively:

$$Q_{n,x} = \sum_i w_i \cos(n\varphi_i) \tag{4.4}$$

$$Q_{n,y} = \sum_i w_i \sin(n\varphi_i) \tag{4.5}$$

where w_i is a weight which might depend on the centrality, transverse, pseudorapidity, particle species *et. al*.

The experimentally measured flow coefficient, v_n, is then given by Eq. 4.6:

$$v_n^{obs}(p_T, \eta) = \langle \cos[n(\varphi - \mathrm{EP}_n)] \rangle \ . \tag{4.6}$$

where the brackets denote an average over all particle with their azimuthal angle φ in a certain window (η and p_T) in all events at a fixed centrality. In order to eliminate the contribution from autocorrelations, we need to subtract the particles of interest from the calculation of the Q-vector. Considering the finite multiplicity of each event, the event plane and hence the v_n have to be corrected for the corresponding resolution for each harmonic:

$$\begin{aligned} \mathscr{R}_n &= \langle \cos[n(\mathrm{EP}_n - \Psi_n)] \rangle \\ &= \frac{\sqrt{\pi}}{2\sqrt{2}} \chi_n e^{-\chi_n^2/4} \times [I_{(k-1)/2}(\chi_n^2/4) + I_{(k+1)/2}(\chi_n^2/4)] \end{aligned} \tag{4.7}$$

where χ_n and I are modified Bessel function [110].

The final anisotropic flow coefficients are given by:

$$v_n\{\mathrm{EP}_n\} = \frac{v_n^{obs}}{\mathscr{R}_n} \tag{4.8}$$

Notice that the above equation can be used only in a narrow centrality bin [165]. For a wide centrality bin, one need to average the results from the narrow bins with weights (e.g. the multiplicity of the bin, or the reciprocal of the statistical uncertainty of v_n). More details about the resolution of the standard event plane method, one can found in [110].

However, there is a clear disadvantage of using the standard Event Plane method. The $v_n\{\mathrm{EP}_n\}$ measurement yields an ambiguous measure lying somewhere between the event-averaged mean value $\langle v_n \rangle$ and the root-mean-square value $\left\langle v_n^2 \right\rangle^{1/2}$ [154,155]. The exact value measured from the event plane method depends on the resolution $\mathscr{R}_n$, which strongly depends on the experimental setup. Therefore, there might be a systematically different value of v_n from different experiments [153]. On the other hand, the $v_n\{\mathrm{EP}\}$ measurement also suffers from non–flow effects. There are two simple approaches to solve these problems. One is to use the event plane method with three-subevents (which usually gives a lower resolution of the event plane in experiments, see section 4.1.2), the other is to use the Scalar Product or Q-Cumulant methods (see section 4.2, 4.3) with a pseudorapidity gap, because these three methods yield root-mean-square value $\left\langle v_n^2 \right\rangle^{1/2}$ and suppress the non–flow contributions.

4.1.2 Event plane using the three-subevents

As discussed above, in order to suppress the non–flow contribution which are additional correlations not associated with the symmetry plane Ψ_n, it is suggested to use a subevent method which includes a gap in pseudorapidity. If the subevents do not cover the same pseudo-rapidity range, one needs at least three windows to determine the event plane resolution in each of them [110]. Assuming we have three-subevents A, B and C, having a gap between each other, then the resolution in the subevent A is determined as:

$$\mathscr{R}_n^{\mathrm{A}} = \sqrt{\frac{\left\langle \cos[n({\mathrm{EP}_n}^{\mathrm{A}} - {\mathrm{EP}_n}^{\mathrm{B}})] \right\rangle \left\langle \cos[n({\mathrm{EP}_n}^{\mathrm{A}} - {\mathrm{EP}_n}^{\mathrm{C}})] \right\rangle}{\left\langle \cos[n({\mathrm{EP}_n}^{\mathrm{B}} - {\mathrm{EP}_n}^{\mathrm{C}})] \right\rangle}} \tag{4.9}$$

where ${\mathrm{EP}_n}^{\mathrm{A}}$ and ${\mathrm{EP}_n}^{\mathrm{B}}$ are the event planes reconstructed in subevent A and B, following Eqs. (4.3). The final flow measured from subevent A:

$$v_n\{\mathrm{EP}_n^{\mathrm{A}}\} = \frac{\left\langle \cos[n(\varphi_n - {\mathrm{EP}_n}^{\mathrm{A}})] \right\rangle}{\mathscr{R}_n^{\mathrm{A}}} = \frac{\left\langle \cos[n(\varphi_n - {\mathrm{EP}_n}^{\mathrm{A}})] \right\rangle}{\sqrt{\frac{\left\langle \cos[n({\mathrm{EP}_n}^{\mathrm{A}} - {\mathrm{EP}_n}^{\mathrm{B}})] \right\rangle \left\langle \cos[n({\mathrm{EP}_n}^{\mathrm{A}} - {\mathrm{EP}_n}^{\mathrm{C}})] \right\rangle}{\left\langle \cos[n({\mathrm{EP}_n}^{\mathrm{B}} - {\mathrm{EP}_n}^{\mathrm{C}})] \right\rangle}}} \tag{4.10}$$

We will only use the Event Plane method using three-subevents with the ALICE detector which has a low resolution of the reconstructed event plane in this thesis. This method gives a v_n value of the root-mean-square value $\left\langle v_n^2 \right\rangle^{1/2}$ which is closed to the results measured by two-particle correlations (cumulants) methods but is less influenced by non–flow effect.

4.2 Scalar Product Method

A more recent method of measuring two-particle correlations is the Scalar Product (SP) method, which correlates particles to the flow vector and uses its length as a weight in the average over events [156]. This method is based on the scalar product of a unit vector for particle i denoted as $u_{n,i}(p_T,\eta)$ with the complex conjugate of the flow vector Q^*. It follows that the differential flow of the particle of interest can be calculated by:

$$v_n\{\mathrm{SP}\} = \frac{\left\langle u^{\mathrm{A}}_{n,i}(p_T,\eta)\cdot\frac{Q^*_{n,B}}{M_B}\right\rangle}{\sqrt{\left\langle\frac{Q_{n,A}}{M_A}\cdot\frac{Q^*_{n,B}}{M_B}\right\rangle}}, \tag{4.11}$$

where $Q_{n,A}$ and $Q_{n,B}$ are the flow vectors from subevent A and B, while M_A and M_B are the multiplicities for the corresponding subevent [1].

In order to suppress non–flow effects (e.g. resonance decay effects), a pseudorapidity gap is applied between subevent A and B. In the case two subevent A and B cover an asymmetric psedurapidity range, we need to use the modified Scalar Product method developed by the ALICE Collaboration [172], which can be calculated via:

$$v_n\{\mathrm{SP}\} = \sqrt{v_n\{\mathrm{SP}\}^{\mathrm{A}}\cdot v_n\{\mathrm{SP}\}^{\mathrm{B}}} = \sqrt{\frac{\langle u_{n,i}(p_T,\eta)\cdot\frac{Q^*_{n,A}}{M_A}\rangle}{\sqrt{\langle\frac{Q_{n,A}}{M_A}\cdot\frac{Q^*_{n,B}}{M_B}\rangle}}\cdot\frac{\langle u_{n,i}(p_T,\eta)\cdot\frac{Q^*_{n,B}}{M_B}\rangle}{\sqrt{\langle\frac{Q_{n,A}}{M_A}\cdot\frac{Q^*_{n,B}}{M_B}\rangle}}} \tag{4.12}$$

where the unit vector $u_{n,i}(p_T,\eta)$ is calculated in a third subevent C.

The advantage of applying the Scalar Product method with pseudorapidity gap is that it gives v_n close to the root-mean-square value $\left\langle v_n^2\right\rangle^{1/2}$, and since the non–flow effect is mainly due to short range correlations. This contribution is removed by the large pseudorapidity gap. Also the results from the Scalar Product method do not depend on the detector. This gives the additional advantage of providing an easy, detector independent, method to compare results from different experiments.

Another version of the Scalar Product has been proposed recently by Ollitrault and his collaborates, to study the symmetry plane correlations [222]. We will discuss the method and the results in Section 6.3.

4.3 Q-Cumulant Method

Realizing the limitations of the previous methods, a new way of studying anisotropic flow effects was introduced in [111], based on the Q-cumulants. The advantage using the Q-Cumulant method is that it provides a fast (one loop over the data) and exact (no approximations and no interference between differential harmonics) estimations of the correlators.

4.3.1 Reference Flow

In the standard Q-Cumulant method, there are two steps, the first one being the calculation of the reference flow. The second step involves the correlation of the particle of interest with the reference flow established in the first step. For the reference flow

---

[1] In practice, one symmetrizes the $u_{n,i}(p_T,\eta)$ (and $Q_{n,B}$) from subevent A to subevent B (subevent B to subevent A) to decrease the statistical error

results, we obtain the single-event average two- and four-particle azimuthal correlations in the following way:

$$\langle 2\rangle = \frac{|Q_n|^2 - M}{M(M-1)} \tag{4.13}$$

$$\langle 4\rangle = \frac{|Q_n|^4 + |Q_{2n}|^2 - 2\cdot \mathrm{Re}[Q_{2n}Q_n^*Q_n^*]}{M(M-1)(M-2)(M-3)} - 2\frac{2(M-2)\cdot|Q_n|^2 - M(M-3)}{M(M-1)(M-2)(M-3)} \tag{4.14}$$

Here Q_n is the event-flow vector we discussed before, and M is the multiplicity per event.

The event average two- and four-particle azimuthal correlations can then be calculated from the single-event average two- and four-particle azimuthal correlations:

$$\langle\langle 2\rangle\rangle = \frac{\sum_{events}(W_{\langle 2\rangle})_i\langle 2\rangle_i}{\sum_{events}(W_{\langle 2\rangle})_i} \tag{4.15}$$

$$\langle\langle 4\rangle\rangle = \frac{\sum_{events}(W_{\langle 4\rangle})_i\langle 4\rangle_i}{\sum_{events}(W_{\langle 2\rangle})_i} \tag{4.16}$$

In order to minimize the effect of multiplicity variation in an event class, the optimal choice for the event weights is:

$$W_{\langle 2\rangle} \equiv M(M-1) \tag{4.17}$$

$$W_{\langle 4\rangle} \equiv M(M-1)(M-2)(M-3) \tag{4.18}$$

Following the general formalism of the cumulants introduced by Borghini *et. al.* [107, 108], the second-order cumulant, $c_n\{2\}$, is simply an average of two-particle correlations defined in Eqs. (4.13) with its weight defined in Eqs. (4.17):

$$c_n\{2\} = \langle\langle 2\rangle\rangle \tag{4.19}$$

The genuine four-particle correlations (i.e., four-particle cumulant) is given by:

$$c_n\{4\} = \langle\langle 4\rangle\rangle - 2\cdot\langle\langle 2\rangle\rangle^2 \tag{4.20}$$

Finally, the 2- and 4-particle reference flow can be obtained by:

$$v_n\{2\} = \sqrt{c_n\{2\}} \tag{4.21}$$

$$v_n\{4\} = \sqrt[4]{-c_n\{4\}} \tag{4.22}$$

4.3.2 Differential Flow

Once the reference flow has been estimated, we proceed to the calculation of the differential flow of the Particles Of Interests (POIs), where we need to use the p_n and q_n vectors. The former built out of all POIs, and the latter one only from POIs labeled also as Reference Flow Particles (RFPs). They can be calculated via:

$$p_n = \sum_{i=1}^{m_p} e^{in\phi_i} \tag{4.23}$$

$$q_n = \sum_{i=1}^{m_q} e^{in\phi_i} \tag{4.24}$$

where m_p is the total number of particles labeled as POIs, m_q is the total number of particles tagged both as RFP and POI.

Using the p_n and q_n vector, we obtained the following equations for the single-event average 2- and 4-particle correlations:

$$\langle 2^{'} \rangle = \frac{p_n Q_n^* - m_q}{m_p M - m_q} \tag{4.25}$$

$$\begin{aligned}\langle 4^{'} \rangle = & [p_n Q_n Q_n^* Q_n^* - q_{2n} Q_n^* Q_n^* - p_n Q_n Q_{2n}^* - 2 \cdot M p_n Q_n^* - 2 \cdot m_q |Q_n|^2 \\ & + 7 \cdot q_n Q_n^* - Q_n q_n^* + q_{2n} Q_{2n}^* + 2 \cdot p_n Q_n^* + 2 \cdot m_q M - 6 \cdot m_q] \\ & /[(m_p M - 3m_q)(M-1)(M-2)]\end{aligned} \tag{4.26}$$

The event average differential two- and four-particle azimuthal correlations then can be calculated from the single-event average differential two- and four-particle azimuthal correlations:

$$\langle\langle 2^{'} \rangle\rangle = \frac{\sum_{events} (W_{\langle 2' \rangle})_i \langle 2^{'} \rangle_i}{\sum_{events} (W_{\langle 2' \rangle})_i} \tag{4.27}$$

$$\langle\langle 4^{'} \rangle\rangle = \frac{\sum_{events} (W_{\langle 4' \rangle})_i \langle 4^{'} \rangle_i}{\sum_{events} (W_{\langle 2' \rangle})_i} \tag{4.28}$$

where in order to reduce the influence from multiplicity fluctuations, the weights now read:

$$W_{\langle 2' \rangle} \equiv m_p M - m_q \tag{4.29}$$

$$W_{\langle 4' \rangle} \equiv (m_p M - 3m_q)(M-1)(M-2) \tag{4.30}$$

For detectors with uniform azimuthal acceptance the differential 2- and 4-order cumulant are given by:

$$d_n\{2\} = \langle\langle 2^{'} \rangle\rangle \tag{4.31}$$

$$d_n\{4\} = \langle\langle 4^{'} \rangle\rangle - 2\langle\langle 2^{'} \rangle\rangle\langle\langle 2 \rangle\rangle \tag{4.32}$$

Finally the estimated differential flow $v_2(p_T, \eta)$ from two- and four-particle correlations are given by:

$$v_n\{2\}(p_T, \eta) = \frac{d_n\{2\}}{\sqrt{c_n\{2\}}} \tag{4.33}$$

$$v_n\{4\}(p_T, \eta) = -\frac{d_n\{4\}}{(-c_n\{4\})^{3/4}} \tag{4.34}$$

In the ideal case, taking two-particle correlations as an example, when only flow correlations are present, the numerator in the equations above give $v_n(p_T, \eta) \cdot v_n$, while the denominator gives $\sqrt{v_n \cdot v_n}$, so that overall the final differential flow $v_n(p_T, \eta)$ does not depend on the reference flow we select. More details can be found in [111].

4.3.3 Q-Cumulant Method with pseudorapidity gap

As discussed also in the other methods, in order to suppress the possible non–flow effects, an η gap is usually applied for two-particle correlations. In this thesis, we introduce an η gap of the 2-particle Q-Cumulant method, both for the calculations of the reference and differential flow [158]. For the reference flow, we select one particle from subevent A and the other from subevent B. This modifies Eqs. (4.13), that now reads:

$$\langle 2\rangle_{\Delta\eta} = \frac{Q_n^{\mathrm{A}} \cdot Q_n^{B*}}{M_A M_B}, \tag{4.35}$$

Here Q_n^{A} and Q_n^{B} are the same flow vectors used in Eqs. 4.11, the same for M_A and M_B which are the corresponding multiplicities. Inserting Eqs. (4.35) with its weight defined as:

$$W_{\langle 2\rangle_{\Delta\eta}} \equiv M_A M_B \tag{4.36}$$

into Eq. (4.15), we get the single-event average two-particle azimuthal correlations $\langle\langle 2\rangle\rangle_{\Delta\eta}$. The 2-particle reference flow can then be calculated via Eq. (4.22).

For the calculations of differential flow, there is no overlap of POIs and RPs if we select RPs from one subevent and POIs from the other. This modifies Eqs. (4.25) to:

$$\langle 2^{'}\rangle_{\Delta\eta} = \frac{p_{n,A} Q^*_{n,B}}{m_{p,A} M_B} \tag{4.37}$$

using Eqs. (4.32) with the weights calculated as:

$$W_{\langle 2'\rangle_{\Delta\eta}} \equiv m_{p,A} M_B \tag{4.38}$$

we get the differential 2-particle cumulant. Finally the differential flow from two-particle cumulant can be obtain by inserting the two-particle reference flow (with η gap) and the differential two-particle cumulant.

4.4 Non–flow

Because the symmetry planes are not observed experimentally, the anisotropic flow can't be measured directly. Therefore, it is usually estimated using azimuthal correlations between the observed particles, like the Scalar Product and Q-Cumulant method. Both Scalar Product and two-particle cumulant methods can be affected by non–flow contributions, which are the azimuthal correlations not due to corrections with the symmetry plane.

We demonstrate the two-particle non–flow contribution in figure 4.1. In Fig. 4.1(a) we see an anisotropic distribution which leads to positive value of both v_2 and $v_2\{2\}$; Fig. 4.1(b) shows a symmetric distribution and therefore $v_2 = 0$ and $v_2\{2\} = 0$; Fig. 4.1(c) shows the additive of two symmetric distribution, which gives $v_2 = 0$ but $v_2\{2\} > 0$. The figure explains how non–flow (like from resonance decays or jets) influence v_2 measured from two-particle correlations.

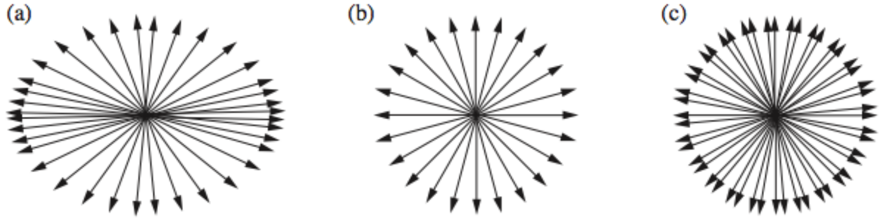

Figure 4.1: Examples of particle azimuthal distributions in the transverse plane where (a) $v_2 > 0$, $v_2\{2\} > 0$; (b) $v_2 = 0$, $v_2\{2\} = 0$; (c) $v_2 = 0$, $v_2\{2\} > 0$

Now we know the two-particle azimuthal correlations can be written as:

$$\begin{aligned}\langle\langle e^{in(\varphi_1-\varphi_2)}\rangle\rangle &= \langle\langle e^{in[(\varphi_1-\Psi_n-(\varphi_2-\Psi_n)]}\rangle\rangle \\ &= \langle\langle e^{in(\varphi_1-\Psi_n}\rangle\langle e^{in(\varphi_1-\Psi_n}\rangle + \delta_n^2\rangle \\ &= \langle v_n^2 + \delta_n^2\rangle\end{aligned} \tag{4.39}$$

From Eqs. (4.39), we can factorize the two-particle azimuthal correlations into the part related to the correlations with respect to the common symmetry plane (the *anisotropic flow*) and the one independent of the symmetry plane, the latter part that corresponds to non–flow is denoted by the term δ_n [159].

Several different methods have been presented so far, each one having different sensitivities to non–flow. A common way to suppress non–flow effects experimentally is by using an η gap, which we mentioned few times above. This gap suppresses the contributions of short-range correlations. However, for the other effects, like the aways side jet contributions, there is no good way to completely remove the contributions.

4.5 Flow fluctuations

In addition to non–flow, flow fluctuations also influence the v_2 measurements in experiments. When the heavy-ion collision starts, the nucleon distributions inside the overlap area fluctuate event-by-event, as already illustrated in figure 1.7. These initial geometry fluctuations will lead to flow fluctuations in the final state. It has been shown in [89] that in the limit of small fluctuations ($\sigma_v < \bar{v}$), for two- and mutli-particle correlations:

$$v_n\{2\}^2 = v_n^2 + \sigma_v^2 + \delta_n^2 \tag{4.40}$$

$$v_n\{4\}^2 = v_n^2 - \sigma_v^2 \tag{4.41}$$

$$v_n\{6\}^2 = v_n^2 - \sigma_v^2 \tag{4.42}$$

where v_n is the 'true' flow developed with respect to the symmetry plane, σ_v is the measure of flow fluctuations and δ_v is the non–flow contribution. Flow fluctuations have become an important part of the anisotropic flow studies, especially after the observation of the triangular flow v_3 [122, 161], which is mostly coming from initial geometry fluctuations. The connection of the anisotropy fluctuation in the initial state to the flow fluctuations in the final state provides important information which helps us to better understand and constrain the initial state.

Chapter 5

Anisotropic flow measurements

One of the fundamental questions in the phenomenology of Quantum Chromo Dynamics (QCD) is what the properties of matter are at the extreme densities and temperatures where quarks and gluons are in a deconfined state, the so-called Quark Gluon Plasma (QGP). Collisions of high-energy heavy-ions, at the Brookhaven Relativistic Heavy Ion Collider (RHIC) and the CERN Large Hadron Collider (LHC), allow us to create and study the properties of such a system in the laboratory. The azimuthal anisotropy in particle production is, at these energies, an observable which provides experimental information on the Equation of State and the transport properties of the QGP. This anisotropy is usually characterized by the Fourier coefficients [87],

$$\begin{aligned} v_n &= \langle \cos\left[n(\varphi - \Psi_n)\right] \rangle, \text{or equivalently} \\ v_n &= \langle e^{in\varphi} e^{-in\Psi_n} \rangle \end{aligned} \tag{5.1}$$

where φ is the azimuthal angle of the particles, Ψ_n is the n^{th}-order flow-plane angle and $\langle\,\rangle$ an average over the selected particles and events. In the last decade, the elliptic flow v_2 [105, 121, 169] which is considered to correspond to the elliptic shape of the spatial overlap region in the system created in the collisions [170] has received a lot of experimental and theoretical attention. For a recent summary see [127, 159]. More recently it was realized that higher odd and even anisotropic flow coefficients are also very important [161]. Hydrodynamic calculations predict that these higher harmonics, such as the triangular flow v_3, are more sensitive to the shear viscosity to entropy density ratio η/s of the QGP than v_2 [171].

In this chapter, we will discuss not only elliptic flow, but also higher harmonic flow for both charged particles and identified particles measured in ALICE.

5.1 Elliptic Flow

The centrality dependence of elliptic flow v_2, measured by 2- and 4-particle cumulant method, fitting q-distributions (FQD) method and Lee-Yang Zeroes (LYZ) method are shown in Figure 5.1 (Left). The clear difference between $v_2\{2\}$ and $v_2\{4\}$ was observed

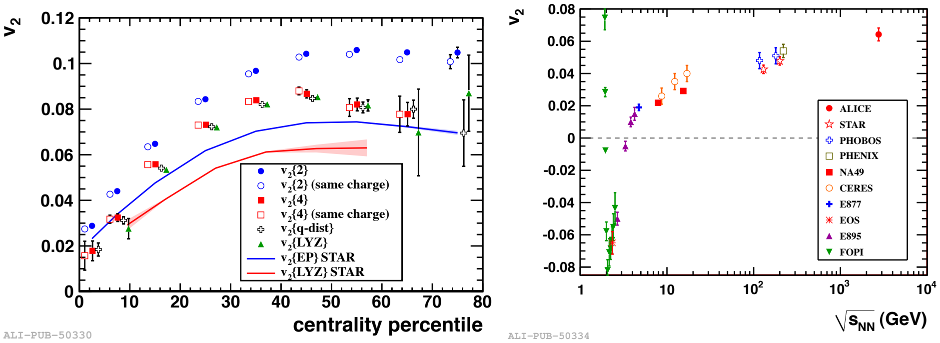

Figure 5.1: (Left) Centrality dependence of v_2 measured by various method. (Right) Energy dependence of v_2 in 20-30% centrality class.

for all centrality classes, which could be understood as due to non-flow effects as well as due to flow fluctuations. Generally speaking, the non-flow effects is negligible for $v_2\{4\}$ because its magnitude $\propto \frac{1}{(M-1)(M-2)(M-3)}$ while it is still visible for $v_2\{2\}$ as its magnitude $\propto \frac{1}{M-1}$ [1]. The contributions of flow fluctuations is positive for $v_2\{2\}$ and negative for $v_2\{4\}$. The measurements with same charge have been tested for $v_2\{2\}$ and $v_2\{4\}$. Considering that most of resonances will decay into particles with different charge, the measurements of 2- and 4-particle cumulants with same charge will be less influenced by non-flow effects (resonance decay). In Fig. 5.1 (Left) the difference between measurements of all charged and same charge suggest that non-flow effects are included in $v_2\{2\}$ and are increasing from central to peripheral collisions as expected due to the decrease in multiplicity M, while the non-flow effects are invisible in $v_2\{4\}$ measurements. Nice agreements between $v_2\{4\}$, $v_2\{\mathrm{q-dis}\}$ and $v_2\{\mathrm{LYZ}\}$ is also observed for the presented centrality classes, implying similar sensitivity to non-flow and flow fluctuations of multi-particle correlations. In addition, the v_2 measurements with the Event Plane method and LYZ method at STAR are smaller than those at ALICE, at the level of 30-50%. Considering the different p_{T} cuts used in different experiments, the correction of the integrated v_2 for the p_{T} cutoff of 0.2 GeV/c was applied using the Monte Carlo model Therminator. The comparison of the corrected v_2 measured in the 20-30% centrality class at LHC and at lower energies is presented in Fig. 5.1 (Right). It shows a continuous increase in the magnitude of v_2 from SPS to LHC, especially a 30% increase from top RHIC to LHC energy is observed. Such a 30% increase is bigger than the ideal hydrodynamic predictions [146] but agrees with viscous hydrodynamics calculations [147, 220].

In order to understand the 30% increasing of integrated v_2, we study the v_2 in more details with the p_{T}-differential flow measurements. Figure 5.2 (a) shows the differential flow $v_2(p_{\mathrm{T}})$ for the centrality class 40-50% using 2- and 4-particle cumulant methods, denoted as $v_2\{2\}$ and $v_2\{4\}$, respectively. The $v_2\{2\}$ and $v_2\{4\}$ measurements differ from

---

[1] M is usually not a small number in heavy ion collisions and therefore the non-flow effects is very small in multi-particle cumulant measurements

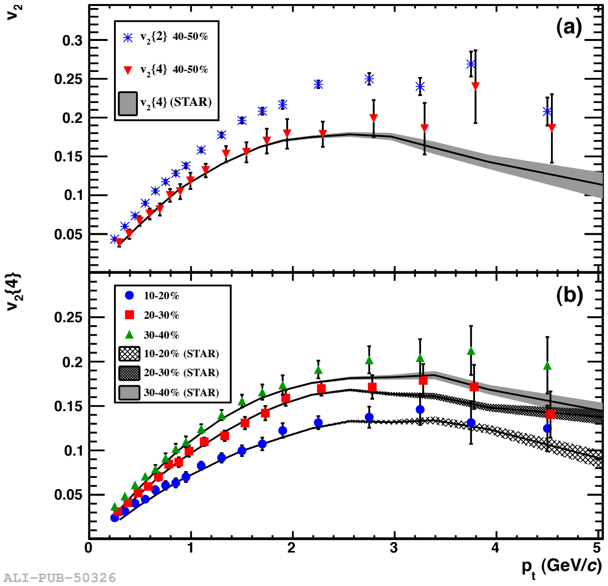

Figure 5.2: (Left) (a) The differential $v_2(p_\mathrm{T})$ for centrality class 40-50% from the 2- and 4-particle cumulant methods, shown by star and triangular; (b) The 4-particle cumulant measurements from ALICE and STAR in three centrality classes. (Right) Integrated v_2 in 20-30% Pb–Pb collisions at $\sqrt{s_\mathrm{NN}} = 2.76$ TeV, compared with results from lower energies at same centrality class.

each other, in agreement with the measurements show in Fig. 5.1, due to different sensitivities to non-flow and flow fluctuations. The comparison for the same measurements in STAR are also presented in the same centrality class. It is found that the differential flow $v_2\{4\}$ does not change within uncertainties from top RHIC to LHC energy (which is more than one order of magnitude higher). Such agreement of $v_2\{4\}$ measured at top RHIC and LHC energies is observed in 40-50% but also for other centrality classes, shown in Fig. 5.2 (b). To better understand this agreement, the identified particle $v_2(p_\mathrm{T})$ at both top RHIC and LHC energy are discussed. It shows that π $v_2(p_\mathrm{T})$ is higher while $\bar{p}$ $v_2(p_\mathrm{T})$ is lower at LHC than at RHIC, due to the stronger radial flow produced at the LHC. Therefore, the quantitatively very similar results for charged particle $v_2\{4\}$ at LHC and RHIC might be just an accident due to the interplay of the increasing eccentricity and radial flow [189].

To better understand the non-flow effects in the 2-particle cumulant, in Fig. 5.3 the $v_2\{2\}$ with various pseudorapidity gaps are presented. Because not only the daughter particles decayed from the same resonance but also the particles within the same jet usually enter similar pseudorapidity region, applying a pseudo rapidity gap between two correlated particles will suppress the non-flow effects in the 2-particle cumulant. It shows that the magnitudes of all v_2 measurements increase from 0-5% most central collisions to 40-50%, then decrease from 50-60%. The difference of v_2 without eta gap

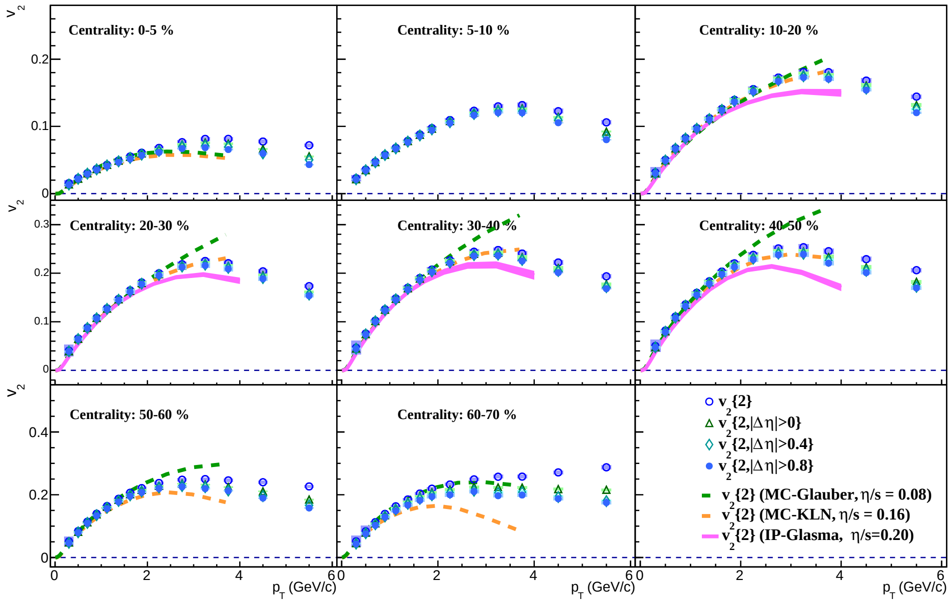

Figure 5.3: The $v_2\{2\}$ with no $|\Delta\eta|$ gap (open circle), $|\Delta\eta| > 0$ (open triangle), $|\Delta\eta| > 0.4$ (open diamond) and $|\Delta\eta| > 0.8$ (solid circle) for various centrality classes in Pb–Pb collisions at $\sqrt{s_{NN}} = 2.76$ TeV. Hydrodynamic calculations with MC-Glauber initial condition and $\eta/s = 0.08$, with MC-KLN initial condition and $\eta/s = 0.16$ and with IP-Glasma initial condition and $\eta/s = 0.20$ [21] are shown in green, orange and magenta curves, respectively.

and $v_2\{2, |\Delta\eta| > 0.8\}$ increases from central to peripheral collisions, which suggest that the contributions of non-flow effects (mainly short range correlations) increase towards peripheral collisions. The comparison to several hydrodynamic calculations shows that all calculations quantitively agree with non-flow suppressed 2-particle cumulant measurement, $v_2\{2, |\Delta\eta| > 0.8\}$, at least for $p_{\mathrm{T}} < 2$ GeV/c. Therefore, due to the lack of knowledge about initial conditions, there is a large uncertainty in the extracted η/s (ranges from 0.08 to 0.20) from v_2 measurements.

Better constrains the initial state condition and the extracted η/s are are obtained measuring the higher harmonic anisotropic flow and/or v_2 of identified particles, which are discussed in Chapter 5.2 and 5.3, respectively.

5.2 Higher Harmonic Flow

Due to the fluctuations in the initial matter distribution, including contributions from fluctuations in the positions of the participating nucleons in the nuclei, the participant plane, determined by the participating nucleons, fluctuates event by event. Such event-by-event fluctuations of the spatial asymmetry generate additional odd harmonic symmetry planes, which are predicted to give rise to the odd harmonics like v_3 and v_5. It is suggested that higher harmonic anisotropic flow coefficients are more sensitive to η/s, because the effect of shear viscosity reduces all anisotropic flow coefficients, with a larger decrease for higher order coefficients. Systematic studies of higher harmonic anisotropic flow of charged particles, will not only help us to understand the initial geometry and its event-by-event fluctuations, but also the η/s of the produced QGP.

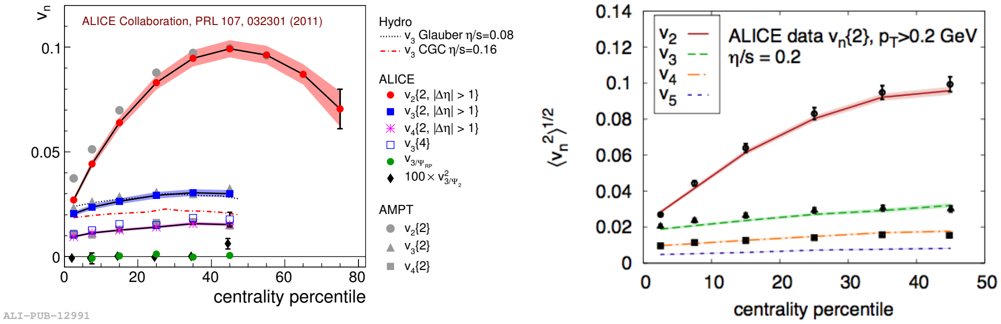

Figure 5.4: The centrality dependence of $v_n\{2\}$ in Pb–Pb collisions at $\sqrt{s_{\rm NN}} = 2.76$ TeV measured by ALICE. The hydrodynamic calculations based on IP-Glasma initial conditions and $\eta/s = 0.20$ are also shown here.

Figure 5.4 (Left) shows v_2, v_3, and v_4 integrated for $0.2 < p_{\rm T} < 5.0$ GeV/c as a function of centrality. The v_2, v_3, and v_4 are measured with a pseudorapidity gap $|\Delta\eta| > 1$ to suppress the non-flow effects. The estimated remaining non-flow contributions are corrected based on the correlation measured in HIJING, which does not include flow but only non-flow effects like jets and resonance decays. It shows that the anisotropic flow v_n follows $v_2 > v_3 > v_4$, this decrease in magnitude with increasing n might be due to the presence of viscous effects. The v_2 increases from central to mid-peripheral collisions and then decreases in most peripheral collisions. In addition, the higher harmonic anisotropic flow show a weak centrality dependence. This might be explained as v_2 mainly reflects the geometry of the initial overlap area, while the higher harmonics seem to mainly reflect the fluctuations of the initial geometry. Besides, $v_3\{4\}$ is finite and found to be 50% smaller than $v_3\{2, |\Delta\eta| > 1\}$, which agrees with the predictions from hydrodynamic calculations in [142]. In order to understand the contributions to v_3, not only the correlations of azimuthal angle φ *w.r.t.* third order symmetry plane Ψ_3 but also the one *w.r.t.* the other planes e.g. second order symmetry plane Ψ_2 and reaction plane $\Psi_{\rm RP}$ are measured. It is found that the v^2_{3/Ψ_2} and $v_{3/\Psi_{\rm RP}}$ are consistent with 0, suggesting that v_3 develops from its own participant plane Ψ_3, there is no contributions received from neither Ψ_2 nor $\Psi_{\rm RP}$. Various hydrodynamic calculations have been compared to the measured centrality dependence of v_n. It is found that only the one with IP-Glasma initial condition and $\eta/s = 0.20$ describes $v_2\{2\}$, $v_3\{2\}$ and $v_4\{2\}$ simultaneously. Clearly the anisotropic flow, especially the higher harmonic flow, put strong constrains on the initial state model and η/s, as we discussed before.

Generally speaking, both initial anisotropy and shear viscosity influence the mag-

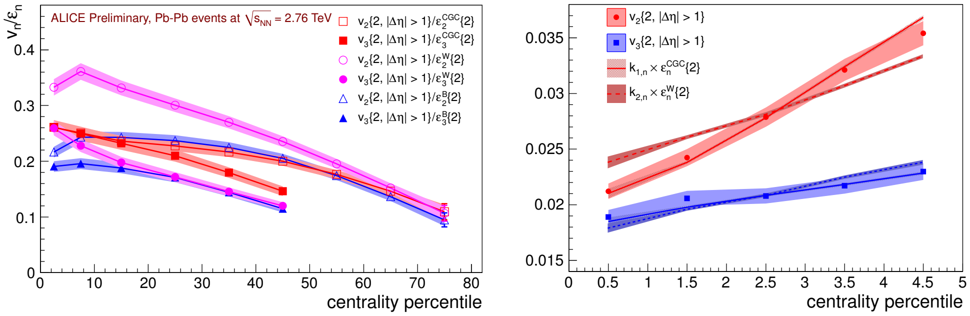

Figure 5.5: The centrality dependence of $v_n\{2, |\Delta\eta| > 1\}$ divided by the corresponding anisotropy ε_n from MC-Glauber with wounded nucleon weight, binary collisions weight and MC-KLN (CGC) in Pb–Pb collisions at $\sqrt{s_{\rm NN}} = 2.76$ TeV measured by ALICE.

nitude of anisotropic flow v_n. To investigate the role of viscosity further, we calculate the ratios v_n/ε_n, to avoid the influence from initial anisotropy as much as possible. Note that the ε_2 and ε_3 are the eccentricity and triangularity of the initial spatial geometry obtained from different initial state models. Considering the final state anisotropic flow is a response to initial geometry anisotropy, it is natural (and also born out by hydrodynamical model calculations) to assume that $v_n \propto \varepsilon_n$, and furthermore we have $v_n\{2\} \propto \varepsilon_n\{2\}$ [96] (for n =2, 3). Figure 5.5 shows the centrality dependence of $v_n\{2, |\Delta\eta| > 1\}$ divided by the corresponding anisotropy ε_n from MC-Glauber with wounded nucleon weighting, binary collisions weighting and MC-KLN (CGC) (different initial state models which gives you different calculations of ε_n). It is shown that for MC-Glauber model the magnitude of $v_3\{2, |\Delta\eta| > 1\}/\varepsilon_3\{2\}$ is smaller than $v_2\{2, |\Delta\eta| > 1\}/\varepsilon_2\{2\}$, interdependent of the weights used in the calculations of ε_n, which would indicate significant viscous corrections for v_3. For the MC-KLN (CGC) calculations, $v_2\{2, |\Delta\eta| > 1\}/\varepsilon_2\{2\}$ and $v_3\{2, |\Delta\eta| > 1\}/\varepsilon_3\{2\}$ are almost identical in most central collisions, as expected for an almost ideal fluid [171]. In addition, $v_3\{2, |\Delta\eta| > 1\}/\varepsilon_3\{2\}$ decreases faster than $v_2\{2, |\Delta\eta| > 1\}/\varepsilon_2\{2\}$ toward more peripheral collisions, due to possible bigger viscous corrections to v_3.

Because the viscous effects are not expected to change too much in a narrow centrality interval, we study the correlations of $v_n\{2\}$ and $\varepsilon_n\{2\}$ in 0-5%. We find that $v_3\{2, |\Delta\eta| > 1\}$ shows a very weak centrality dependence, this can be describe by the scaled $\varepsilon_3\{2\}$ from both the MC-Glauber and the MC-KLN (CGC) initial state model. At the same time, $v_2\{2, |\Delta\eta| > 1\}$ increases by almost 60% in the 0-5% centrality interval, this centrality dependence can be described only by the $\varepsilon_2\{2\}$ from MC-KLN (CGC) initial condition.

To further constrain the initial condition and η/s, we present the v_3 and v_4 measurements with various pseudorapidity gaps, as well as the comparisons to three different hydrodynamic calculations in Fig. 5.6 and 5.7. Both the differential v_3 and v_4 show a weak centrality dependence, and they are decreasing as the pseudorapidity gap increases, which might suggest that non-flow effects in v_3 and v_4 are suppressed by using a

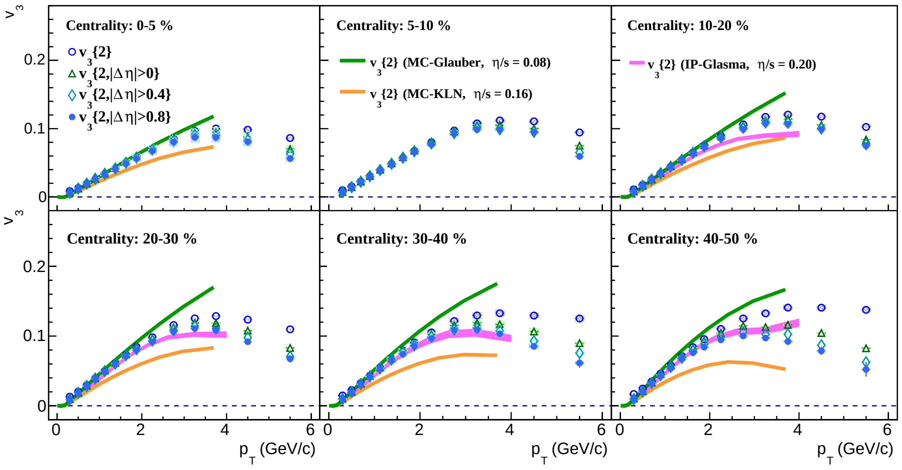

Figure 5.6: The $v_3\{2\}$ with different $|\Delta\eta|$ gap are presented for various centrality classes in Pb–Pb collisions at $\sqrt{s_{NN}} = 2.76$ TeV. The $v_3\{2\}$, $v_3\{2, |\Delta\eta| > 0\}$, $v_3\{2, |\Delta\eta| > 0.4\}$ and $v_3\{2, |\Delta\eta| > 0.8\}$ are represented by open circle, open triangle, open diamond and solid circle, respectively. Hydrodynamic calculations with MC-Glauber initial condition and $\eta/s = 0.08$, with MC-KLN initial condition and $\eta/s = 0.16$ and with IP-Glasma initial condition and $\eta/s = 0.20$ are shown in green, orange and magenta curves, respectively.

large pseudorapidity gap in 2-particle correlations. Although nice agreement is observed between data and three different hydrodynamic calculations for v_2, it seems that only the hydrodynamic calculation with IP-Glasma initial state and $\eta/s = 0.20$ describes $v_3\{2, |\Delta\eta| > 0.8\}$ and $v_4\{2, |\Delta\eta| > 0.8\}$ fairly well, calculations with a MC-Glauber initial state and $\eta/s = 0.08$, or with MC-KLN initial state and $\eta/s = 0.20$ can't quantitatively describe the data.

The measured centrality and p_{T} dependence of v_2, v_3 and v_4 compared to hydrodynamic calculations are best described by the initial condition used in the IP-Glasma model. These results seems lead the conclusion that a new state of strongly interacting matter with shear viscosity to entropy density $\eta/s = 0.20$ has been created in $\sqrt{s_{\mathrm{NN}}} = 2.76$ TeV Pb–Pb collisions at LHC.

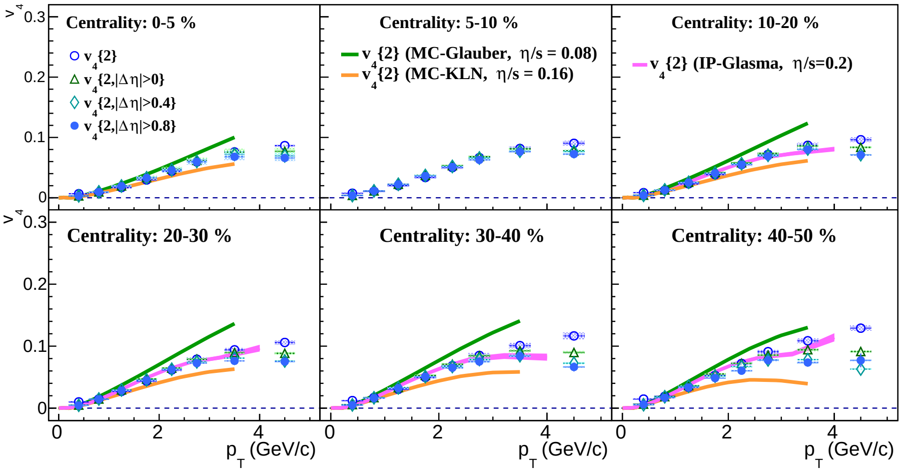

Figure 5.7: The $v_4\{2\}$ with different $|\Delta\eta|$ gap are presented for various centrality classes in Pb–Pb collisions at $\sqrt{s_{NN}} = 2.76$ TeV. The $v_4\{2\}$, $v_4\{2, |\Delta\eta| > 0\}$, $v_4\{2, |\Delta\eta| > 0.4\}$ and $v_4\{2, |\Delta\eta| > 0.8\}$ are represented by the open circles, open triangles, open diamonds and solid circle, respectively. Hydrodynamic calculations with MC-Glauber initial condition and $\eta/s = 0.08$, with MC-KLN initial condition and $\eta/s = 0.16$ and with IP-Glasma initial condition and $\eta/s = 0.20$ are shown in green, orange and magenta curves, respectively.

5.3 Identified Particle Flow

The study of anisotropic flow in relativistic heavy collisions at RHIC suggested that the produced system is described as a strongly coupled quark-gluon plasma (sQGP) [174–176]. Theoretical arguments, based on the AdS/CFT conjecture, suggest a lower bound of $1/4\pi$ (in natural units) for the ratio of shear viscosity to entropy density η/s [186]. Recent measurements at the LHC indicate that the system created in Pb–Pb collisions at $\sqrt{s_{\rm NN}} = 2.76$ TeV also behaves as a strongly interacting liquid [121, 122]. Additional constraint on the value of η/s can be obtained by studying the anisotropic flow of identified particles [174–176]. In this chapter, we will discuss the anisotropic flow of identified particles measured in ALICE, focusing on the v_2 of ϕ meson, which is one of the main topic of this thesis.

5.3.1 ϕ meson v_2

The ϕ meson consists of a strange (s) and an anti-strange ($\bar{s}$) quark, and its interaction with hadrons is suppressed due to the Okubo-Zweig-Izuka (OZI) rules [178]. One consequence is that the ϕ meson is expected to have a rather small hadronic cross section *w.r.t.* other hadrons, as suggested from a phenomenological analysis [177] (although the ϕ meson cross section are still not well known). Therefore, the ϕ meson produced in relativistic heavy ion collisions is expected to provide information about the early partonic stages of the system's evolution and will not be affected by later hadronic interactions.

In a (locally) thermalized system, for instance in hydrodynamics, the interplay of radial expansion and anisotropic flow leads to a specific dependence of the differential flow $v_n(p_\mathrm{T})$ on the mass of the particles [188, 189]. Indeed systematic studies of elliptic flow for heavy, strange and multi-strange hadrons measured at RHIC confirm the mass ordering picture for the low p_T region ($p_\mathrm{T} \leq 2$ GeV/c) [174–176]. In addition, when v_2 is scaled by the number of constituent quarks (n_q) and is plotted as function of transverse momentum or transverse kinetic energy (KE_T), v_2/n_q shows universal scaling for a broad range of particle species at intermediate p_T ($2 < p_\mathrm{T} < 5$ GeV/c). This so-called number of constituent quark scaling has been interpreted as evidence of partonic collectivity, one of the conditions for QGP formation.

Considering that the mass of the ϕ meson is close to that of a proton and Λ, but its number of constituent quark (n_q) is 2, while 3 for a proton and Λ, the ϕ meson v_2 measurement is an important check of the mass ordering scenario predicted by hydrodynamical models. In addition, it will also provide an important benchmark test for the universal scaling, strengthening the evidence for partonic collectivity.

v_n versus m_{inv} method

The anisotropic flow of resonances can not be directly measured in experiments, but could be studied via either the $\varphi - \Psi_n$ method [191] or with the v_n versus m_{inv} method [166] according to:

$$v_n^{Tot}(m_{inv}) = v_n^{Sig}\frac{N^{Sig}}{N^{Tot}}(m_{inv}) + v_n^{Bg}(m_{inv})\frac{N^{Bg}}{N^{Tot}}(m_{inv}). \tag{5.2}$$

Here $v_n^{Tot}(m_{inv})$ and $v_n^{Bg}(m_{inv})$ are the v_n of all the pairs and background, respectively; $\frac{N^{Sig}}{N^{Tot}}(m_{inv})$ and $\frac{N^{Bg}}{N^{Tot}}(m_{inv})$ are the relative yields of signal and background w.r.t the total number of particle pairs. The first step is to reconstruct the invariant mass distributions of kaon pairs and calculate $\frac{N^{Sig}}{N^{Tot}}(m_{inv})$ and $\frac{N^{Bg}}{N^{Tot}}(m_{inv})$.

ϕ meson invariant mass spectra

The ϕ meson was reconstructed via its hadronic decay channel: $\phi \rightarrow \mathrm{K}^+ + \mathrm{K}^-$ with a branching ratio of 48.9%. For the identification of charged kaons over a wide p_T range, the combined information from the TPC and the TOF detectors was used. Specifically, the identification was based on a two dimensional correlation between the response of the TPC and TOF and defining n standard deviations ($n\sigma^K_{detector}$) contour lines (i.e. related to the dE/dx and the TOF resolution) in this plane in various momentum intervals. Fig. 5.8 (middle) shows an example of the correlation plot between the number of standard deviation from the expected signal of the TPC and the TOF detectors. The default setting is '$3\sigma^K$' for kaon selections for the presented p_T range while different '$n\sigma^K_{detector}$' kaon selections have been used for the systematic study which will be discussed later.

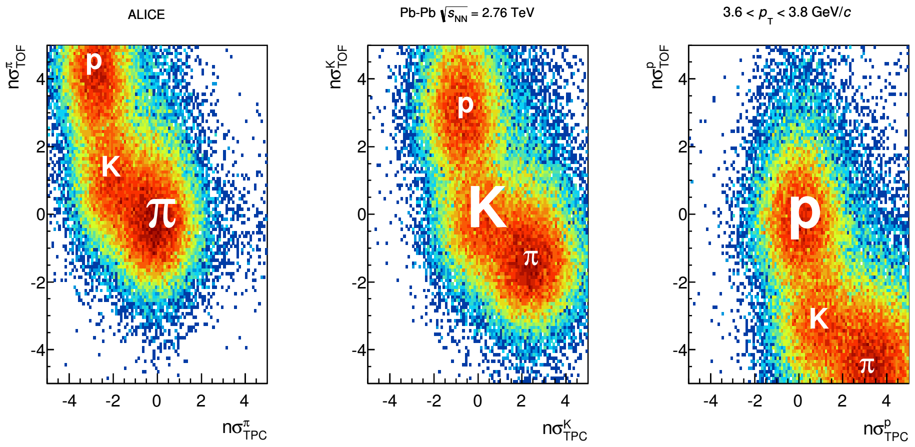

Figure 5.8: The correlation between the number of standard deviations from the expected signal of the TPC and the TOF detectors using the three different mass hypotheses for $3.6 < p_T < 3.8$ GeV/c in 0–5% most central Pb–Pb collisions.

ϕ meson reconstruction

The selected kaons are combined to form unlike-sign kaon pairs which are used to build up the invariant mass spectrum of the ϕ meson (see Fig. 5.9a). Background removal from this spectrum is performed in two steps: combinatorial background removal by subtraction, and residual background removal by fitting.

The combinatorial background can be removed by subtracting the like–sign pair spectrum from the unlike-sign pair spectrum (see Fig. 5.9b). In case the number of like-sign kaon pairs is not equal to the number of unlike-sign kaon pairs, the combinatorial background is normalized to an invariant mass region outside of the expected ϕ peak.

After the combinatorial background subtraction there is still some residual background. Assuming the invariant mass distribution of the background can be approximated by 2^{nd} polynomial function, one can subtract the residual background by using a polynomial fit. This fitting process is performed in two steps: first of all, the residual background in the invariant mass spectrum is approximated by a 2^{nd} order polynomial functions (see long-red-dash line in Fig. 5.9b). Then using the estimated background obtained in the first step, the invariant mass spectrum (green circles in Fig. 5.9b) is fitted again with a sum of a Breit-Wigner distribution and a 2^{nd} order polynomial function (blue line in Fig. 5.9b). (Different fitting functions are tested, the yielded differences compared to the default setting have been included in the final systematic uncertainty.)

After subtracting the combinatorial and residual background, we obtain the invariant mass spectrum of ϕ meson (see blue circles in Fig. 5.9c). By dividing the raw invariant mass distributions (see Fig. 5.9a) from the ϕ meson invariant distributions (Fig. 5.9c), the $\frac{N^{Sig}}{N^{Tot}}(m_{inv})$ and $\frac{N^{Bg}}{N^{Tot}}(m_{inv})$ could easily be obtained. The results is presented by green and azure circles and fitted with a Breit-Wigner function, shown in red dashed and

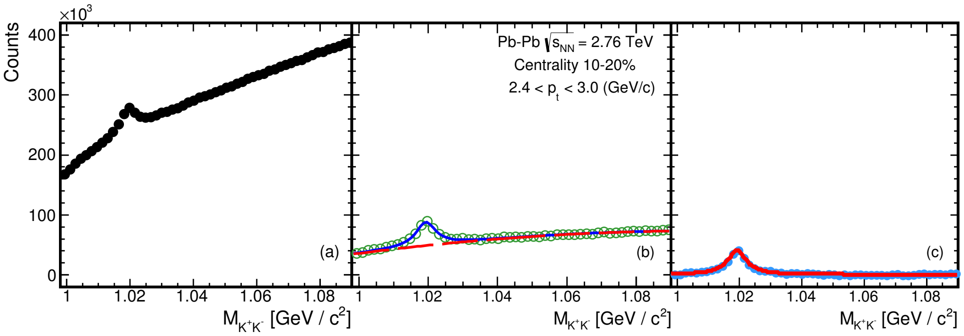

Figure 5.9: Invariant mass distributions (a) built by unlike-sign kaon pairs (black solid circles); (b) after the combinatorial background subtraction (green open circles); (c) after residual background subtraction (blue solid circles), at $2.4 < p_{\mathrm{T}} < 3.0$ GeV/c in 10–20 % centrality.

solid lines in Fig. 5.10. It is found that the extracted mass and width of ϕ meson peak are in agreement with PDG value, when taking the detector resolution into account.

ϕ meson v_2 extraction

The $v_2^{Tot}(m_{inv})$ could be measured directly via the Q-Cumulant, Scalar Product and Event Plane methods, as a function of invariant mass in different p_{T} bins. An example can be found in Fig. 5.10 (bottom) where the blue markers stand for the $v_2^{Tot}(m_{inv})$ measurements based on the SP method with $|\Delta\eta|$ >0.9, taking kaon pairs from the TPC acceptance correlated with the reference particles in the VZERO. The possible non-flow effects will be suppressed because of the large pseudo rapidity gap between TPC and VZERO. The red lines are the fit to v_2^{Tot}, which is the sum of a Breit-Wigner function plus a 2^{nd} order polynomial function. The $v_2^{Bg}(m_{inv})$ is parameterized as a 2^{nd} order polynomial function to take care of the non-constant v_2^{Bg} value as a function of invariant mas.

All variables in Eq. (5.2) are available and the ϕ meson v_2 can not be extracted by fitting the $v_2^{Tot}(m_{inv})$ distributions with Eq. (5.2) [2]. The fitting procedure is shown in red solid line and the extracted fitting parameters v_2^{Sig} is the ϕ meson v_2 measured by V0-SP method at $2.4 < p_{\mathrm{T}} < 3.0$ GeV/c in 10-20 % centrality class shown in Fig. 5.10.

Systematic uncertainty

The systematic uncertainty of the ϕ meson v_2 measurement was determined by varying all event and particle selections described above. Upper limits for allowed deviations due

---

[2] Note, the fitting ranges for $v_2^{Tot}(m_{inv})$ are not fixed: a number of possible fitting ranges (within certain limits) is tried. For each fit, the quality is checked by evaluating the χ^2 divided by degrees of freedom (DOF); the fit with the lowest χ^2/DOF value is chosen as best fit (the v_2 values obtained based on the best fits from a wider limits contribute to the systematic uncertainty of signal extraction, as will be explained in appendix **??**).

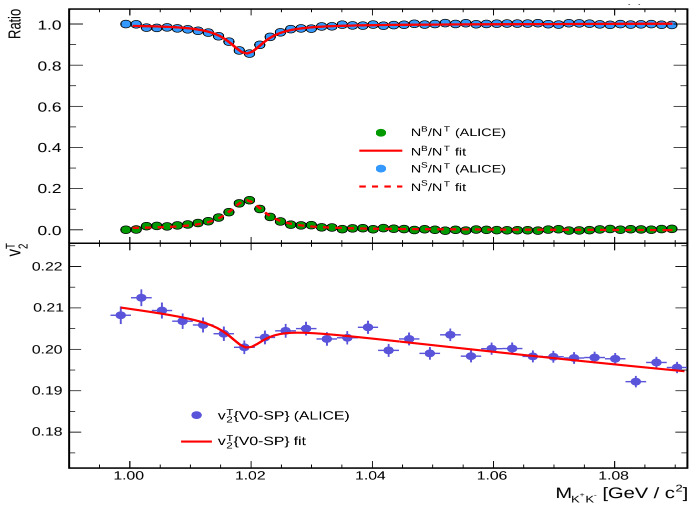

Figure 5.10: (Top) The ratio of $\frac{N^{Sig}}{N^{Tot}}(m_{inv})$ (green circle) and $\frac{N^{Bg}}{N^{Tot}}(m_{inv})$ (blue circle) as a function of invariant mass, the red dash and solid lines are the corresponding fits; (bottom) v_2 of kaon pairs measured by $v_2^T\{\mathrm{V0-SP}\}$, as a function of invariant mass. The red line is the fits for the $v_2^T\{\mathrm{V0-SP}\}$.

to the event selection and track selection were determined. In order to test the signal extraction procedure several different functions were used to describe the signal and background in the invariant mass distribution. The event-mixing technique, which takes random two tracks (particles) from two different events but similar physics condition (e.g. centrality, vertex), is widely used for the estimation of uncorrelated background. It was utilized for the combinatorial background subtraction in the ϕ meson reconstruction, as an additional systematic check in addition to Like-Sign subtraction. The observed difference of ϕ meson v_2 was included into systematic uncertainty. The uncertainty in the VZERO detector calibration, was estimated and propagated to a systematic uncertainty in the v_2 measurement. The final systematic systematic uncertainty was evaluated as the quadratic sum of the contributions from the above systematic checks. Details are summarized in Table 5.1.

Uncertainty sources	Centrality				
	10-20%	20-30%	30-40%	40-50%	50-60%
Event Selection	0.007	0.009	0.003	0.003	0.016
Track cuts	0.009	0.003	0.009	0.010	0.013
Signal extraction	0.004	0.001	0.002	0.003	0.
V0 calibration	0.002	0.002	0.	0.001	0.

Table 5.1: Table of systematic uncertainties for the ϕ meson v_2 measurements.

Extraction of ϕ meson v_2 from different methods

The v_2 of the ϕ meson was estimated also from other methods using the TPC detector, which apply a smaller pseudorapidity gap between two correlated particles. This was done in an attempt to evaluate the contribution from non-flow effects to the measurements. The p_T–differential v_2 of the ϕ meson, measured using the 2-particle Q-Cumulant ($v_2\{2\}$, red circle), Scalar Product ($v_2\{\mathrm{TPC}-\mathrm{SP}\}$, yellow circle) and Event Plane ($v_2\{\mathrm{TPC}-\mathrm{EP}\}$, blue circle) methods without $|\Delta\eta|$ gap based on TPC in 10-20 % are presented in Fig. 5.11 (left). A very good agreement is observed for the v_2 values measured with the three different methods. Good agreement is also seen in the relevant results obtained with the Scalar Product, shown in Fig. 5.11 (right) and Event Plane ($v_2\{\mathrm{V0}-\mathrm{EP}\}$, green triangle) methods with $|\Delta\eta|$ gap using TPC and VZERO detector.

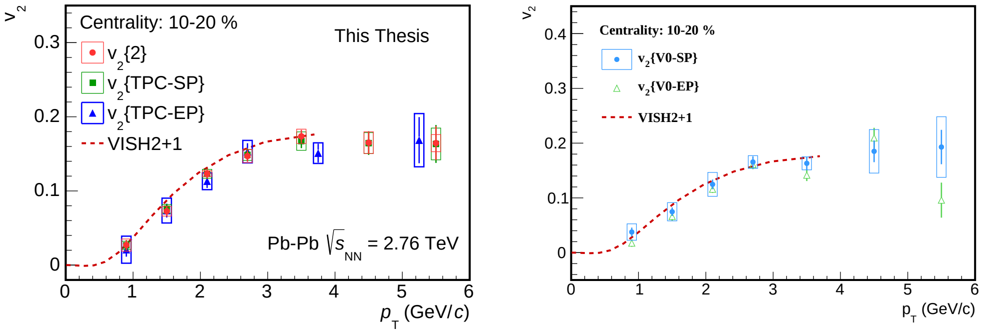

Figure 5.11: p_T–differential v_2 of the ϕ meson measured using the TPC (left) and the VZERO (right) for centrality 10-20%.

Figure 5.12 gives a complete picture of the centrality evolution of the p_T differential v_2 measured with the 2-particle cumulants using the TPC (left plot) and the Scalar Product method using the VZERO detector (right plot). A clear centrality dependence of the ϕ meson v_2 is observed. Generally speaking, the magnitude of v_2 is governed by the initial geometry and re-interactions of the collision. If the re-interactions are strong enough, the initial geometry anisotropy could be translated efficiently into the final anisotropic flow. In Fig. 5.12, we see that the magnitude of the ϕ meson v_2 progressively increases from central to peripheral collisions up to the 40-50% centrality interval. This is consistent with the picture that the final state anisotropic is dominated by the initial geometry anisotropy, as represented by the initial state eccentricity which increases for peripheral collisions. For more peripheral events (i.e. 50-60%), the magnitude of ϕ meson v_2 does not change significantly within the systematic uncertainties compared to the previous centrality interval. According to [179], this might originate from a convolution of different effects such as the smaller lifetime of the fireball in peripheral compared to more central collisions that does not allow ϕ meson v_2 to further develop, the less significant (compared to more central events) contribution of eccentricity fluctuations and to final state hadronic effects. It provides a hint that the hadronic interaction might play a role in the development of the ϕ meson v_2 in heavy ion collisions, especially in central collisions. The $p_{\rm T}$ differential v_2 of ϕ meson exhibits an almost linear increase up to 2 to 3 GeV/c. This initial rise is followed by a saturation and then a decrease is observed for all centralities.

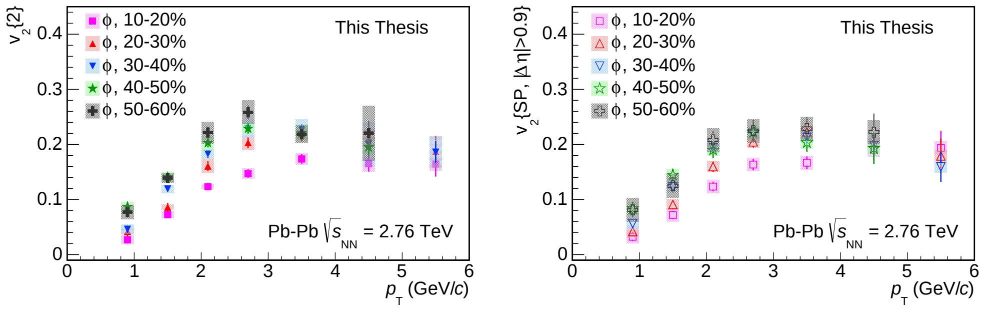

Figure 5.12: Centrality dependence of ϕ meson v_2 measured in TPC (left) and VZERO (right).

5.3.2 $\pi^{\pm}$, K$^{\pm}$, p($\overline{\rm p}$), ϕ, strange and multi-strange particle v_2

The elliptic flow v_2 is measured not only for the ϕ meson, but also for $\pi^{\pm}$, K, p+$\overline{\rm p}$, ϕ, Λ+$\overline{\Lambda}$, Ξ^-+$\overline{\Xi}^+$ and Ω^-+$\overline{\Omega}^+$ in Pb–Pb collisions at $\sqrt{s_{\rm NN}}$ = 2.76 TeV. These measurements, together with the comparisons to various theoretical calculations, can help us constrain the initial conditions and the dynamics of the collisions, i.e. the properties of the system (e.g. η/s) as well as probe the particle production mechanism (e.g. coalesence), for examples see [184].

The identification of $\pi^{\pm}$, K$^{\pm}$ and p($\overline{\rm p}$) is based on the combined information from the TPC and the TOF, shown in Fig. 5.8. Estimated from the Monte–Carlo (MC) simulations, the resulting purities are above 90% throughout the presented $p_{\rm T}$ range. The v_2 of $\pi^{\pm}$, K$^{\pm}$ and p+$\overline{\rm p}$ can be directly measured using the Q-Cumulant, Scalar Product and Event Plane methods. The measurements of K$^0_{\rm S}$, Λ($\overline{\Lambda}$) are studied via their weak decay channels: K$^0_{\rm S}$ $\rightarrow \pi^+ + \pi^-$ with a branching ratio 69.2% and $\Lambda \rightarrow {\rm p} + \pi^-$, $\overline{\Lambda} \rightarrow \overline{\rm p} + \pi^+$ with branching ratio 63.9%. The reconstructions of K$^0_{\rm S}$, Λ($\overline{\Lambda}$) are based on the reconstruction of the secondary vertex exhibiting a characteristic V-shape, called V0, defined by the trajectories of the decay products. The reconstruction of Ξ^-+$\overline{\Xi}^+$ and Ω^-+$\overline{\Omega}^+$ candidates is achieved via their decays channels $\Xi^- \rightarrow \Lambda + \pi^-$, $\overline{\Xi}^+ \rightarrow \overline{\Lambda} + \pi^+$ with branching ratio 99.9% and 67.8%, respectively. Topological and kinematic criteria were applied to first select the V0 decay products and then to match them with the secondary, bachelor track. Following the similar approach as discussed in Chapter 5.3.1, the invariant mass spectra of K$^0_{\rm S}$, Λ($\overline{\Lambda}$), Ξ^-($\overline{\Xi}^+$) and Ω^-($\overline{\Omega}^+$) are presented in Fig 5.13. After obtaining the $v_2^{Tot}(m_{inv})$ presented in Fig. 5.14, we can extract the v_2 of all the decaying particles by using the v_n versus m_{inv} method.

Figure 5.15 shows the $p_{\rm T}$-differential v_2 for $\pi^{\pm}$, K$^{\pm}$, p($\overline{\rm p}$), K$^0_{\rm S}$, ϕ, Λ($\overline{\Lambda}$), Ξ($\overline{\Xi}$) and Ω($\overline{\Omega}$) in different centrality classes. For the low $p_{\rm T}$ region (i.e. $p_{\rm T} \leq 3$ GeV/c), one can

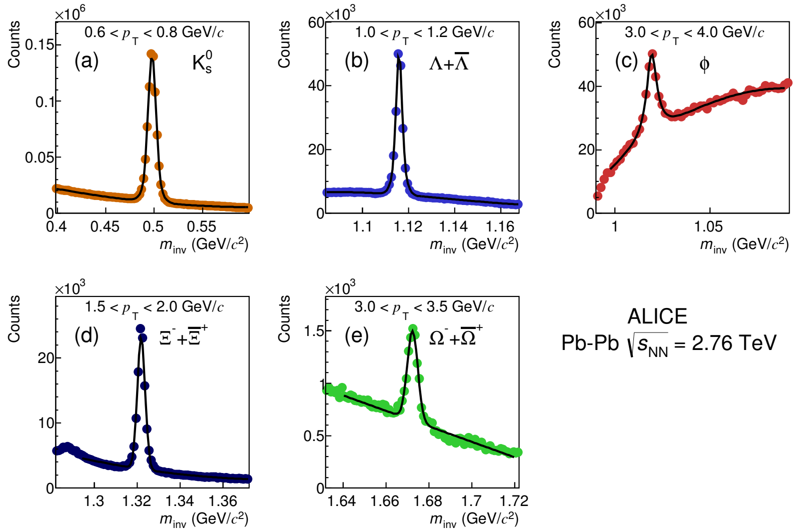

Figure 5.13: Invariant mass distributions for econstructed decaying particles: (a) K^0_S, (b) $\Lambda+\overline{\Lambda}$, (c) ϕ, (d) Ξ^- ($\overline{\Xi}^+$), and (e) Ω^- ($\overline{\Omega}^+$) in the 10–20% centrality interval of Pb–Pb collisions.

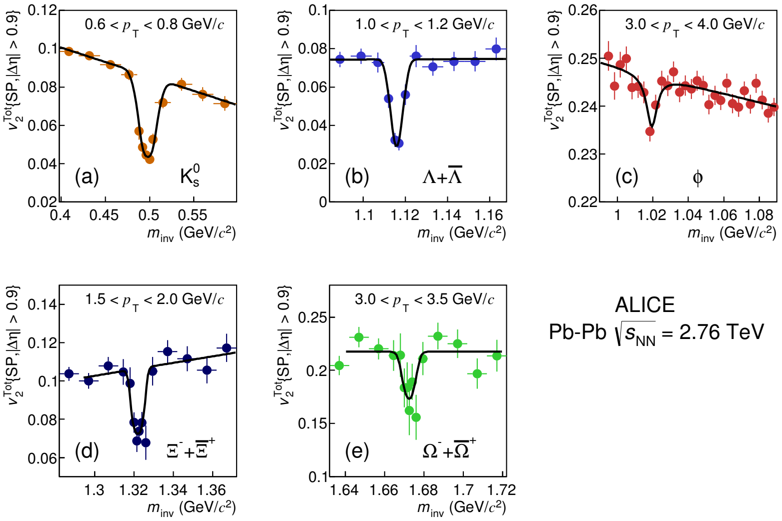

Figure 5.14: The $v_2^{\rm Tot}$ as a function of the invariant mass for all decaying particles in the 10–20% centrality in Pb–Pb collisions.

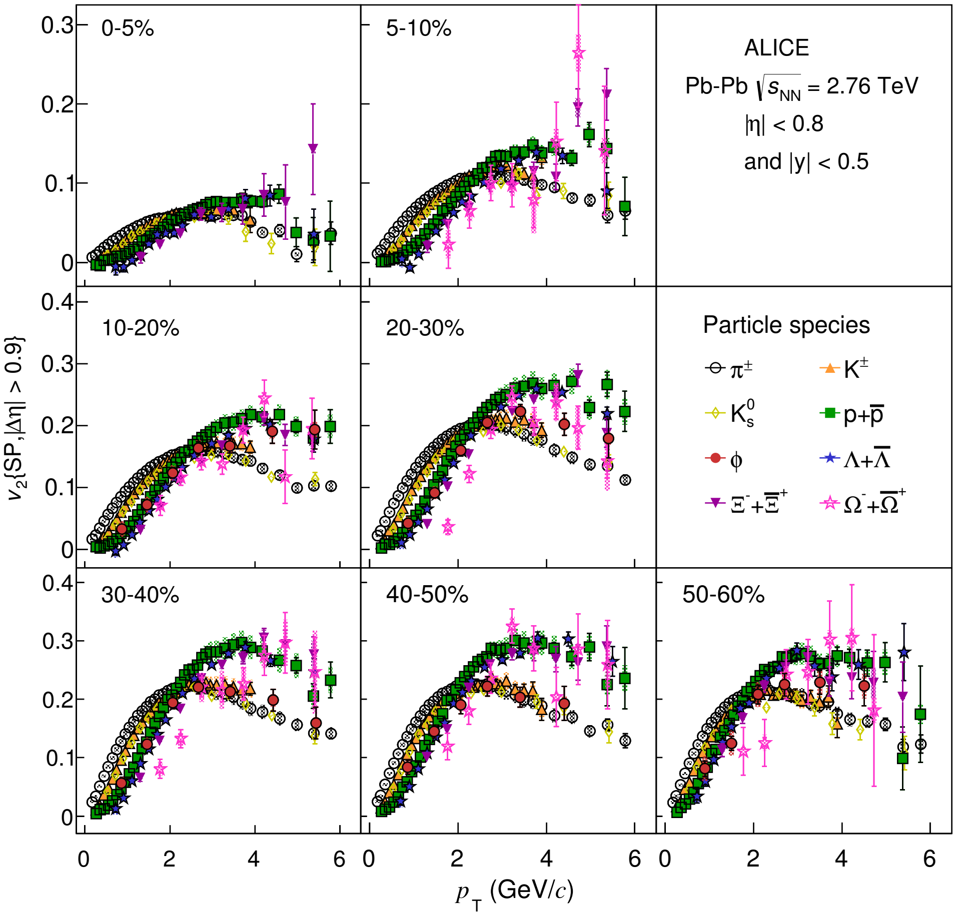

Figure 5.15: The centrality dependence of p_T–differential v_2 for different particle species in Pb–Pb collisions at $\sqrt{s_{NN}}$ =2.76 TeV.

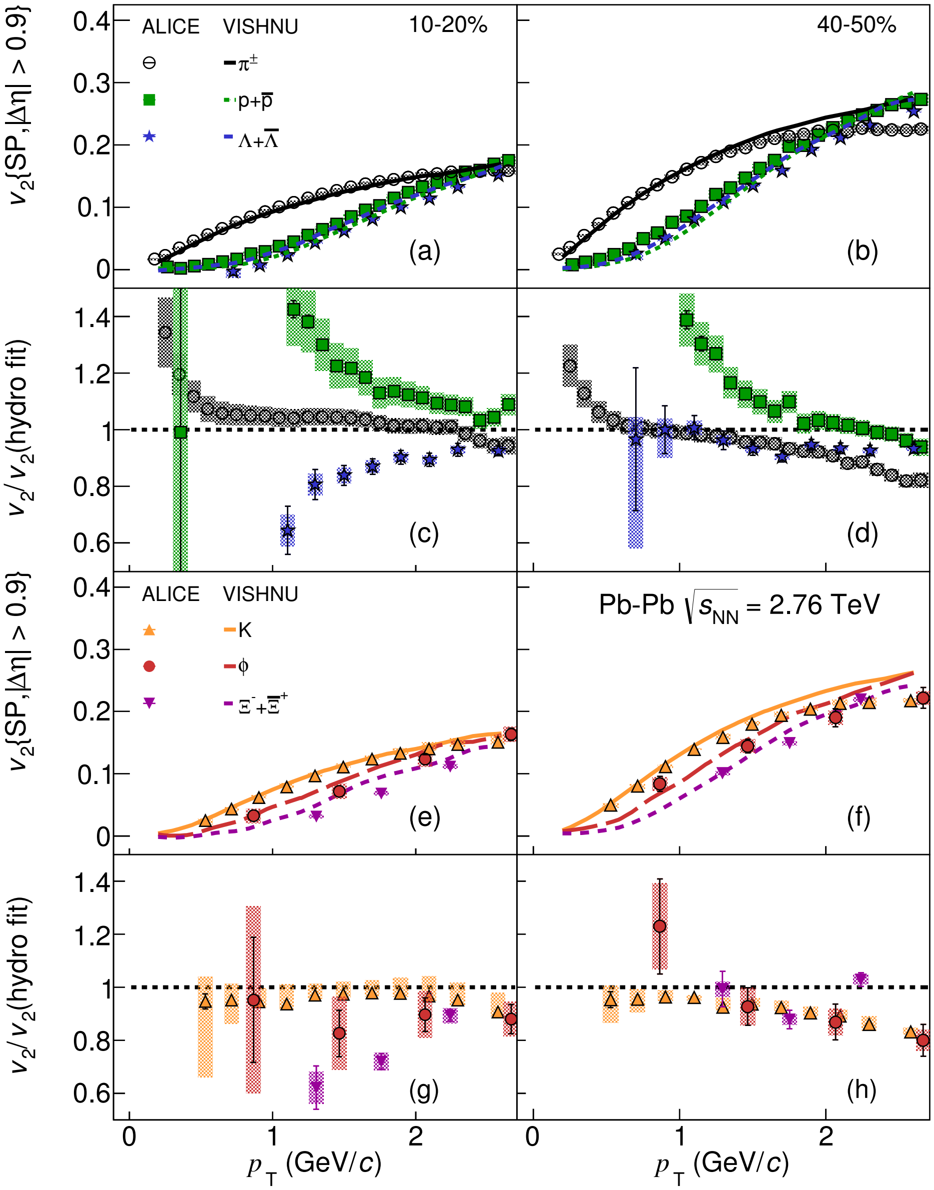

Figure 5.16: The p_{T}-differential v_2 for different particle species in (a), (b), (e), (f), measured with the scalar product method with a pseudo-rapidity gap $|\Delta\eta| > 0.9$ in Pb–Pb collisions at $\sqrt{s_{\mathrm{NN}}} = 2.76$ TeV, compared to hydrodynamic calculations (VISHNU). The panels (c), (d), (g) and (h), show the dependence of the ratio of the experimental points to a fit over the hydrodynamic calculations as a function of p_{T}. The left and right plots present the comparison for the 10–20% and 40–50% centrality intervals, respectively.

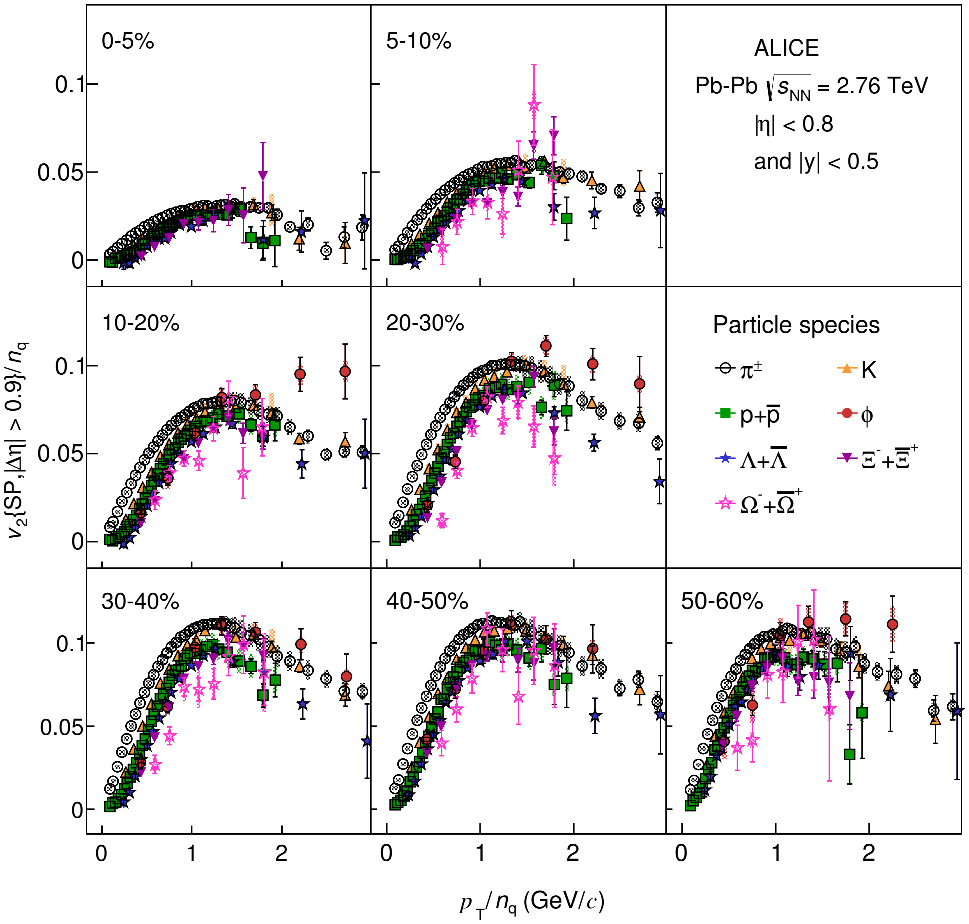

Figure 5.17: The p_{T}/n_q dependence of v_2/n_q for $\pi^{\pm}$, K, p+$\overline{\mathrm{p}}$, ϕ, Λ+$\overline{\Lambda}$, Ξ^-+$\overline{\Xi}^+$ and Ω^-+$\overline{\Omega}^+$ for Pb–Pb collisions in various centrality intervals at $\sqrt{s_{\mathrm{NN}}} = 2.76$ TeV.

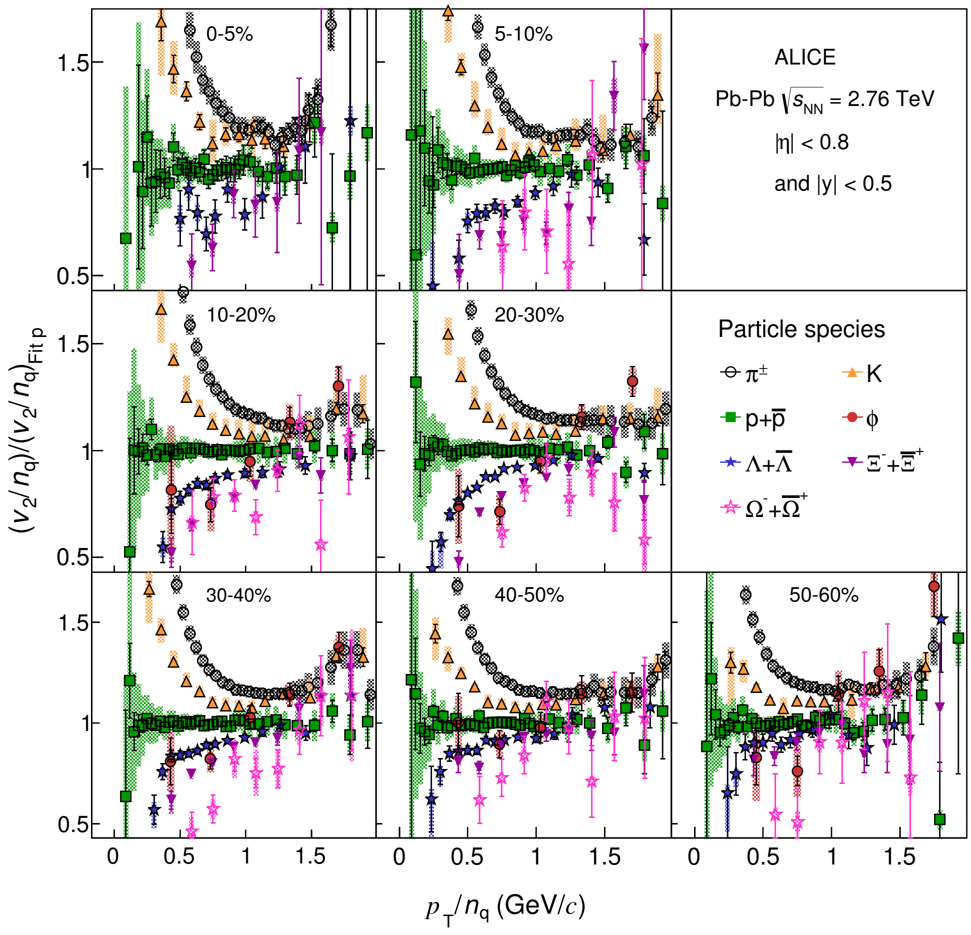

Figure 5.18: The p_{T}/n_q dependence of the double ratio of v_2/n_q for every particle species relative to a fit to v_2/n_q of p and $\bar{\mathrm{p}}$ for Pb–Pb collisions at $\sqrt{s_{\mathrm{NN}}} = 2.76$ TeV.

see a rather clear evidence for mass ordering ($v_2^{\pi} < v_2^{\mathrm{K}} < v_2^{\mathrm{p}} \leq v_2^{\phi} < v_2^{\Lambda} < v_2^{\Xi} < v_2^{\Omega}$). This is expected due to the interplay between elliptic and radial flow [181, 189] as we discussed above. This ordering is followed by a crossing between the v_2 values of different particles, which takes place between 2 and 3.5 GeV/c, depending on the particle species and centrality. For higher values of p_{T} ($p_{\mathrm{T}} > 3$ GeV/c), particles tend to group according to their type, i.e. mesons and baryons. This feature will be discussed in detail in Chapter 5.3.2.

The multi-strange baryons, i.e. $\Xi^- + \overline{\Xi}^+$ and $\Omega^- + \overline{\Omega}^+$, with their large mass and presumably small hadronic cross sections should be less sensitive to hadronic rescattering in the later stages of the collisions and therefore are, as in the case of the ϕ meson, a probe of the early stage of the collisions.

Fig. 5.15 shows that v_2 of $\Xi^-(\overline{\Xi}^+)$ increases with p_{T}, reaching a saturation at $p_{\mathrm{T}} \approx$ 4 GeV/c, depending on the centrality interval, which is similar to the results for $\Lambda(\overline{\Lambda})$. The v_2 of $\Omega(\overline{\Omega})$ is clearly non-zero, lower than $\Xi^-(\overline{\Xi}^+)$ v_2 at low p_{T} and consistent with $\Xi^-(\overline{\Xi}^+)$ v_2 at intermediate p_{T}. It is clear that both $\Xi^-(\overline{\Xi}^+)$ and $\Omega(\overline{\Omega})$ respect the mass ordering at low p_{T} while they follow the baryon band formed by the $\mathrm{p}(\overline{\mathrm{p}})$ and $\Lambda(\overline{\Lambda})$ at intermediate p_{T}. Assuming that multi-strange baryons are less affected by the hadronic interactions and v_2 develops primarily at the early stage of the collisions, the measured large v_2 indicate that partonic collectivity is generated at the LHC.

As we discussed above, the ϕ meson is of particular interest because it provides an excellent test of both the mass ordering and/or the baryon-meson grouping. Figure 5.15 shows that the v_2 of the ϕ meson lays within errors between those of the lighter (e.g. $\mathrm{K}^{\pm}$, p) and heavier (e.g. Λ, Ξ) particles at low p_{T} ($p_{\mathrm{T}} < 3$ GeV/c) for all centrality intervals, which confirms the mass-ordered hierarchy. Different from what was observed at RHIC, the ϕ meson v_2 seems to follow, within uncertainties, the group of baryons in central collisions, and shifts progressively to the group of mesons for peripheral collisions, in the intermediate p_{T} region. An additional measurement sensitive to the ϕ meson production mechanism is looking at the p/ϕ ratio as a function of p_{T} in ALICE [183]. If the production of ϕ mesons and $\mathrm{p}(\overline{\mathrm{p}})$ is described within a hydrodynamic framework, their p_{T} distributions and v_2 are expected to have similar shapes, despite the difference of their quantum numbers. In fact, the p/ϕ ratio shows an almost independent trend with p_{T} in central collisions while decreases with increasing p_{T} in peripheral collisions [183]. This flat p/ϕ ratio in central collisions indicate that the shape of the p_{T} distributions at low and intermediate p_{T} are determined by the mass of the particles at LHC. The coalesce mechanism, which generate the p_{T} distributions and v_2 related to the quantum number, is challenged by the particle spectra and elliptic flow measurements of at low and intermediate p_{T} in central Pb–Pb collisions.

comparison with hydrodynamical calculations

Early viscous hydrodynamic calculations revealed that the shear viscosity of the QGP suppresses the fluid anisotropy and therefore can be extracted from the anisotropic flow measurements [184]. However, hadronic chemical compositions and off-equilibrium kinetics also influence significantly the development of flow, which brings a large uncertainty for the extracted shear viscosity of the QGP. In order to better describe the

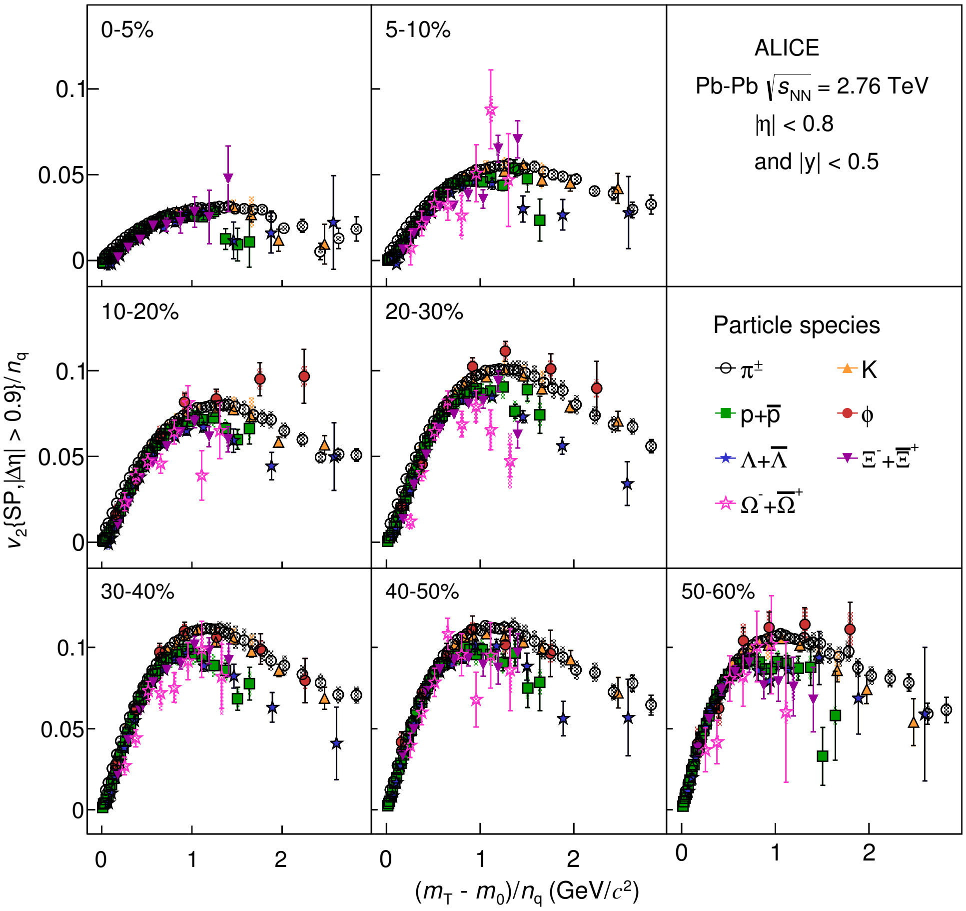

Figure 5.19: The $(m_T - m_0)/n_q$ dependence of v_2/n_q for $\pi^{\pm}$, K, p+$\overline{\text{p}}$, ϕ, Λ+$\overline{\Lambda}$, Ξ^-+$\overline{\Xi}^+$ and Ω^-+$\overline{\Omega}^+$ for Pb–Pb collisions in various centrality intervals at $\sqrt{s_{NN}}$ = 2.76 TeV.

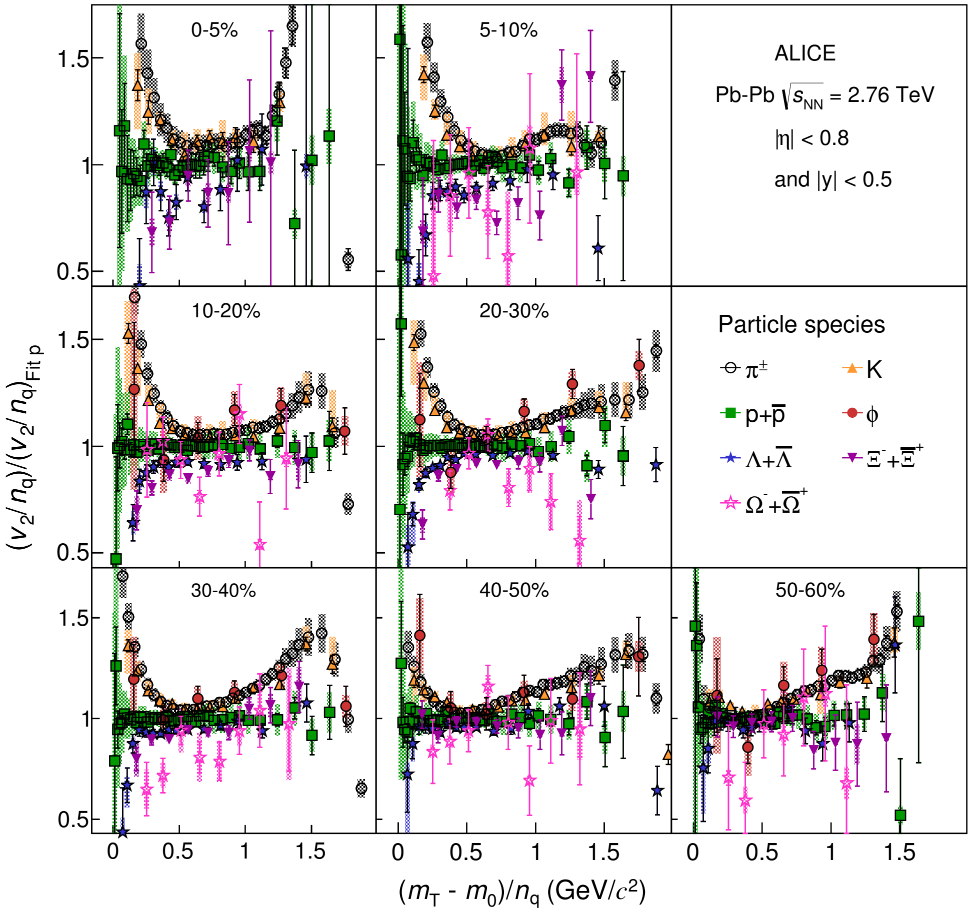

Figure 5.20: The p_{T}/n_q dependence of the double ratio of v_2/n_q for every particle species relative to a fit to v_2/n_q of p and p (see text for details) for Pb–Pb collisions at $\sqrt{s_{\mathrm{NN}}} = 2.76$ TeV.

hadronic matter, hybrid models have been developed by coupling viscous hydrodynamics for the QGP fluid expansion with a hadron cascade model, to describe the microscopic evolution and decoupling of the hadronic matter [184]. Nice agreement of identified particle spectra and elliptic flow from hybrid hydrodynamic calculations and experimental measurements have been observed [184].

Fig. 5.16 shows the comparison of identified particle v_2 measurements and the viscous hydrodynamical calculation VISHNU, which is based on initial conditions modeled by MC-KLN and a $\eta/s = 0.16$. Here (a), (b), (e), (f), present the p_{T}-differential v_2 for different particle species, while (c), (d), (g) and (h) show the ratio of the experimental points over a fit to the hydrodynamic calculations as a function of p_{T}. The VISHNU calculations generate the main feature of mass ordering for the v_2 of most particle species at low p_{T}, which roughly agrees with data. However, a closer look reveals that VISHNU calculations of $\pi^{\pm}$ and $\mathrm{p}(\overline{\mathrm{p}})$ v_2 are systematically below the measured v_2, while the calculations of $\mathrm{K}^{\pm}$ v_2 nicely describe the data points. In addition, v_2 of all heavier particles, e.g. ϕ meson, strange and multi-strange particle, are overestimated in this hybrid hydrodynamic calculations. It is noticed that in the VISHNU model, the ϕ and $\Lambda(\overline{\Lambda})$ v_2 calculations not follow the mass ordering at low p_{T} region. All these results suggest that ϕ meson, strange and multi-strange particles might either freeze-out later than what the current implementation of VISHNU expects, and/or their hadronic cross sections are underestimated in UrQMD model. Thus, further knowledge about freeze-out condition (e.g. radial flow, freeze-out temperature) and better constraints of the hadronic cross section of the ϕ meson, strange and multi-strange particles are still necessary to improve the hydrodynamic calculations.

Number of constituent quark scaling

The scaling with the number of constituent quarks, named NCQ scaling, was used to support the picture that the collectivity already develops at the partonic level at top RHIC energy [72, 185]. It can also serve as a test of hadron production via quark coalescence/recombination mechanism.

The v_2 scaled by the number of constituent quarks (n_q) as a function of p_{T}/n_q for all particle species and centrality intervals are shown in Fig. 5.17. An approximate scaling behaviour is observed for the intermediate transverse momentum region (i.e. 2-3 $< p_{\mathrm{T}} <$ 5-6 GeV/c) [72, 185], and it was nicely described by the coalescence mechanism [193]. Similar approximate NCQ scaling pictures could be also found in other centrality intervals. In order to quantify to which extend the scaling exists, we calculate the ratio of (v_2/n_q) for each particle to the fit on v_2/n_q for $\mathrm{p}(\overline{\mathrm{p}})$ as a function of p_{T}/n_q. The results of such 'double ratio' for the various centrality intervals are presented in Fig. 5.18. It is clear that the number of constituent quark scaling does not hold perfectly, the deviations of this scaling from unity are at the level of ±20% for all centrality classes.

On the other hand, the scaling of v_2/n_q vs KE_{T}/n_q, suggested by PHENIX Collaboration, could remove the mass effects (different contributions for particles with different mass) and extend the universal scaling to a lower p_{T} region [187] (here $KE_{\mathrm{T}} = m_{\mathrm{T}} - m_0$ and $m_{\mathrm{T}} = \sqrt{p_{\mathrm{T}}^2 + m_0^2}$ is the transverse mass). The $(m_{\mathrm{T}} - m_0)/n_q$ (or KE_{T}/n_q) dependence of v_2/n_q is shown in Fig. 5.19. It is seen that although the mass effect was supposed to be removed in the KE_{T} scaling, significant deviations for $(m_{\mathrm{T}} - m_0)/n_q <$

0.6 - 0.8 GeV/c^2 are still observed at the LHC. Furthermore, the v_2/n_q versus $KE_{\rm T}$ scaling, holds only approximately for the intermediate $KE_{\rm T}$ region in the presented centrality classes. To quantify these deviations, in Fig. 5.20 the $(m_{\rm T} - m_0)/n_q$ dependence of v_2/n_q for p($\bar{\rm p}$) is fitted with a seventh order polynomial function and the double ratio of $(v_2/n_q)/(v_2/n_q)_{Fitp}$ for each particle species is then formed. For low $p_{\rm T}$ (or $(m_{\rm T} - m_0)/n_q < 0.6$ - 0.8 GeV/c^2), the scaling is broken while for intermediate $p_{\rm T}$ the scaling hold approximately, with deviations at the level of ±20% with respect to the reference ratio for all centrality intervals.

5.3.3 Higher harmonics of identified particles

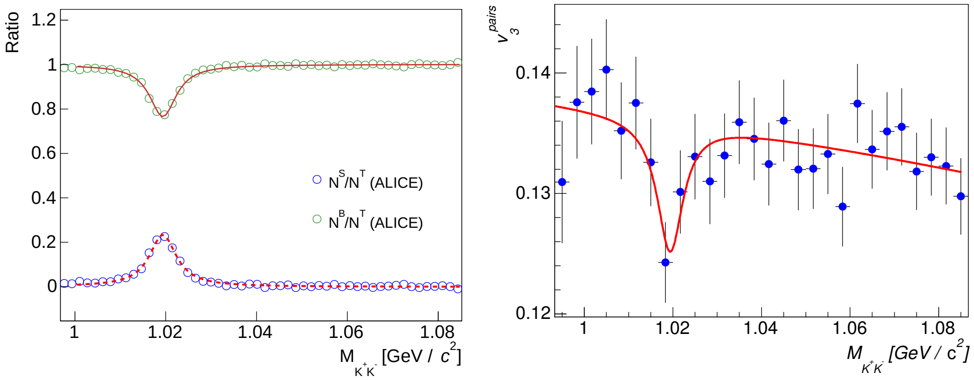

Figure 5.21: (Left) The ratio of $\frac{N^{Sig}}{N^{Tot}}(m_{inv})$ (green circle) and $\frac{N^{Bg}}{N^{Tot}}(m_{inv})$ (blue circle) as a function of invariant mass, the red dash and solid lines are the corresponding fits; (Right) v_3 of kaon pairs as a function of invariant mass measured by 2-particle Q-Cumulant method. The red line is the fits for the $v_3\{2\}^T$.

Most attention has been paid to the v_2 measurements to obtain the initial state conditions and the extraction of the specific shear viscosity over entropy density ratio η/s. However, the uncertainty for η/s remains large, primarily because of an uncertainty in the initial state geometry used in model calculations (e.g. $\eta/s \sim 0.16 - 0.20$ with an initial state model using MC-KLN and $\eta/s \sim 0.08$ from a MC-Glauber model). Recent results suggest that the higher harmonic anisotropic flow v_n ($n > 2$) of inclusive charged hadrons provide tighter constraints for disentangling the role of the initial state geometry, its fluctuations and η/s [122]. The identified particle v_3 measurements, as well as the comparison of hydrodynamic calculations, will help us to further understand the interplay of the radial and triangular expansion.

The ϕ meson v_3 can be obtained using the v_n versus invariant mass method which was also used for the v_2 calculations. The reconstruction of the ϕ meson, the ratio of N^S/N^T and N^B/N^T as a function of m_{inv} are presented in Fig. 5.21 (Left). In order to extract the ϕ meson v_3 via Eq. 5.2, the $v_3^T(m_{inv})$ is first measured with 2-particle Q-Cumulant method, illustrated by Fig. 5.21 (Right). The centrality dependence of the

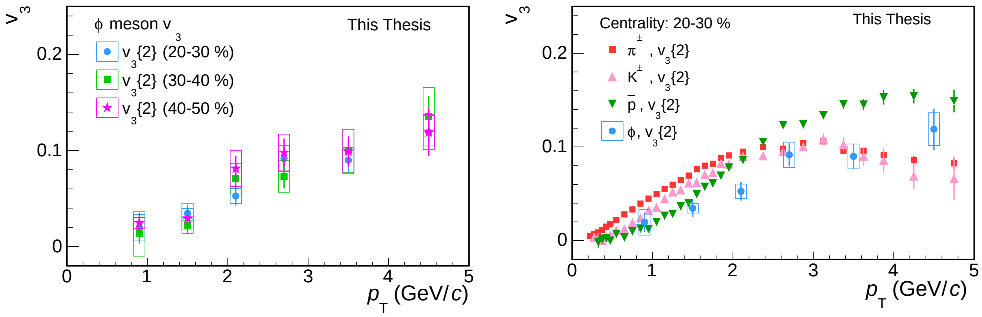

Figure 5.22: The centrality dependence of p_{T}–differential v_3 for ϕ meson in Pb–Pb collisions at $\sqrt{s_{\mathrm{NN}}}$ =2.76 TeV (left). The p_{T}-differential v_3 for different particle species for centrality 20-30 % in Pb–Pb collisions at $\sqrt{s_{\mathrm{NN}}}$ =2.76 TeV.

p_{T}–differential v_3 of the ϕ meson are shown in Fig. 5.22 (Left). Similar to the centrality dependence of inclusive charged hadron v_3 [122], a weak centrality dependence of ϕ meson v_3 is observed.

The comparison of the ϕ meson v_3 to $\pi^{\pm}$, $\mathrm{K}^{\pm}$ and $\overline{\mathrm{p}}$ in the 20–30% centrality class is presented in Fig. 5.22 (right). The v_3 of identified particles exhibits similar features as the those of v_2. It shows a clear mass ordering at low p_{T}, which might be attributed to the interplay between radial and triangular flow. A simple test shows that if we introduce the concept of triangularity into a simple Blast-wave model [167], indeed one can generate mass dependent v_3. The comparison to existing hydrodynamic calculations of identified particle v_3 ($\pi^{\pm}$, $\mathrm{K}^{\pm}$, $\overline{\mathrm{p}}$) in centrality 10-20% and 40-50% are presented in Fig. 5.23 (Left) and (Right), respectively. A distinct mass ordering is observed in both central and peripheral collisions in hydrodynamic calculations with both MC-KLN initial condition with η/s = 0.20 and with MC-Glauber initial condition with η/s = 0.08. However, none of the calculations quantitatively reproduce the magnitude of v_3 in both centrality classes.

It is also seen in Fig. 5.23 that v_3 of $\overline{\mathrm{p}}$ cross $\pi^{\pm}$ at $p_{\mathrm{T}} \sim 2.5$ GeV/c while also there is a baryon-meson grouping at the intermediate p_{T} range, as expected from the quark coalescence mechanism. Although the v_3 of ϕ meson is close to $\overline{\mathrm{p}}$ at low p_{T}, it seems to group with other mesons (e.g. $\pi^{\pm}$ and $\mathrm{K}^{\pm}$) v_3 in intermediate p_{T} region. In order to check the scaling properties of v_3, the p_{T}/n_q and KE_{T}/n_q dependence of v_3/n_q are presented in 20-30% in Fig. 5.24 (left) and (right), respectively. It is found that there is no NCQ scaling for v_3/n_q versus p_{T}/n_q, while KE_{T} scaling works better for v_3 than for v_2, which shown in Fig. 5.19, but it is still only approximate as can be seen in Fig. 5.24 (right).

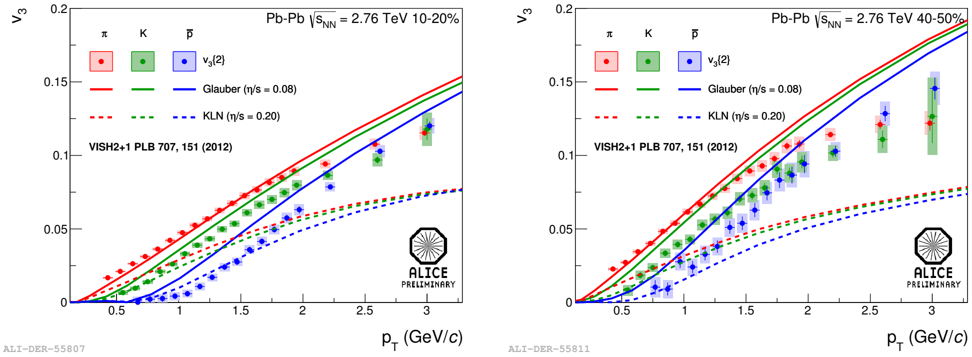

Figure 5.23: The $p_{\rm T}$-differential v_3 for different particle species and the comparison to hydrodynamic calculations (VISH2+1) for centrality 10-20 % (left) and 40-50 % in Pb–Pb collisions at $\sqrt{s_{\rm NN}}$ =2.76 TeV.

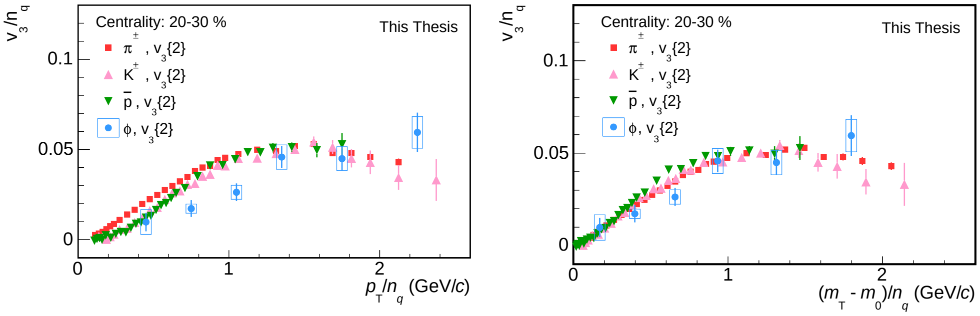

Figure 5.24: The $p_{\rm T}/n_q$ dependence of v_3/n_q for $\pi^{\pm}$, $\mathrm{K}^{\pm}$, p+p̄, ϕ for Pb–Pb collisions in 20-30 % centrality interval at $\sqrt{s_{\rm NN}}$ = 2.76 TeV.

Chapter 6

Flow fluctuations at LHC

Initial event-by-event geometry fluctuations not only lead to the fluctuations of even harmonic anisotropic flow, but also generate non-zero odd harmonics. In fact, this initial fluctuations lead to $\langle v_n^k \rangle \neq \langle v_n \rangle^k$ and the development of different order participant planes Ψ_n. Thus, a comprehensive understanding of both initial state geometry fluctuations and their effects on the final state anisotropic flow is crucial for the comparison of theory and experiments.

In this chapter, four main questions will be discussed in detail, namely:

- How do v_n and ε_n fluctuate and what is the underlying probability density function (*p.d.f.*) of their distributions;
- How are the initial geometry fluctuations reflected in differential flow measurements;
- What is the relationship between different harmonic participant planes Ψ_n and Ψ_m $(n \neq m)$;
- What is the relationship between the flow coefficients of different harmonic v_n and v_m $(n \neq m)$.

6.1 Searches of the underlying *p.d.f.* of event-by-event flow fluctuations

The consequence of initial event-by-event geometry fluctuations is the fact that $\langle v_n^k \rangle \neq \langle v_n \rangle^k$, where the moments $\langle v_n^k \rangle$ are defined as:

$$\langle v_n^k \rangle \equiv \int v_n^k f(v_n) \mathrm{d}v_n, \tag{6.1}$$

and $f(v_n)$ is the underlying *p.d.f.*.

Traditionally, the flow measurements try to explore the first moment of the distribution i.e. the mean value of the *p.d.f.* which is the anisotropic flow from the symmetry plane. This is hardly enough to describe a broad range of dynamic phenomena since different *p.d.f.* could generate accidentally the same $\langle v_n \rangle$. Thus, one should try to reconstruct the underlying *p.d.f.* by as many moments, or equivalently cumulants, as possible. Whether the *p.d.f.* could be reconstructed uniquely from the measured moments, or whether the equivalence "*p.d.f.* ⇔ moments" holds true could be checked by the Krein conditions [210, 211]. Several possible candidates for the underlying *p.d.f.* of v_n or ε_n are proposed. For the sake of simplicity, the ε_n distributions are used as an example in the following discussions while the conclusions should be similar for both v_n and ε_n. A popular parameterisation of ε_n is the Bessel-Gaussian distributions [89]:

$$p(\varepsilon_n) = \frac{\varepsilon_n}{\sigma^2} I_0 \left(\frac{\varepsilon_0 \varepsilon_n}{\sigma^2} \right) \exp \left(-\frac{\varepsilon_0^2 + \varepsilon_n^2}{2\sigma^2} \right) \tag{6.2}$$

where I_0 is a modified Bessel function, ε_0 is the anisotropy *w.r.t.* the reaction plane and σ denotes the fluctuations of the anisotropy. It is found that the ε_2 distributions are described fairly well by a Bessel-Gaussian parameterization in mid-central collisions ($4 < b < 6$ fm) [89]. The agreement becomes worse in peripheral collisions, since there are no constrains like $\varepsilon_2 < 1$ in each event [223]. In [224], a simple one-parameter (i.e. α in Eq. (6.3)) power-law distribution was proposed:

$$p(\varepsilon_n) = 2\alpha\, \varepsilon_n \left(1 - \varepsilon_n^2\right)^{\alpha - 1}, \tag{6.3}$$

to parameterize the fluctuations driven anisotropies [224]. Recently, another function, called Elliptic-Power [223], which might describe the ε_n distributions in both nucleus-nucleus and proton-nucleus, was suggested as the candidate for underlying *p.d.f.*. It is defined as:

$$p(\varepsilon_n) = \frac{\alpha\, \varepsilon_n}{\pi} \left(1 - \varepsilon_0^2\right)^{\alpha + \frac{1}{2}} \int_0^{2\pi} \frac{\left(1 - \varepsilon_n^2\right)^{\alpha - 1} \mathrm{d}\phi}{\left(1 - \varepsilon_0\, \varepsilon_n \cos\phi\right)^{2\alpha + 1}}, \tag{6.4}$$

where α and ε_n have the same meaning as above.

In this thesis, we will not only study the mean (the anisotropic flow *w.r.t.* the corresponding symmetry plane), the standard deviation (the "typical" flow fluctuations) of the underlying *p.d.f.*, but also the higher order cumulants. The expectations from three candidate functions will be tested with the cumulant results.

6.1.1 Mean and standard deviation of the underlying p.d.f.

One of the goals of this thesis is to combine the initial state information obtained from Monte Carlo models (which work on heavy ion collisions), and the experimental measurements of anisotropic flow (in terms of different order cumulants), and study the response of the system to geometry fluctuations as reflected in the final state.

There are several Monte Carlo models, for instance MC-Glauber [196] and MC-KLN (CGC) [197], that attempt to describe the initial conditions. The initial anisotropy ε_n can be obtained from these initial state models via [97]:

$$\varepsilon_n = \frac{\sqrt{\langle r^n \cos n\varphi \rangle^2 + \langle r^n \sin n\varphi \rangle^2}}{\langle r^n \rangle}, \tag{6.5}$$

where $(r,\, \varphi)$ are polar coordinates of each participating nucleon in the collisions [1]. The parameter ε_2 is usually referred to as eccentricity and ε_3 as triangularity.

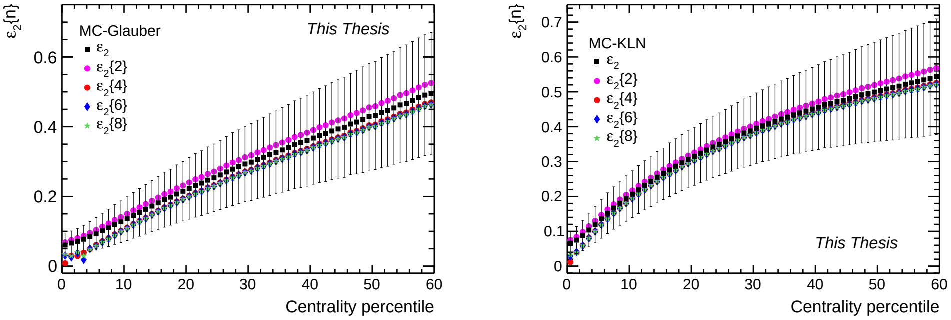

Figure 6.1: Centrality dependence of ε_2 for 2-, 4-, 6- and 8-particle cumulant from MC-Glauber model with number of wounded nucleon as weight (Left) and MC-KLN CGC model (Right).

A typical way to study fluctuations is using 2- and higher-order cumulants:

$$\begin{aligned}
\varepsilon_n\{2\} &= \langle \varepsilon_n^2 \rangle^{1/2} \\
\varepsilon_n\{4\} &= \left[2\langle \varepsilon_n^2 \rangle^2 - \langle \varepsilon_n^4 \rangle \right]^{1/4} \\
\varepsilon_n\{6\} &= \left[(1/4) \cdot \left(\langle \varepsilon_n^6 \rangle - 9\langle \varepsilon_n^4 \rangle \langle \varepsilon_n^2 \rangle + 12\langle \varepsilon_n^2 \rangle^3 \right) \right]^{1/6} \\
\varepsilon_n\{8\} &= \left[-(1/33) \cdot \left(\langle \varepsilon_n^8 \rangle - 16\langle \varepsilon_n^6 \rangle \langle \varepsilon_n^2 \rangle - 18\langle \varepsilon_n^4 \rangle^2 + 144\langle \varepsilon_n^4 \rangle \langle \varepsilon_n^2 \rangle^2 - 144\langle \varepsilon_n^2 \rangle^4 \right) \right]^{1/8} .
\end{aligned} \tag{6.6}$$

For a Gaussian distribution, in the case of small fluctuations $\sigma_{\varepsilon_n} \ll \langle \varepsilon_n \rangle$,

$$\begin{aligned}
\varepsilon_n\{2\}^2 &= \langle \varepsilon_n \rangle^2 + \sigma_{\varepsilon_n}^2 \\
\varepsilon_n\{4\}^2 &\approx \langle \varepsilon_n \rangle^2 - \sigma_{\varepsilon_n}^2 \\
\varepsilon_n\{6\}^2 &\approx \langle \varepsilon_n \rangle^2 - \sigma_{\varepsilon_n}^2 \\
\varepsilon_n\{8\}^2 &\approx \langle \varepsilon_n \rangle^2 - \sigma_{\varepsilon_n}^2 .
\end{aligned} \tag{6.7}$$

where $\langle \varepsilon_n \rangle$ is the mean anisotropy relative to the participant plane and σ_{ε_n} is the standard deviation of anisotropy fluctuations [89]. They correspond to the first and second order moments of the underlying $p.d.f.$.

The centrality dependence of $\varepsilon_2\{2\}$, ε_2 and $\varepsilon_2\{4\}$ is presented in Fig. 6.1. Although the magnitude and shape of ε_2 from MC-Glauber and MC-KLN are not exactly the same, similar trends of $\varepsilon_2\{2\}$, ε_2 and $\varepsilon_2\{4\}$ are expected. In particular, $\varepsilon_2\{2\} > \varepsilon_2 > \varepsilon_2\{4\}$ is observed in both models. This observation supports the idea that $\varepsilon_2\{2\}$ and $\varepsilon_2\{4\}$ have different sensitivities to anisotropy fluctuations, as expected from Eq. (6.7).

---

[1] The r^2 weight was also tested in Eq. 6.5 which gives similar results for ε_n.

With $\varepsilon_n\{2\}$ and $\varepsilon_n\{4\}$, the relative anisotropy fluctuations can be estimated via $F(\varepsilon_n)$ defined as:

$$F(\varepsilon_n) = \sqrt{\frac{\varepsilon_n^2\{2\} - \varepsilon_n^2\{4\}}{\varepsilon_n^2\{2\} + \varepsilon_n^2\{4\}}} \approx \frac{\sigma_{\varepsilon_n}}{\langle\varepsilon_n\rangle}. \tag{6.8}$$

Considering σ_{ε_n} and $\langle\varepsilon_n\rangle$ are known in MC-Glauber [196] and MC-KLN models [197], we can check if the estimated relative eccentricity fluctuations calculated with $\varepsilon_n\{2\}$, $\varepsilon_n\{4\}$ are compatible to the relative eccentricity fluctuations $\sigma_{\varepsilon_n}/\langle\varepsilon_n\rangle$ which are directly obtained from the initial state models. The comparisons of $F(\varepsilon_2)$ and $\sigma_{\varepsilon_2}/\langle\varepsilon_2\rangle$ from both MC-Glauber model (in grey) and MC-KLN model (in red) are presented in Fig. 6.2. First of all, we see $F(\varepsilon_2)$ roughly agree with $\sigma_{\varepsilon_2}/\langle\varepsilon_2\rangle$ for centralities 20-50% in MC-Glauber model and centralities 10-50 % for MC-KLN model. Deviations are observed in most central collisions for both models, because for these centralities the $\sigma_{\varepsilon_2} \ll \langle\varepsilon_2\rangle$ is not valid. The $\sigma_{\varepsilon_2}/\langle\varepsilon_2\rangle$ both in MC-Glauber model and MC-KLN model saturates around 0.52 in most central collisions, which agrees with the Bessel-Gaussian fluctuations limit $\sqrt{4/\pi - 1}$ in the case of only fluctuations [89, 195].

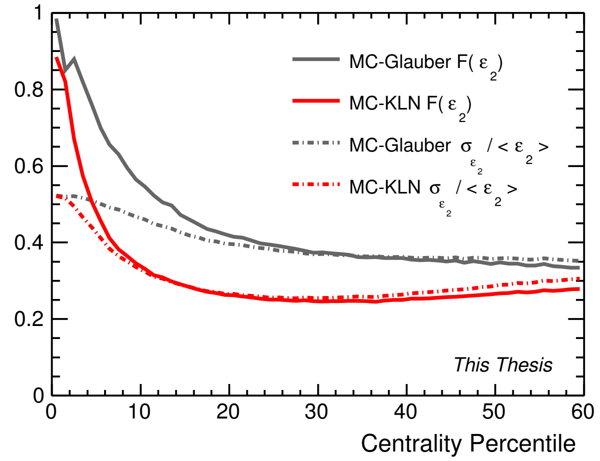

Figure 6.2: Centrality dependence of relative eccentricity fluctuations. The solid and dash lines are for $F(\varepsilon_2)$ and $\sigma_\varepsilon/\langle\varepsilon_2\rangle$ from MC-Glauber (grey) and MC-KLN (red), respectively.

Both ideal and viscous hydrodynamic calculations have shown that in a given event v_n exhibits a linear response to the initial anisotropy ($v_n = k_n\,\varepsilon_n$). Such assumption works quite well for $n = 2$, 3 [207]. Therefore, if we replace ε_n with v_n in Eq. (6.6), we

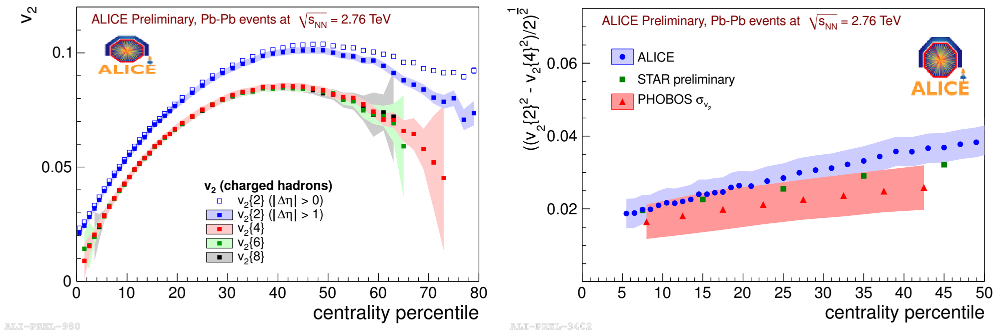

Figure 6.3: (Left) Centrality dependence of charged particle v_2 measured by 2- and multi-particle cumulant; (Right) Relative flow fluctuations as a function of centrality.

have:

$$\begin{aligned}
v_n\{2\} =& \langle v_n^2\rangle^{1/2}, \\
v_n\{4\} =& \left[2\langle v_n^2\rangle^2 - \langle v_n^4\rangle\right]^{1/4}, \\
v_n\{6\} =& \left[(1/4)\cdot\left(\langle v_n^6\rangle - 9\langle v_n^4\rangle\langle v_n^2\rangle + 12\langle v_n^2\rangle^3\right)\right]^{1/6}, \\
v_n\{8\} =& \left[-(1/33)\cdot\left(\langle v_n^8\rangle - 16\langle v_n^6\rangle\langle v_n^2\rangle - 18\langle v_n^4\rangle^2 + 144\langle v_n^4\rangle\langle v_n^2\rangle^2 - 144\langle v_n^2\rangle^4\right)\right]^{1/8}.
\end{aligned} \tag{6.9}$$

For a Gaussian distributions, in the case of small fluctuations $\sigma_{v_n} \ll \langle v_n\rangle$ (and non-flow effect are removed in 2-particle cumulant measurements as assumed),

$$\begin{aligned}
v_n\{2\}^2 =& \langle v_n\rangle^2 + \sigma_{v_n}^2, \\
v_n\{4\}^2 \approx& \langle v_n\rangle^2 - \sigma_{v_n}^2, \\
v_n\{6\}^2 \approx& \langle v_n\rangle^2 - \sigma_{v_n}^2, \\
v_n\{8\}^2 \approx& \langle v_n\rangle^2 - \sigma_{v_n}^2,
\end{aligned} \tag{6.10}$$

where $\langle v_n\rangle$ is the anisotropic flow from the participant plane and σ_{v_n} is the corresponding anisotropic flow fluctuations. These two quantities correspond to the first and second order moments of the underlying $p.d.f.$ of v_n distributions.

Figure 6.3 shows the centrality dependence of v_2 measured with 2- and multi-particle correlations by ALICE [201]. The solid blue points show the v_2 with estimated with 2-particle correlations with pseudorapidity gap $|\Delta\eta| > 1$ and non-flow removed by HIJING calculations. The measurements of multi-particle correlations are clearly lower than those from 2-particle correlations. The difference is mainly due to the contributions of elliptic flow fluctuations.

Using the measured $v_n\{2\}$ and $v_n\{4\}$, we can obtain the $\langle v_n \rangle$ and σ_{v_2} via:

$$\begin{aligned} \langle v_n \rangle &\approx \sqrt{\frac{v_n^2\{2\} + v_n^2\{4\}}{2}}, \\ \sigma_{v_n} &\approx \sqrt{\frac{v_n^2\{2\} - v_n^2\{4\}}{2}}. \end{aligned} \tag{6.11}$$

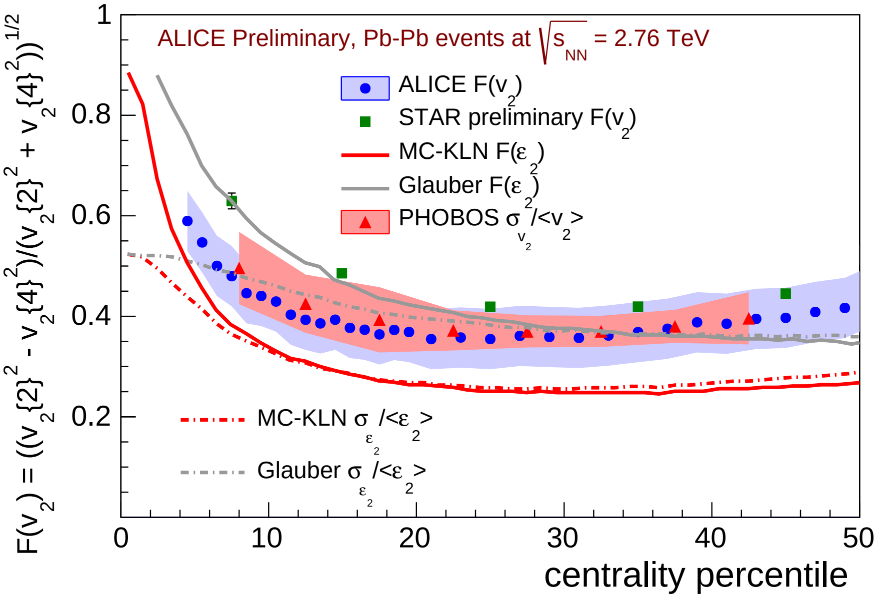

Figure 6.4: Centrality dependence of relative elliptic flow fluctuations and relative eccentricity fluctuations. The ALICE, STAR and PHOBOS $F(v_2)$ results are shown by blue circle, green square and red triangle, respectively. The solid and dash lines are for F_{ε_2} and $\sigma_\varepsilon/\langle\varepsilon_2\rangle$ from MC-Glauber (grey) and MC-KLN (red).

The centrality dependence of σ_{v_2} is presented in Fig. 6.3 (Right). The second moment of the v_2 distribution equals approximately 0.02 in the most central collisions and increases as the centrality is increasing. The σ_{v_2} estimated at LHC energies is clearly higher than the estimation at the top RHIC energy [198, 199], which could indicate that stronger elliptic flow fluctuations develop at LHC than at RHIC. Furthermore, the relative elliptic flow fluctuations $\sigma_{v_2}/\langle v_2 \rangle$ can be estimated via $F(v_2)$ defined as:

$$F(v_n) = \sqrt{\frac{v_n^2\{2\} - v_n^2\{4\}}{v_n^2\{2\} + v_n^2\{4\}}}. \tag{6.12}$$

Figure 6.4 shows the centrality dependence of $F(v_2)$ measured in ALICE. The $F(v_2)$ decreases from central to mid-central collisions, and saturates at a value of ≈ 0.4 for mid-central and mid-peripheral collisions. The $F(v_2)$ measured at top RHIC energy by the STAR, represented by the green markers in the same figure, indicates a larger value of relative elliptic flow fluctuations. This might be due to the fact that there was no non-flow subtraction for the 2-particle correlations in $F(v_2)$ calculations from STAR [199]. Thus, non-flow included $F(v_2)$ measured by STAR gave an upper limit of the relative elliptic flow fluctuations at top RHIC energy. In addition, the $\sigma_{v_2}/\langle v_2 \rangle$ from PHOBOS was measured using a completely different technique [198]. The PHOBOS results are in a good agreement with ALICE measurements. Although the elliptic flow fluctuations are stronger at LHC than top RHIC energy, the relative flow fluctuations are of similar magnitude. It is also found that $F(\varepsilon_2)$ from MC-Glauber roughly describes $F(v_2)$ measured by ALICE in the centrality range 20-50% while it overestimates $F(v_2)$ in most central collisions. Meanwhile, $F(\varepsilon_2)$ from MC-KLN underestimates $F(v_2)$ for all centrality classes. These results suggest that the MC-Glauber model simulates initial eccentricity fluctuations better than MC-KLN model. Obviously the comparisons of elliptic flow fluctuations and initial eccentricity fluctuations will provide a way to constrain the initial state models.

6.1.2 Higher order cumulants

Besides the studies of mean and standard deviation, the higher order cumulants of the v_n (and ε_n) distributions are investigated. Figure 6.1 shows the centrality dependence of higher order cumulants of ε_2 from MC-Glauber model and MC-KLN CGC model. All higher order cumulants seem to give compatible results. Interestingly enough for Bessel-Gaussian p.d.f. all higher order cumulants are exactly the same [89]. On the other hand the Elliptic-Power function predicts $\sim 1\%$ difference between 4- and 6-particle cumulant, and 0.1% difference between 6- and 8-particle cumulant. The measurements of $v_2\{4\}$, $v_2\{6\}$ and $v_2\{8\}$ are presented in Fig. 6.3. Good agreement has been observed for the multi-particle cumulants of v_2, as expected if the underlying $p.d.f.$ is Bessel-Gaussian, Power-Law as well as Elliptic-Power distributions. Unfortunately, the current statistics do not allow a precision to distinguish which function gives the best description of higher order cumulants, it seems that all three functions are still the promising candidates for the underlying $p.d.f.$.

6.1.3 Flow fluctuations of higher harmonics

To further constrain the possible candidate of the underlying $p.d.f$, we also study the moments of higher harmonics distributions, which have different sensitivities to fluctuations.

Considering the odd harmonics originate from the initial geometry fluctuations, it should satisfy the case of only fluctuations. The centrality dependence of 2- and multi-particle cumulants for triangular flow, presented in Fig. 6.6 (left), show dramatically different results of 2- and multi-particle cumulants. Then $F(v_3)$ is calculated from Eq. (6.12), using $v_3\{2\}$ and $v_3\{4\}$ shown in Fig. 6.6 (left). The result is presented in Fig. 6.6 (right). It shows that the magnitude of $F(v_3)$ ranges from 0.7 to 0.8. It is clear that the assumption $\sigma_{v_n} \ll \langle v_n \rangle$ does not hold for odd harmonics and $F(v_3)$, thus can not be used as an estimation of relative triangular flow fluctuations.

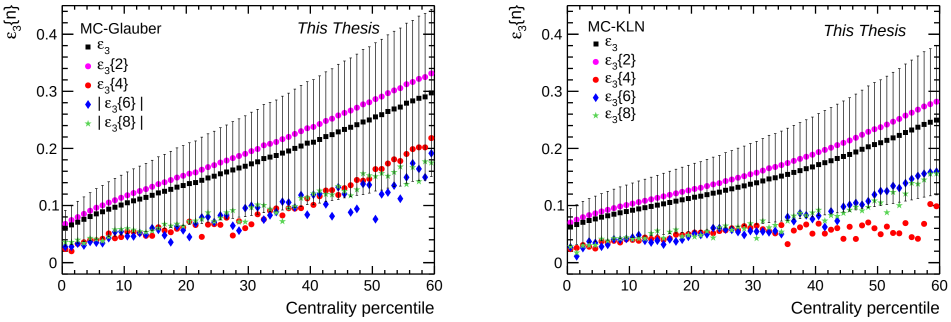

Figure 6.5: Centrality dependence of 2- and higher-order cumulant for ε_3 from both MC-Glauber model (left) and MC-KLN (CGC) model (right). The black lines are the spread of ε_n, which stand for σ_ε.

The expectations from Bessel-Gaussian fluctuations, are the following [89]:

$$\begin{aligned} \varepsilon_3\{2\} &= \frac{2}{\sqrt{\pi}}\,\langle\varepsilon_3\rangle, \\ \varepsilon_3\{4\} &= \varepsilon_3\{6\} = \varepsilon_3\{8\} = 0, \end{aligned} \tag{6.13}$$

and:

$$\begin{aligned} v_3\{2\} &= \frac{2}{\sqrt{\pi}}\,\langle v_3\rangle, \\ v_3\{4\} &= v_3\{6\} = v_3\{8\} = 0. \end{aligned} \tag{6.14}$$

The condition $\varepsilon_3\{2\}/\langle\varepsilon_3\rangle \approx 1.13$ is satisfied in both MC-Glauber and MC-KLN model. However, the higher order cumulants of both ε_3 (shown in Fig. 6.5) and v_3 (shown in Fig. 6.6) have finite magnitudes. This observation does not support the expectation from Bessel-Gaussian function [89]. On the other hand, it is in-line with expectations from Power-Law and Elliptic-Power function. In addition, Fig. 6.6 also shows that the ratio $\sigma_{\varepsilon_3}/\langle\varepsilon_3\rangle \approx 0.52 \approx \sqrt{4/\pi - 1}$ is expected by both MC-Glauber and MC-KLN model. However, it seems that $\varepsilon_3\{4\} \approx \langle\varepsilon_3\rangle - \sigma_{\varepsilon_3} \approx \langle\varepsilon_3\rangle - \sqrt{4/\pi - 1} \times \langle\varepsilon_3\rangle \approx 0.48\ \langle\varepsilon_3\rangle$ in the centrality intervals presented here. If the initial triangularity fluctuations are the only source of triangular flow fluctuations ($v_3 \propto \varepsilon_3$), we expect $\sigma_{v_3}/\langle v_3\rangle \approx \sqrt{4/\pi - 1}$ and $v_3\{4\} = \langle v_3\rangle - \sigma_{v_3}$. For non-flow corrected $v_3\{2\}$ and $v_3\{4\}$, we obtain $v_3\{4\} \approx 0.43\ v_3\{2\}$, which agrees within uncertainties with what we got in Fig. 6.6 (Left). Furthermore, the 6-particle cumulants are studied as a function of centrality[2] for v_3 in Fig. 6.6 (Left). It is found that $v_3\{6\}$ is finite and $v_3\{6\} \approx v_3\{4\}$. This observation confirms that Bessel-Gaussian fluctuations, which predicts all higher order cumulants are equal to 0, are excluded as the underlying *p.d.f.*.

---

[2] Due to limited statistics, v_3 measurements are not available with 8-particle cumulants.

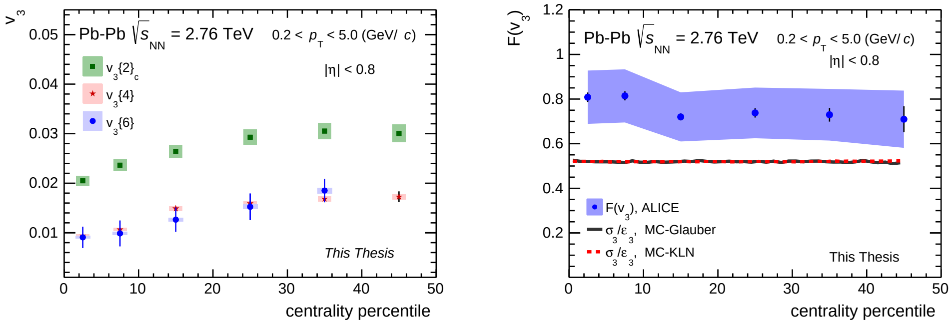

Figure 6.6: (Left) Centrality dependence of $v_3\{2\}$, $v_3\{4\}$ and $v_3\{6\}$ in centrality range 0-50%. (Right) $F(v_3)$, σ_3/ε_3 as a function of centrality.

Recent study [223] shows the predictions from Power-Law function[3] as: $v_3\{4\}/v_3\{2\} \sim 0.5$, $v_3\{6\}/v_3\{4\} \approx 0.84$ and $v_3\{8\}/v_3\{6\} \approx 0.94$ for mid-central collisions. The non-zero $v_3\{4\}$ and $v_3\{4\}/v_3\{2\} \sim 0.5$ expectations agree with the experimental measurements. Unfortunately, due to the current limited statistics, it is difficult to judge whether the Power-Law distributions or Elliptic-Power function describe better the data for higher order cumulants. Therefore, the LHC RUN2 program, which might bring a factor of 10 statistics, will be very useful for further study of the underlying $p.d.f.$, with the precise measurements of higher order cumulants.

6.1.4 Fitting the event-by-event ε_n distributions

In order to provide further constraints on the underlying $p.d.f$, one powerful approach is to study the event-by-event ε_n distributions, simulated by initial state models. Figure 6.7 shows the ε_2 distributions for the 0-5%, 30-40% and 60-70% from MC-Glauber calculations. The three distributions are fitted with Power-Law (green solid line), Bessel-Gaussian (azure dot dash line) and Elliptic-Power (red dash line) functions. It is found that in the 0-5% interval, the three functions give consistent results and all fit the ε_2 distribution quite well. In most central collisions, $\varepsilon_0 \ll 1$ and $\alpha > 1$, the Elliptic-Power distribution reduces to Bessel Gaussian distribution and to Power-Law distribution if $\varepsilon_0 = 0$ (anisotropy is solely due to fluctuations). Thus, all three functions give almost the same descriptions of ε_n distributions in most central collisions. The nice agreements between all three functions show that ε_0 must have a very small value, consistent with the idea of an eccentricity generated mainly by fluctuations. For the 30-40% centrality interval, both Bessel-Gaussian and Elliptic-Power functions describe fairly well the ε_2 distributions with the latter providing a better agreement. On the other hand, the Power-Law function doesn't work satisfactorily in this centrality range. For most peripheral collisions, the Elliptic-Power function still describes correctly the ε_2 distributions,

---

[3] The Elliptic-Power function should give very similar result with Power-Law if the extra parameter $v_3\{\mathrm{RP}\}$ goes to 0.

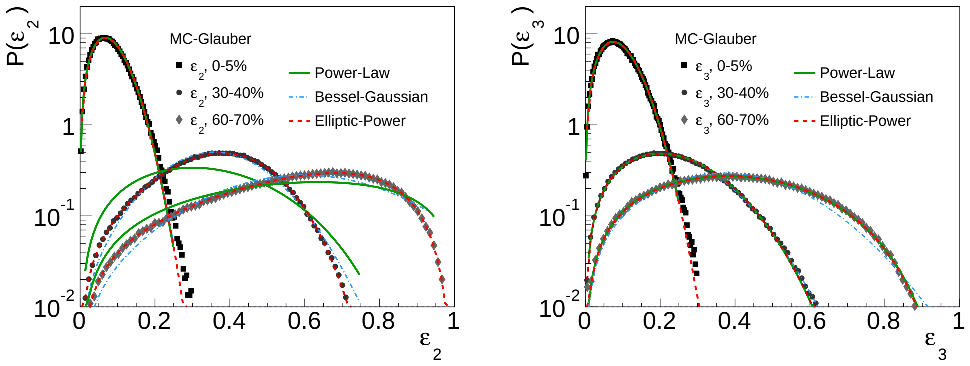

Figure 6.7: Event-by-event distributions of ε_2 (Left) and ε_3 (Right) from MC-Glauber model.

which can not be reproduced by either by Bessel-Gaussian or Power-Law function.

The ε_3 distributions are presented together with three fits in Fig. 6.7 (right). Since triangularity is solely created by geometry fluctuations, the ε_3 distributions could be well described by the single-parameter Power-Law function. The two-parameters Elliptic-Power has been tested and the parameter ε_0 turns out to be zero. This agrees with the expectation of no correlations between initial Φ_3 and reaction plane. On the other hand, the Bessel-Gaussian function quantitatively reproduces the ε_3 distributions for central and mid-central collisions but the agreement is worse for most peripheral collisions.

Combining the results of moments for the v_n and ε_n and the event-by-event distributions of ε_n, we can conclude the following:

- Bessel-Gaussian: predicts zero value of $v_3\{n\}$ and $\varepsilon_3\{n\}$ $(n \geq 4)$ [89] which are not supported by the data; in addition it seems to fail in describing the ε_2 distributions and ε_3 distributions (in peripheral collisions), due to the lack of constrains $\varepsilon_n < 1$;

- Power-Law: does not describe the ε_2 distributions (in non-central collisions), while it predicts non-zero value of $v_3\{n\}$ and $\varepsilon_3\{n\}$ $(n \geq 4)$ which agrees with the results [224]; furthermore, it predicts different values of higher order cumulants which has not been validated yet;

- Elliptic-Power: quantitatively reproduces both the ε_2 and ε_3 distributions in all centrality intervals, predicts non-zero value of $v_3\{n\}$ and $\varepsilon_3\{n\}$ $(n \geq 4)$, and predicts slightly different values of higher order cumulants [223] which has not been validated yet.

From the above, it is clearly that Elliptic-Power function is the most promising candidate of the underlying *p.d.f.* of v_n distributions. In the future, with large statistics from heavy ion collisions at the LHC, the measurements of $v_3\{4\}$, $v_3\{6\}$, $v_3\{8\}$ will be crucial to confirm if Elliptic-Power is the *p.d.f.* of v_n distributions.

The study of flow fluctuations for different harmonics broadens the knowledge of the geometry fluctuations and their effects to the final anisotropic flow measurements. However, the comparison of anisotropic flow measurements and hydrodynamic calculations are not only applied for the integrated, but also for the differential flow, which is more sensitive to the η/s and initial conditions. Additional p_{T} and/or η dependent fluctuations of symmetry plane orientation (named flow angle in [214, 215]) and magnitude might be produced as the response of the system to initial geometry fluctuations. In the following section, searches of p_{T} dependent flow angle and magnitude fluctuations, which might originate from initial geometry fluctuations, will be discussed.

6.2 Transverse momentum dependent flow angle and magnitude fluctuations

A powerful technique to characterize the properties of the medium created in heavy-ion collisions is to use two-particle azimuthal correlations expanded in a Fourier series in relative angle $\Delta\varphi$ of the particle pair:

$$\frac{d^3N^{pair}}{dp_{\mathrm{T}}^a dp_{\mathrm{T}}^t d\Delta\varphi} \propto 1 + \sum_{n=1}^{\infty} 2V_{n\Delta}(p_{\mathrm{T}}^a, p_{\mathrm{T}}^t)\cos(n\Delta\varphi), \tag{6.15}$$

where p_{T}^a and p_{T}^t are the transverse momenta of the trigger and the associate particles, respectively. The $V_{n\Delta}(p_{\mathrm{T}}^a, p_{\mathrm{T}}^t)$ is the n^{th} order Fourier harmonic of the two particle azimuthal correlations. When the only source of correlations among produced particles is anisotropic flow, all particles are correlated to some common symmetry planes, $V_{n\Delta}(p_{\mathrm{T}}^a, p_{\mathrm{T}}^t)$ is naïve expected to exhibit *factorization*:

$$V_{n\Delta}(p_{\mathrm{T}}^a, p_{\mathrm{T}}^t) = v_n(p_{\mathrm{T}}^a) \cdot v_n^{\mathrm{ref}}. \tag{6.16}$$

In order to get the single particle $v_n(p_{\mathrm{T}})$, one can use the so called 'Global Fit' to extract $v_n(p_{\mathrm{T}}^a)$ (and v_n^{ref}) directly from $V_{n\Delta}(p_{\mathrm{T}}^a, p_{\mathrm{T}}^t)$ [173]. Another approach to obtain the single particle $v_n(p_{\mathrm{T}}^a)$ is by calculating first the reference flow by selecting two reference flow particles from $p_{\mathrm{T}}^{\mathrm{ref}}$:

$$v_n(p_{\mathrm{T}}^{\mathrm{ref}}) = \sqrt{V_{n\Delta}(p_{\mathrm{T}}^{\mathrm{ref}}, p_{\mathrm{T}}^{\mathrm{ref}})}. \tag{6.17}$$

We then correlate the particle we are interested with those from $p_{\mathrm{T}}^{\mathrm{ref}}$, by measuring $V_{n\Delta}(p_{\mathrm{T}}^a, p_{\mathrm{T}}^{\mathrm{ref}})$. In the end, the $v_n(p_{\mathrm{T}}^a)$ can be obtained by:

$$v_n(p_{\mathrm{T}}^a) = \frac{V_{n\Delta}(p_{\mathrm{T}}^a, p_{\mathrm{T}}^{\mathrm{ref}})}{\sqrt{V_{n\Delta}(p_{\mathrm{T}}^{\mathrm{ref}}, p_{\mathrm{T}}^{\mathrm{ref}})}}, \tag{6.18}$$

assuming $v_n(p_{\mathrm{T}}^a)$ is independent of the selection of reference flow particles.

However, the factorization (Eq. 6.16) does not always hold true, e.g. most of known sources of non–flow correlations do not factorize at low p_{T}, which is confirmed by Monte Carlo studies [213]. On the other hand, it is expected that factorization comes naturally in a pure hydrodynamic picture where non-flow effects are negligible. Therefore, the factorization should work perfectly in hydrodynamics. In contrast, the recent hydrodynamic calculations from Gardim *et al* [214] show clearly that factorization can be broken even if these correlations are entirely driven by collective flow. Later on, Heinz *et. al.* pointed out that in general flow angles Ψ_n depend on p_T in hydrodynamic simulations [215]. The p_T dependent flow angle fluctuations, as well as the p_T dependent flow magnitude fluctuations have been discussed in [215] using VISH$2+1$ calculations. This effect was proposed as a natural reason for the factorization being broken in hydrodynamic calculations in which non-flow correlations are absent.

6.2.1 Factorization and r_n

A new observable, called factorization ratio r_n, was proposed to test the validation of factorization [214]. It is defined as:

$$r_n \equiv \frac{V_{n\Delta}(p_\mathrm{T}^a, p_\mathrm{T}^t)}{\sqrt{V_{n\Delta}(p_\mathrm{T}^a, p_\mathrm{T}^a) \cdot V_{n\Delta}(p_\mathrm{T}^t, p_\mathrm{T}^t)}}. \tag{6.19}$$

If there are p_T dependent fluctuations of flow angle and magnitude, Eq. (6.16) changes to:

$$V_{n\Delta}(p_\mathrm{T}^a, p_\mathrm{T}^t) = \langle v_n(p_\mathrm{T}^a) v_n^{\mathrm{ref}} e^{in(\Psi_n^a - \Psi_n^t)}. \rangle \tag{6.20}$$

and then:

$$r_n \equiv \frac{V_{n\Delta}(p_\mathrm{T}^a, p_\mathrm{T}^t)}{\sqrt{V_{n\Delta}(p_\mathrm{T}^a, p_\mathrm{T}^a) \cdot V_{n\Delta}(p_\mathrm{T}^t, p_\mathrm{T}^t)}} = \frac{\langle v_n(p_\mathrm{T}^a)\, v_n^{\mathrm{ref}}\, e^{in(\Psi_n^a - \Psi_n^t)} \rangle}{\sqrt{\langle v_n(p_\mathrm{T}^a)^2 \rangle \langle v_n^{\mathrm{ref}}\, v_n^{\mathrm{ref}} \rangle}}. \tag{6.21}$$

It follows that if r_n is consistent with unity, the factorization holds. Otherwise, the factorization is broken, which implies possible p_T dependent fluctuations of flow angle and magnitude.

Analysis approach to obtain $V_{n\Delta}(p_\mathrm{T}^a, p_\mathrm{T}^t)$: direct calculation method

The usual way to obtain $V_{n\Delta}(p_\mathrm{T}^a, p_\mathrm{T}^t)$ is from the 2-particle correlations function $C(\Delta\varphi, \Delta\eta)$ where $\Delta\varphi$ and $\Delta\eta$ are the differences in azimuthal angle φ and pseudorapidity η between the two particles. The $C(\Delta\varphi, \Delta\eta)$ is usually calculated via:

$$C(\Delta\varphi, \Delta\eta) = \frac{S(\Delta\varphi, \Delta\eta)}{B(\Delta\varphi, \Delta\eta)}. \tag{6.22}$$

Here the signal function $S(\Delta\varphi, \Delta\eta)$ is the per-trigger-particle yield extracted from pairs found in the same event, while the background function $B(\Delta\varphi, \Delta\eta)$ is obtained from mixed-event technique in order to remove structure in the angular distribution that arises from non–uniform acceptance (NUA) and non-uniform efficiency (NUE).

However, inspired by the Q-Cumulant method with pseudorapidity gap, $V_{n\Delta}(p_\mathrm{T}^a, p_\mathrm{T}^t)$ can be obtained as:

$$V_{n\Delta}(p_\mathrm{T}^a, p_\mathrm{T}^t) = \left\langle V_n(p_\mathrm{T}^a)\, V_n(p_\mathrm{T}^{t*}) \right\rangle = \left\langle \frac{q_n^a \cdot q_n^{t*}}{m^a m^t} \right\rangle \tag{6.23}$$

where $V_n = \langle e^{in\varphi} \rangle$ is the n^{th} order complex Fourier flow coefficient, q_n^a, q_n^t are the flow vectors built at transverse momentum p_{T}^a and p_{T}^t, m^a and m^t are the corresponding multiplies, and $\langle\ \rangle$ indicates an average over all events. We can also get:

$$V_{n\Delta}(p_{\mathrm{T}}^a, p_{\mathrm{T}}^a) = \langle V_n(p_{\mathrm{T}}^a) V_n(p_{\mathrm{T}}^{a*}) \rangle = \left\langle \frac{p_n^a \cdot p_n^{a*}}{M_a M_a} \right\rangle. \tag{6.24}$$

In this case the two particles are both selected from p_{T}^a with a pseudorapidity gap in between. Therefore, the non-flow effects are expected to be suppressed while no self-correlations are included in the two-particle correlations.

Considering the $V_{n\Delta}(p_{\mathrm{T}}^a, p_{\mathrm{T}}^t)$ can be directly calculated with the flow vector and without using correlations function $C(\Delta\varphi, \Delta\eta)$, this method is called "*direct calculation method*". For the analysis presented in this thesis, we will show the results based on "*direct calculation method*".

Searches for p_{T} dependent flow angle and magnitude fluctuations in Pb–Pb collisions via r_n measurements

In this thesis, we study the factorization ratio r_n (n = 2, 3) as a function of p_{T}^t and p_{T}^a (with different pseudorapidity gaps) in various centrality classes in Pb–Pb collisions at $\sqrt{s_{\mathrm{NN}}} = 2.76$ TeV. By construction, we have $r_n = 1$ when we select the trigger and associate particles from the same p_{T} interval ($p_{\mathrm{T}}^t = p_{\mathrm{T}}^a$).

Figure 6.8 and 6.9 show the factorization ratios r_2 and r_3, respectively, for eight p_{T}^t bins (p_{T}^t is increasing from top to bottom panels) as a function of p_{T}^a. The measurements are performed in centrality classes 0-5 %, 20-30 % and 40-50 %. Contrary to other analyses, there is no $p_{\mathrm{T}}^t \geq p_{\mathrm{T}}^a$ cut (which is applied to avoid self-correlations) applied in this thesis, due to the pseudorapidity gap between subevents. The error bars correspond to statistical uncertainties, while the shaded colour bands correspond to systematic uncertainties.

It is seen in Fig. 6.8 that r_2 significantly deviates from unity as the collisions become more central. For the 0-5 % centrality interval this effect becomes stronger the larger the difference is between p_{T}^t and p_{T}^a. The previous measurements [173] indicated that the factorization holds approximately for $n = 2$ for p_{T} below 4 GeV/c. This analysis, shows that the factorization breaks at lower p_{T}, with a more sensitive observable r_2. The deviation from unity is up to 20 % for the lowest p_{T}^a for $3 < p_{\mathrm{T}}^t < 4$ GeV/c in the 0-5% most central Pb-Pb collisions. This can be naturally explained by p_{T} dependent fluctuations of flow angle (Ψ_2) and magnitude (v_2), generated by initial event-by-event geometry fluctuations. However, since non-flow effects might not be removed completely by using a pseudorapidity gap, it is still possible that they contribute to the deviation of r_2 from unity. Figure 6.8 also shows the recent r_2 measurements from the CMS Collaboration, applying a larger pseudorapidity gap ($|\Delta\eta| > 2.0$). It is seen that the CMS measurement seems to be consistent with the ALICE results. The agreement of the r_2 measurements indicates that the possible additional pseudorapidity dependent fluctuations of flow angle (Ψ_2) and magnitude (v_2) is not supported by the data (within the uncertainties).

Figure 6.8 also presents the comparison of two hydrodynamic calculations with data for the presented centrality classes. Both hydrodynamic calculations with MC-Glauber

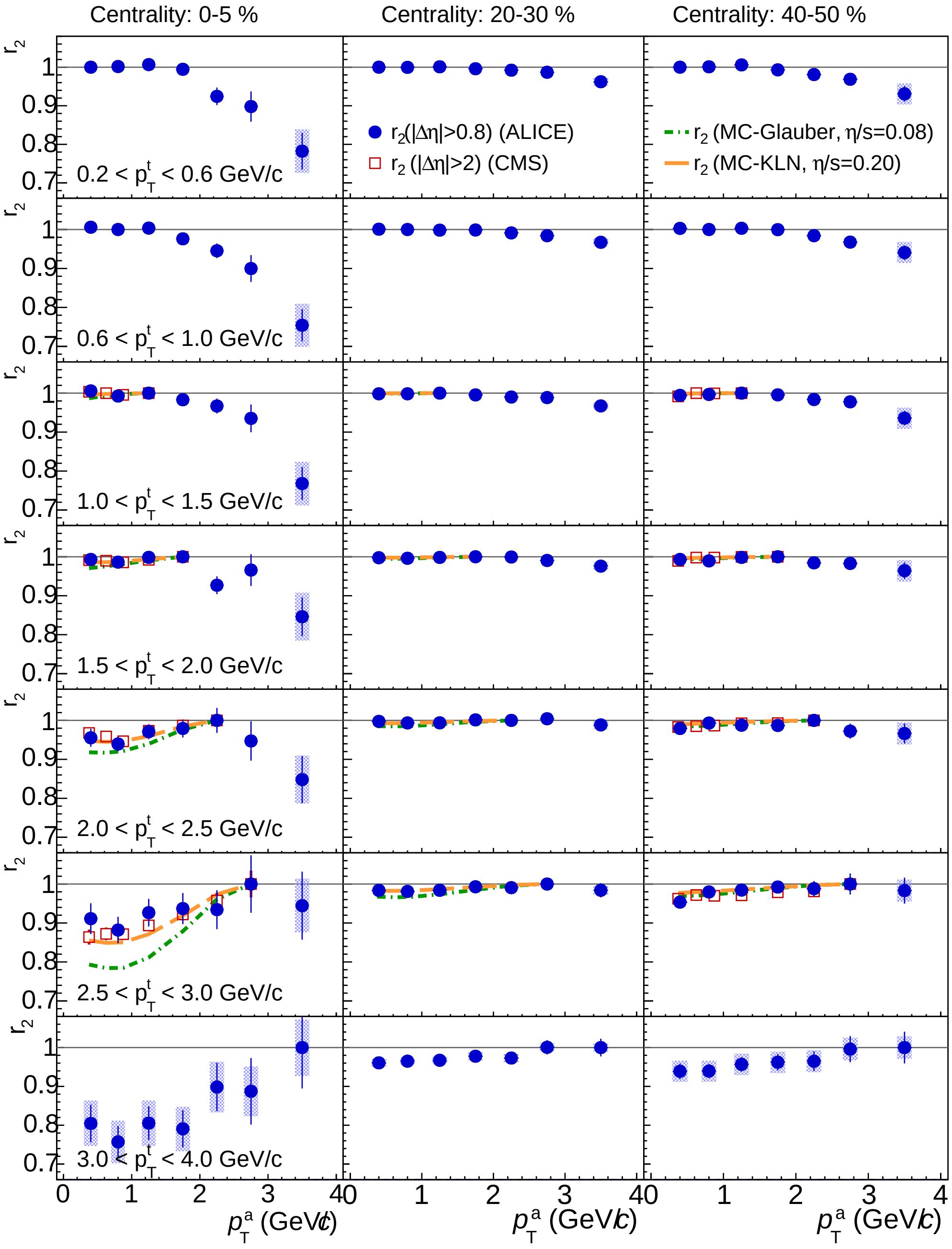

Figure 6.8: Factorization ratio r_2, as a function of p_{T}^{a} in 8 p_{T}^{t} bins for 0-5 %, 20-30 % and 40-50 % in Pb–Pb collisions at $\sqrt{s_{\mathrm{NN}}}$ = 2.76 TeV, is presented by solid circles. CMS measurements are presented by open squares. In addition, hydrodynamic calculations with MC-Glauber initial condition and η/s = 0.08 and with MC-KLN initial condition and η/s = 0.20 are shown in dot-dash green and dash orange curves.

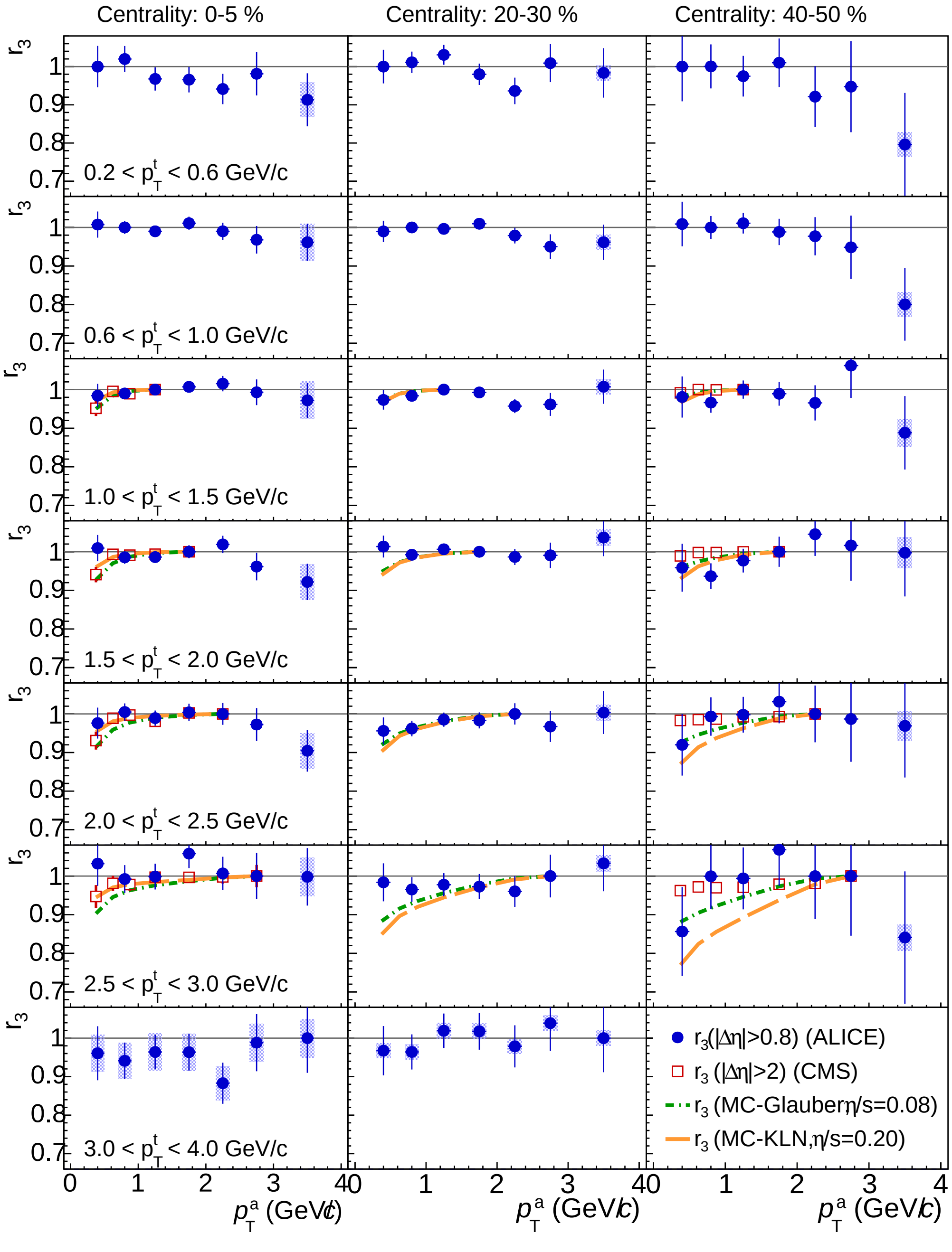

Figure 6.9: Factorization ratio r_3, as a function of p_{T}^{a} in 7 p_{T}^{t} bins for 0-5 %, 20-30 % and 40-50 % in Pb–Pb collisions at $\sqrt{s_{\mathrm{NN}}} = 2.76$ TeV, is presented by solid circles. CMS measurements are presented by open squares. In addition, hydrodynamic calculations with MC-Glauber initial condition and $\eta/s = 0.08$ and with MC-KLN initial condition and $\eta/s = 0.20$ are shown in dot-dash green and dash orange curves.

initial condition and $\eta/s = 0.08$ and MC-KLN initial condition and $\eta/s = 0.20$ qualitatively predict the trend of r_2, while the latter one agrees with the data better.

For r_3, the factorization is valid over a wider range of p_{T}^a, p_{T}^t and centrality, when compared to r_2. The factorization is broken within 10 % when p_{T}^a, p_{T}^t are below 4 GeV/c. Again, CMS measurements quantitatively agree with the ALICE r_3 results although the pseudorapidity ranges are different between the two analyses. This suggests that the additional pseudorapidity dependent fluctuations of flow angle (Ψ_3) and magnitude (v_3) are not observed in presented analysis.

6.2.2 $v_n\{2\}$ *vs.* $v_n[2]$ measurements

Another way used to probe the p_{T} dependent flow angle and magnitude fluctuations is via the v_n measurements. Typically the anisotropic flow coefficients at p_{T}^a can be evaluated as:

$$\begin{aligned} v_n\{2\}(p_{\mathrm{T}}^a) &= \frac{\langle \cos\, n(\varphi_1^a - \varphi_2^{\mathrm{ref}})\rangle}{\langle \cos\, n(\varphi_1^{\mathrm{ref}} - \varphi_2^{\mathrm{ref}})\rangle^{1/2}} \\ &= \frac{\langle \cos\,[n(\varphi_1^a - \Psi_n) - n(\varphi_2^{\mathrm{ref}} - \Psi_n)]\rangle}{\langle \cos\,[n(\varphi_1^{\mathrm{ref}} - \Psi_n) - n(\varphi_2^{\mathrm{ref}} - \Psi_n)]\rangle^{1/2}} = \frac{\langle v_n(p_{\mathrm{T}}^a)\, v_n^{\mathrm{ref}}\rangle}{\langle v_n^{\mathrm{ref}}\, v_n^{\mathrm{ref}}\rangle^{1/2}}. \end{aligned} \tag{6.25}$$

Here Ψ_n is the n^{th} order participant plane and v_n^{ref} is the reference flow (usually calculated from a wide p_{T} range). One can measure $v_n(p_{\mathrm{T}}^a)$ using two-particle cumulant without using information of Ψ_n.

However, due to the predicted p_{T} dependent flow angle and magnitude fluctuations [215], Ψ_n at different transverse momentum intervals is not necessary the same. Thus, Eq. (6.25) is converted to:

$$\begin{aligned} v_n\{2\}(p_{\mathrm{T}}^a) &= \frac{\langle \cos\, n(\varphi_1^a - \varphi_2^{\mathrm{ref}})\rangle}{\langle \cos\, n(\varphi_1^{\mathrm{ref}} - \varphi_2^{\mathrm{ref}})\rangle^{1/2}} \\ &= \frac{\langle \cos\,[n(\varphi_1^a - \Psi_n^a) - n(\varphi_2^{\mathrm{ref}} - \Psi_n^{\mathrm{ref}}) + n(\Psi_n^a - \Psi_n^{\mathrm{ref}})]\rangle}{\langle \cos\,[n(\varphi_1^{\mathrm{ref}} - \Psi_n^{\mathrm{ref}}) - n(\varphi_2^{\mathrm{ref}} - \Psi_n^{\mathrm{ref}})]\rangle^{1/2}} \\ &= \frac{\langle v_n(p_{\mathrm{T}}^a)\, v_n^{\mathrm{ref}} \cos[n(\Psi_n^a - \Psi_n^{\mathrm{ref}})]\rangle}{\langle v_n^{\mathrm{ref}}\, v_n^{\mathrm{ref}}\rangle^{1/2}}. \end{aligned} \tag{6.26}$$

Comparing Eq. (6.26) to Eq. (6.25), the additional cosine term shows the difference of $\Psi_n(p_{\mathrm{T}}^a)$ *w.r.t* the event-average flow angle Ψ_n^{ref}, which can probe the possible p_{T} dependent flow angle fluctuations. Additionally, the $\langle v_n(p_{\mathrm{T}}^a)\, v_n^{\mathrm{ref}}\rangle$ can not be factorized to the product of single particle $\langle v_n(p_{\mathrm{T}}^a) v_n(p_{\mathrm{T}}^a)\rangle^{1/2}$ (or $v_n(p_{\mathrm{T}}^a)\{2\}$) and $\langle v_n^{\mathrm{ref}} v_n^{\mathrm{ref}}\rangle^{1/2}$ (or $v_n^{\mathrm{ref}}\{2\}$), if there is p_{T} dependent flow magnitude fluctuations.

A new observable, denoted as $v_n[2]$, is proposed by Heinz *et al* [215], which can be calculated via:

$$\begin{aligned} v_n[2](p_{\mathrm{T}}^a) =& \langle \cos[n(\varphi_1^a - \varphi_2^a)]\rangle^{1/2} \\ =& \langle \cos[n(\varphi_1^a - \Psi_n^a) - n(\varphi_2^a - \Psi_n^a)]\rangle^{1/2} = \langle v_n(p_{\mathrm{T}}^a)^2\rangle^{1/2}. \end{aligned} \tag{6.27}$$

The difference between $v_n\{2\}$ and $v_n[2]$ is that the former is taking the RPs from the entire p_{T} range and the POIs from the p_{T}^a, while the latter is taking both RPs and POIs from p_{T}^a range. Fruitful information is extracted from the ratio of $v_2\{2\}$ and $v_2[2]$:

$$\frac{v_n\{2\}}{v_n[2]} = \frac{\langle v_n(p_{\mathrm{T}}^a)\, v_n^{\mathrm{ref}}\, \cos[n(\Psi_n^a - \Psi_n^{\mathrm{ref}})]\rangle}{\langle v_n(p_{\mathrm{T}}^a)\, v_n(p_{\mathrm{T}}^a)\rangle^{1/2}\, \langle v_n^{\mathrm{ref}}\, v_n^{\mathrm{ref}}\rangle^{1/2}}. \tag{6.28}$$

If it is less than 1, it suggests that there might be effects of p_{T} dependent fluctuations of flow angle and magnitude.

Q-Cumulant for $v_n\{2\}$ and $v_n[2]$

Similarly to $v_2\{2\}$, $v_2[2]$ could be also evaluated using Q-Cumulant method. In the case there is no pseudorapidity gap between the two correlated particles, we have:

$$\langle 2\rangle_{[2]} = \frac{|q_n|^2 - m_q}{m_q^2 - m_q} \tag{6.29}$$

The q_n and m_q are the flow vector and multiplicity at certain p_{T} interval.

Then the event average two-particle azimuthal correlations can be calculated by inserting Eq. (6.29) into Eq. (4.28),

$$c_n[2] = \langle\langle 2\rangle\rangle_{[2]} = \frac{\sum_i (W_{\langle 2\rangle_{[2]}})_i \cdot (\langle 2\rangle_{[2]})_i}{\sum_i (W_{\langle 2\rangle_{[2]}})_i}, \tag{6.30}$$

using $(m_q^2 - m_q)$ as weight. Considering the reference flow is the same as differential flow for $v_2[2]$, we have:

$$v_n[2] = \sqrt{c_n[2]}. \tag{6.31}$$

In the case a pseudorapidity gap is applied, Eq. (6.29) is converted to:

$$\langle 2\rangle_{[2,|\Delta\eta|]} = \frac{q_{n,A} \cdot q_{n,B}^*}{m_{q,A} m_{q,B}}. \tag{6.32}$$

where A and B denote subevent A dnd B from different pseudorapidity ranges. Then the event-averaged two-particle correlations will be obtained via:

$$c_n[2, |\Delta\eta|] = \langle\langle 2\rangle\rangle_{[2,|\Delta\eta|]} = \frac{\sum_{events} (W_{\langle 2\rangle_{[2,|\Delta\eta|]}})_i \cdot (\langle 2\rangle_{[2,|\Delta\eta|]})_i}{\sum_{events} (W_{\langle 2\rangle_{[2,|\Delta\eta|]}})_i}, \tag{6.33}$$

where $W_{\langle 2\rangle_{[2,|\Delta\eta|]}} = m_{q,A} \cdot m_{q,B}$. In the end, the newly proposed differential flow from two-particle cumulant with pseudorapidity gap, called $v_2[2, |\Delta\eta|]$, is given by:

$$v_n[2, |\Delta\eta|] = \sqrt{c_n[2, |\Delta\eta|]}. \tag{6.34}$$

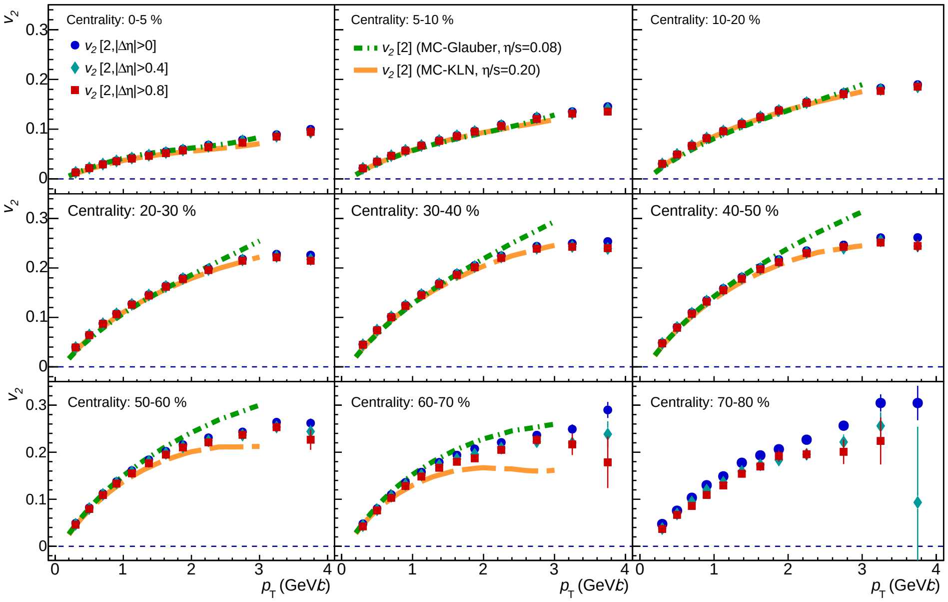

Figure 6.10: The $v_2[2]$ with $|\Delta\eta| > 0$ (solid circle), $|\Delta\eta| > 0.4$ (solid diamond) and $|\Delta\eta| > 0.8$ (solid square) for various centrality classes in Pb–Pb collisions at $\sqrt{s_{\mathrm{NN}}} = 2.76$ TeV. Hydrodynamic calculations with MC-Glauber initial condition and $\eta/s = 0.08$ and with MC-KLN initial condition and $\eta/s = 0.20$ are shown in dot-dash green and dash orange curves.

Searches for p_{T} dependent flow angle and magnitude fluctuations in Pb–Pb collisions via $v_n\{2\}$ and $v_n[2]$

Figure 6.10 shows the transverse momentum dependence of $v_2[2]$. To better understand the influence of non-flow effects to the $v_2[2]$ measurements, pseudorapidity gap $|\Delta\eta| > 0$, 0.4 and 0.8 have been tested. The $v_2[2]$ exhibits a decreasing trend as the pseudorapidity gap increases and saturates with $|\Delta\eta| > 0.8$. The non-flow effects, especially the short range correlations, are expected to be strongly suppressed when using $|\Delta\eta| > 0.8$. The results are also compared with the hydrodynamic calculations with MC-Glauber initial condition with $\eta/s = 0.08$ (which was found as the lowest possible value of η/s from a string theory model) and MC-KLN (CGC) initial condition with $\eta/s = 0.20$. It is seen that the hydrodynamic calculations with MC-KLN (CGC) initial condition and $\eta/s = 0.20$ describe the $v_2[2]$ measurement better in central and mid-central collisions while the one with MC-Glauber initial condition and $\eta/s = 0.08$ is more close to $v_2[2]$ without pseudorapidity gap.

In order to probe the p_{T} dependent flow angle and magnitude fluctuations quantitatively, the ratio $\frac{v_2\{2,|\Delta\eta|>0.8\}}{v_2[2,|\Delta\eta|>0.8]}$ is presented as a function of p_{T} in different centrality classes in Fig. 6.11. This ratio is consistent with unity up to $p_{\mathrm{T}} \sim 2$ GeV/c in the most central collision and up to $p_{\mathrm{T}} \sim 2.5$ - 3 GeV/c in non-central collisions. The devia-

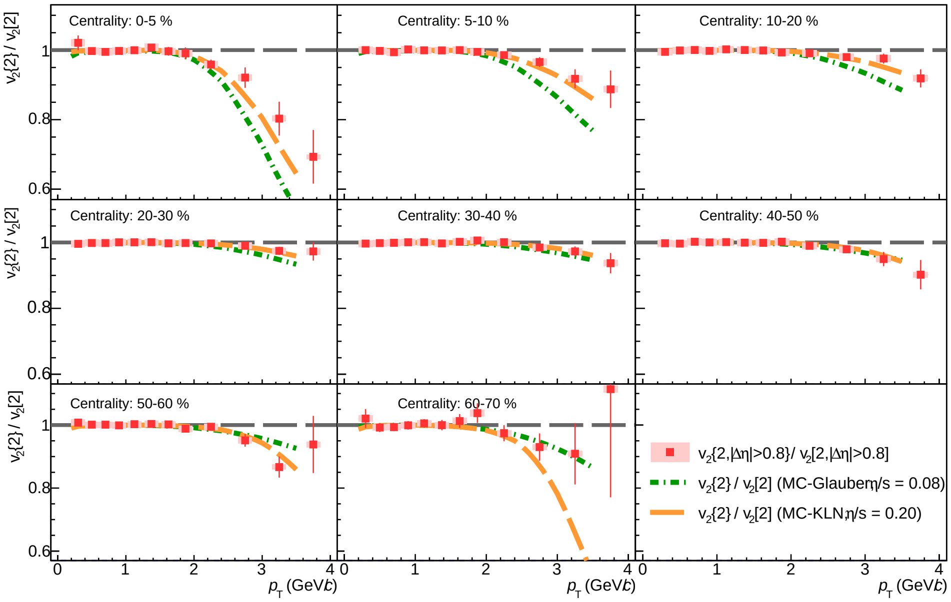

Figure 6.11: The ratio $\frac{v_2\{2,|\Delta\eta|>0.8\}}{v_2[2,|\Delta\eta|>0.8]}$ for various centralities of Pb–Pb collisions at $\sqrt{s_{\rm NN}}$ = 2.76 TeV. Hydrodynamic calculations with MC-Glauber initial condition and $\eta/s = 0.08$ and with MC-KLN initial condition and $\eta/s = 0.20$ are shown in dash green and dash orange curves.

tions from unity become weaker but occur at higher $p_{\rm T}$ range for peripheral collisions. These results indicate the $p_{\rm T}$ dependent flow angle (Ψ_2) and magnitude (v_2) fluctuations, if they exist, are limited within 10 % in non-central collisions while being more pronounced in most central collisions at the presented $p_{\rm T}$ range. The comparison to two hydrodynamic calculations shows that our data favor the descriptions of hydrodynamic calculations with MC-KLN (CGC) initial condition and $\eta/s = 0.20$ over MC-Glauber initial condition and $\eta/s = 0.08$. This indicates that the former calculation might not only generate correct v_2, but also the possible $p_{\rm T}$ dependent fluctuations of flow angle (Ψ_2) and magnitude (v_2).

In Fig. 6.12, the transverse momentum dependence of $v_3[2]$ with four different pseudorapidity gaps is shown for several centrality classes. Similar to v_2, $v_3[2]$ shows a decreasing trend as the pseudorapidity gap increases, as expected if non-flow effects are suppressed. A weak centrality dependence of $v_3[2]$ is observed after applying $|\Delta\eta| > 0.8$. When the experimental results are compared with hydrodynamic calculations, it is seen that neither calculations with initial condition from MC-Glauber nor from MC-KLN (CGC) are able to describe the measured trend.

The ratio of $\frac{v_3\{2,|\Delta\eta|>0.8\}}{v_3[2,|\Delta\eta|>0.8]}$ together with various hydrodynamic calculations are shown in Fig. 6.13 as a function of $p_{\rm T}$. It is found that the ratio $\frac{v_3\{2,|\Delta\eta|>0.8\}}{v_3[2,|\Delta\eta|>0.8]}$ agrees with unity over wider $p_{\rm T}$ range than $\frac{v_2\{2,|\Delta\eta|>0.8\}}{v_2[2,|\Delta\eta|>0.8]}$. In particular the data points do not deviate

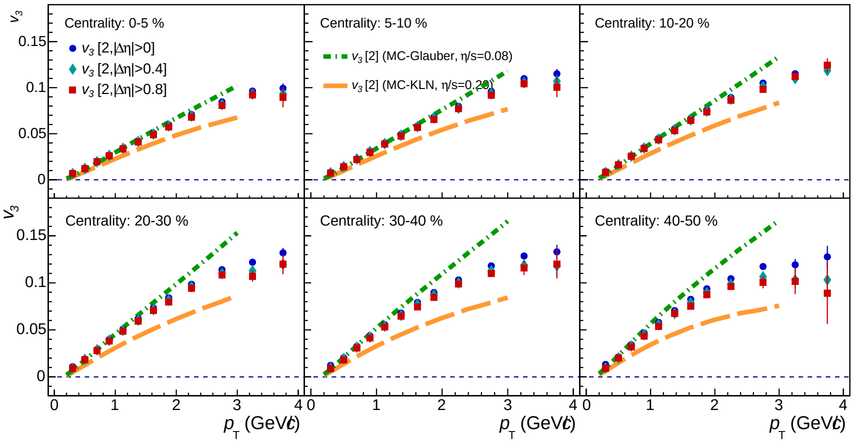

Figure 6.12: The $v_3[2]$ with different $|\Delta\eta|$ gap are presented for various centrality classes in Pb–Pb collisions at $\sqrt{s_{\rm NN}} = 2.76$ TeV. The $v_3[2, |\Delta\eta| > 0]$, $v_3[2, |\Delta\eta| > 0.4]$ and $v_3[2, |\Delta\eta| > 0.8]$ are represented by solid circle, solid diamond and solid circle, respectively. Hydrodynamic calculations with MC-Glauber initial condition and $\eta/s = 0.08$ and with MC-KLN initial condition and $\eta/s = 0.20$ are shown in dash green and dash orange curves.

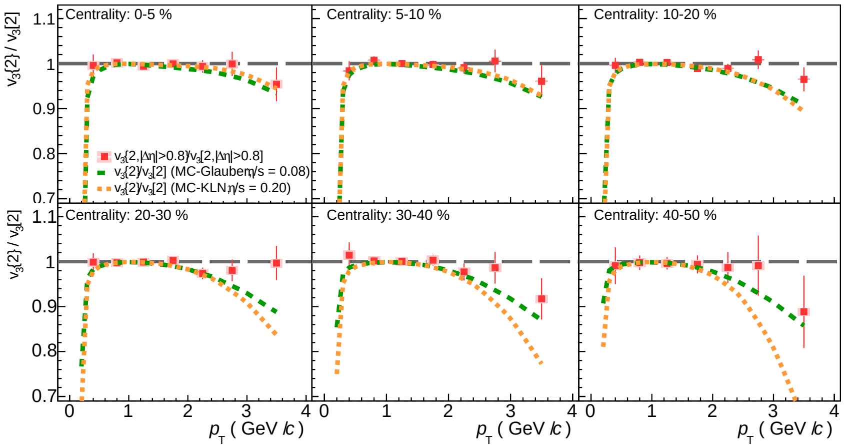

Figure 6.13: The ratio $\frac{v_3\{2,|\Delta\eta|>0.8\}}{v_3[2,|\Delta\eta|>0.8]}$ for various centralities of Pb–Pb collisions at $\sqrt{s_{\rm NN}} = 2.76$ TeV. Hydrodynamic calculations with MC-Glauber initial condition and $\eta/s = 0.08$ and with MC-KLN initial condition and $\eta/s = 0.20$ are shown in dash green and dash orange curves.

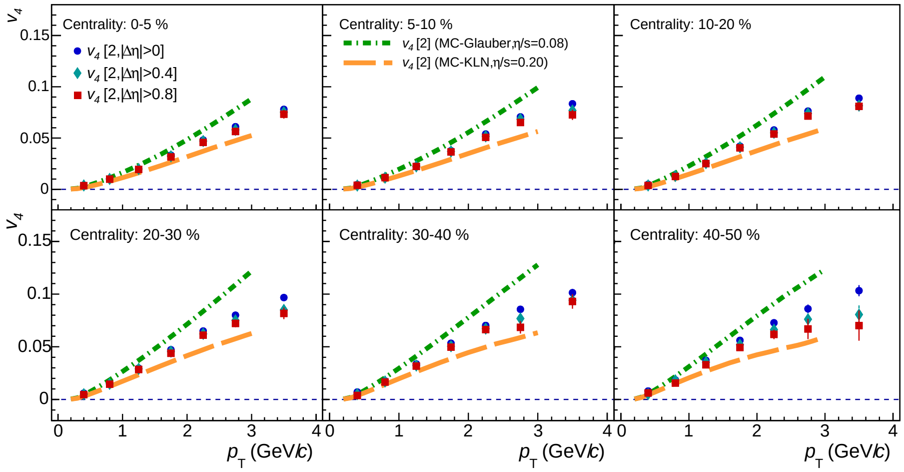

Figure 6.14: The $v_4[2]$ with different $|\Delta\eta|$ gap are presented for various centrality classes in Pb–Pb collisions at $\sqrt{s_{\rm NN}} = 2.76$ TeV. The $v_4[2, |\Delta\eta| > 0]$, $v_4[2, |\Delta\eta| > 0.4]$ and $v_4[2, |\Delta\eta| > 0.8]$ are represented by solid circle, solid diamond and solid circle, respectively. Hydrodynamic calculations with MC-Glauber initial condition and $\eta/s = 0.08$ and with MC-KLN initial condition and $\eta/s = 0.20$ are shown in dash green and dash orange curves.

within uncertainties from unity for $p_{\rm T} < 3$ GeV/c. Even though the hydrodynamic calculations with MC-Glauber and MC-KLN (CGC) initial conditions can't reproduce the magnitude of $v_3\{2\}$ and $v_3[2]$, it is still interesting to check if they can generate correct $p_{\rm T}$ dependent fluctuations of flow angle (Ψ_3) and magnitude (v_3), which are independent of the magnitude of v_3 itself. Very rough agreement is observed in Fig. 6.13 between data and hydrodynamic calculations while it is still difficult to conclude which hydrodynamic calculation describes the measurements better, due to limited statistics.

The transverse momentum dependence of $v_4[2]$ with four different pseudorapidity gaps is shown in Fig. 6.14 for different centrality intervals. Decreasing trend with increasing $|\Delta\eta|$ gap and a weak centrality dependence are observed. The hydrodynamic calculations with MC-Glauber initial condition and $\eta/s = 0.08$ (or MC-KLN (CGC) initial condition and $\eta/s = 0.20$) overestimate (underestimate) $v_4[2]$. Moreover, the ratio $\frac{v_4\{2,|\Delta\eta|>0.8\}}{v_4[2,|\Delta\eta|>0.8]}$ shown in Fig. 6.15 is in agreement within uncertainties with unity over the presented $p_{\rm T}$ range and centrality classes. This can be translated into the conclusion that no clear indication of flow angle (Ψ_4) and magnitude (v_4) is achieved so far.

In summary, hydrodynamic calculations from MC-Glauber initial condition and $\eta/s = 0.08$ and MC-KLN initial condition and $\eta/s = 0.20$ quantitatively reproduce the $v_2\{2\}$ and $v_2[2]$ results, especially at low $p_{\rm T}$, but fail to reproduce the magnitude of higher harmonic $v_n\{2\}$ and $v_n[2]$ ($n = 3$, 4). Conversely, hydrodynamic calculations with IP-Glasma initial condition and $\eta/s = 0.20$ quantitatively describe not only $v_2\{2\}$ but also $v_3\{2\}$ and $v_4\{2\}$, as discussed in Section 5.1 and 5.2. In the future, it would be interesting to see the hydrodynamic calculation of $v_n[2]$ from IP-Glasma initial condition

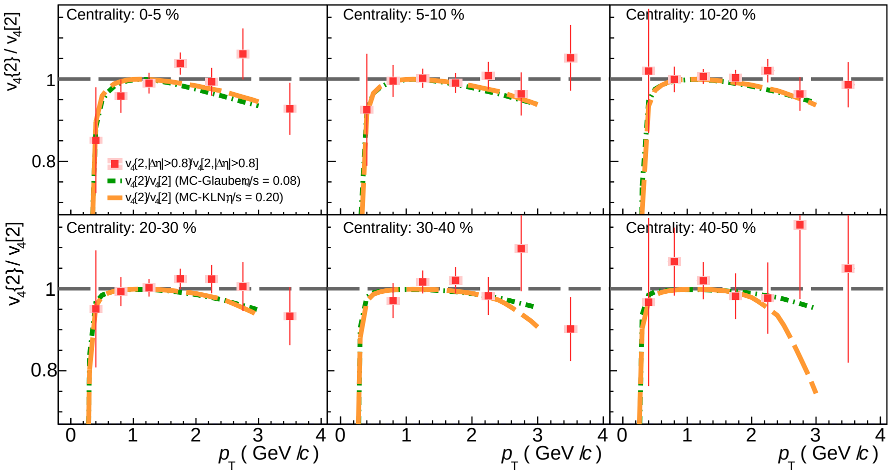

Figure 6.15: The ratio $\frac{v_4\{2,|\Delta\eta|>0.8\}}{v_4[2,|\Delta\eta|>0.8]}$ for various centralities of Pb–Pb collisions at $\sqrt{s_{\rm NN}} =$ 2.76 TeV. Hydrodynamic calculations with MC-Glauber initial condition and $\eta/s = 0.08$ and with MC-KLN initial condition and $\eta/s = 0.20$ are shown in dash green and dash orange curves.

and $\eta/s = 0.20$, with which we can further constrain the hydrodynamic model via the calculations of $p_{\rm T}$ dependent flow angle (Ψ_n) and magnitude (v_n) fluctuations.

6.2.3 Searches for $p_{\rm T}$ dependent flow angle and magnitude fluctuations in p–Pb collisions

The study of p–Pb collisions at LHC, was expected to provide baseline measurements for the quantification of cold nuclear matter effects. However, a lot of unexpected results have been observed, for instance a symmetric double ridge structure on both near- and away-side in high multiplicity p–Pb collisions as reported by ALICE [216]. In addition, the CMS Collaboration shows agreement between multi-particle cumulants, $v_2\{4\} \approx v_2\{6\} \approx v_2\{8\} \approx v_2\{\text{LYZ}\}$ [217], and similar results have been confirmed by the ATLAS Collaboration [218]. Whether the current measurements in p–Pb events, especially in the high multiplicity region, reveal the onset of collective behavior, or should be understood as non-flow effects, is a key question in p–Pb collisions [219]. Furthermore, it would be interesting to ask if collective flow develops in p–Pb collisions, and is there any addition $p_{\rm T}$ dependent flow angle and magnitude fluctuations in p–Pb collisions.

Figure 6.16 shows the $r_2(|\Delta\eta| > 0.8)$ measurements as a function of $p_{\rm T}^a$ in three $p_{\rm T}^t$ intervals for multiplicity classes 0-20 %, 20-40 % and 40-60 % in p–Pb collisions at $\sqrt{s_{\rm NN}} = 5.02$ TeV. It is found that $r_2(|\Delta\eta| > 0.8)$ deviates from unity either if we select trigger particle from $0.2 < p_{\rm T}^t < 0.6$ GeV/c and associate particle from $p_{\rm T}^a > 1$ GeV/c in all multiplicity classes; or if we select the trigger particle from $1.5 < p_{\rm T}^t < 2.0$ GeV/c and select the associate particle from very low and/or very high $p_{\rm T}$. The breakdown of factorization is more pronounced in p–Pb collisions than in peripheral Pb–Pb collisions, whose multiplicities are similar to central p–Pb collisions.

The $v_2\{2\}$, $v_2[2]$, $v_2\{2, |\Delta\eta| > 0.8\}$ and $v_2[2, |\Delta\eta| > 0.8]$ are presented in Fig. 6.17 for various multiplicity classes in p–Pb collisions at $\sqrt{s_{\rm NN}} = 5.02$ TeV. It shows that after applying a pseudorapidity gap $|\Delta\eta| > 0.8$, non-flow effects are strongly suppressed in $v_2\{2, |\Delta\eta| > 0.8\}$ and $v_2[2, |\Delta\eta| > 0.8]$. It is also found that the deviation of $v_2\{2\}/v_2[2]$ from unity appears at $p_{\rm T} \sim 3$ GeV/c, while $v_2\{2, |\Delta\eta| > 0.8\}$ and $v_2[2, |\Delta\eta| > 0.8]$ agree with each other up to $p_{rmT} \ \sim 4$ GeV/c. However, at higher $p_{\rm T}$ range, we see clearly the difference of $v_2\{2, |\Delta\eta| > 0.8\}$ and $v_2[2, |\Delta\eta| > 0.8]$. The hydrodynamic calculations from MUSIC v2.0 using modified MC-Glauber initial state and $\eta/s = 0.08$ are also presented in Fig. **??**. These calculations agree with the data better in central than in peripheral p–Pb collisions, where the non-flow effects might be dominant.

Besides v_2, the $v_3\{2, |\Delta\eta| > 0\}$, $v_3[2, |\Delta\eta| > 0]$, $v_3\{2, |\Delta\eta| > 0.8\}$ and $v_3[2, |\Delta\eta| > 0.8]$ are also investigated in p–Pb collisions at $\sqrt{s_{\rm NN}} = 5.02$ TeV. It is observed in Fig. 6.19 that not only $v_3\{2, |\Delta\eta| > 0\}$ and $v_3[2, |\Delta\eta| > 0]$ but also the difference of the two increases linearly as a function of $p_{\rm T}$. It is important to understand whether the increasing differences are due to increasing of non-flow effects or possible $p_{\rm T}$ dependent flow angle and/or magnitude fluctuations. By applying a pseudorapidity gap $|\Delta\eta| > 0.8$, the $v_3\{2, |\Delta\eta| > 0.8\}$ and $v_3[2, |\Delta\eta| > 0.8]$ are found to be much smaller than those without pseudorapidity gap. Non-flow effects seem stronger in v_3 measurements than v_2. In addition, the difference between $v_3\{2, |\Delta\eta| > 0.8\}$ and $v_3[2, |\Delta\eta| > 0.8]$ is not accessible for the presented $p_{\rm T}$ range. Based on the previous observations, there is no indication of $p_{\rm T}$ dependent flow fluctuations of angle (Ψ_3) and magnitude (v_3).

6.2.4 Outlook

The above results show the searches of $p_{\rm T}$ dependent flow angle and magnitude fluctuations, via two particle correlations techniques. However, as mentioned, there are two main issues with the 2-particle correlations:

- one can't exclude the possibility that the observed deviations of $v_2\{2\}/v_2[2]$ and r_2 from unity are due to non-flow effects;
- one can't distinguish $p_{\rm T}$ dependent flow angle fluctuations from $p_{\rm T}$ dependent flow magnitude fluctuations.

For the possible non-flow effects in two particle correlations, even if a large pseudorapidity gap between two correlated particles is applied, contributions from e.g. away-side jet contributions are not excluded. Therefore, we should either estimate the remaining non-flow effects in 2-particle correlations or use multi-particle correlations which are less sensitive to non-flow effects. In this thesis, we focus on multi-particle correlations, and new observables will be proposed later to probe the $p_{\rm T}$ dependent flow angle fluctuations and flow magnitude fluctuations separately.

New observable $v_n\{4\}/v_n[4]$: $(a, T, T, T) \xrightarrow{factorize} (a)$ & (T, T, T)

There is no theoretical implementation of such multi-particles correlations which can probe the $p_{\rm T}$ dependent flow angle and magnitude fluctuations so far. But inspired by the comparison of $v_n\{2\}$ and $v_n[2]$, we can simply construct $v_n[4]$ which select all 4-particles from the same $p_{\rm T}$ interval and compare the results to $v_n\{4\}$. If there is $p_{\rm T}$ dependent flow angle and magnitude fluctuations, we have:

$$\begin{aligned}
v_n\{4\} &= \frac{\langle \cos\, n(\varphi_1^a + \varphi_2^{\rm ref} - \varphi_3^{\rm ref} - \varphi_4^{\rm ref}) \rangle}{\langle \cos\, n(\varphi_1^{\rm ref} + \varphi_2^{\rm ref} - \varphi_3^{\rm ref} - \varphi_4^{\rm ref}) \rangle^{3/4}} \\
&= \frac{\langle \cos\,[n(\varphi_1^a - \Psi_n^a) + n(\varphi_2^{\rm ref} - \Psi_n^{\rm ref}) - n(\varphi_3^{\rm ref} - \Psi_n^{\rm ref}) - n(\varphi_4^{\rm ref} - \Psi_n^{\rm ref}) + n(\Psi_n^a - \Psi_n^{\rm ref})] \rangle}{\langle \cos\,[n(\varphi_1^{\rm ref} - \Psi_n^{\rm ref}) + n(\varphi_2^{\rm ref} - \Psi_n^{\rm ref}) - n(\varphi_3^{\rm ref} - \Psi_n^{\rm ref}) - n(\varphi_4^{\rm ref} - \Psi_n^{\rm ref})] \rangle^{3/4}} \\
&= \frac{\langle v_n(p_{\rm T}^a)\, {v_n^{\rm ref}}^3 \cos[n(\Psi_n^a - \Psi_n^{\rm ref})] \rangle}{\langle {v_n^{\rm ref}}^4 \rangle^{3/4}},
\end{aligned} \tag{6.35}$$

and

$$\begin{aligned}
v_n[4] &= \langle \cos\, n(\varphi_1^a + \varphi_2^a - \varphi_3^a - \varphi_4^a) \rangle^{1/4} \\
&= \langle \cos\,[n(\varphi_1^a - \Psi_n^a) + n(\varphi_2^a - \Psi_n^a) - n(\varphi_3^a - \Psi_n^a) - n(\varphi_4^a - \Psi_n^a)] \rangle^{1/4} \\
&= \langle v_n(p_{\rm T}^a)^4 \rangle^{1/4}.
\end{aligned} \tag{6.36}$$

Therefore, if we calculate the ratio of $v_n\{4\}$ and $v_n[4]$, we have:

$$\frac{v_n\{4\}}{v_n[4]} = \frac{\langle v_n(p_{\rm T}^a)\, {v_n^{\rm ref}}^3 \cos[n(\Psi_n^a - \Psi_n^T)] \rangle}{\langle {v_n^{\rm ref}}^4 \rangle^{3/4} \langle v_n(p_{\rm T}^a)^4 \rangle^{1/4}}. \tag{6.37}$$

Clearly if $\langle \cos[n(\Psi_n^a - \Psi_n^T)] \rangle < 1$, this signals the $p_{\rm T}$ dependent flow angle fluctuations, and if $\langle v_n(p_{\rm T}^a) {v_n^{\rm ref}}^3 \rangle < \langle {v_n^{\rm ref}}^4 \rangle^{3/4} \langle v_n(p_{\rm T}^a)^4 \rangle^{1/4}$, it suggests $p_{\rm T}$ dependent flow magnitude fluctuations. Thus, the observable $v_n\{4\}/v_n[4]$ could be used to probe $p_{\rm T}$ dependent flow angle and magnitude fluctuations, with negligible non-flow contributions.

Figure 6.20 shows the first look of the comparison between $v_2\{4\}$ and $v_2[4]$ in centrality 30-40% (Left) and 50-60% (Right). It seems that $v_2\{4\}$ agrees with $v_2[4]$ within statistical uncertainty up to $p_{\rm T} < 4$ GeV/c, where a deviation of $v_2\{2\}$ and $v_2[2]$ is observed in this $p_{\rm T}$ region as presented in Fig 6.11. However, more investigations are necessary to better understand the bias due to different kinematic selections we used in $v_2[4]$ and $v_2\{4\}$. More specifically, $v_2\{4\}$ requires at least four particles for each event and no less than three particles in each $p_{\rm T}$ interval, whereas $v_2[4]$ demands four particles for each $p_{\rm T}$ bin, following the standard definition of $v_n\{4\}$ and $v_n[4]$.

New Observable R_n: $(a,b,b,b) \xrightarrow{factorize} (a)$ & (b,b,b)

Analogously to the observable r_n, we can design R_n with 4-particle correlations. It could be defined as:

$$R_n \equiv \frac{V_n(p_\mathrm{T}^a, p_\mathrm{T}^b, p_\mathrm{T}^b, p_\mathrm{T}^b)}{V_n(p_\mathrm{T}^a, p_\mathrm{T}^a, p_\mathrm{T}^a, p_\mathrm{T}^a)^{1/4} V_n(p_\mathrm{T}^b, p_\mathrm{T}^b, p_\mathrm{T}^b, p_\mathrm{T}^b)^{3/4}} = \frac{\langle v_n(p_\mathrm{T}^a) {v_n^b}^3 \cos\left[n(\Psi_n^a - \Psi_n^b)\right]\rangle}{\langle v_n(p_\mathrm{T}^a)^4\rangle^{1/4} \langle {v_n^b}^4\rangle^{3/4}}, \tag{6.38}$$

where $V_n(p_\mathrm{T}^a, p_\mathrm{T}^b, p_\mathrm{T}^b, p_\mathrm{T}^b) = \langle V_n^a V_n^b V_n^{b*} V_n^{b*}\rangle$, and $V_n(p_\mathrm{T}^a, p_\mathrm{T}^a, p_\mathrm{T}^a, p_\mathrm{T}^a) = \langle V_n^a V_n^a V_n^{a*} V_n^{a*}\rangle$ and $V_n(p_\mathrm{T}^b, p_\mathrm{T}^b, p_\mathrm{T}^b, p_\mathrm{T}^b) = \langle V_n^b V_n^b V_n^{b*} V_n^{b*}\rangle$. This observable seems very similar with ratio $v_n\{4\}/v_n[4]$. In fact, R_n can be used to test whether the 4-particle correlations can be factorized into single (from certain p_T^a) and 3-particle (from entire p_T^T) correlations, meanwhile $v_n\{4\}/v_n[4]$ checks if the factorization of 4-particle correlations into single (from certain p_T^a) and 3-particle (from certain p_T^b) correlations is valid. The breakdown of factorization for such 4-particle correlations will show more evidence of p_T dependent flow angle and magnitude fluctuations, as the non-flow effects are strongly suppressed in these measurements.

New Observable $SC\{a, T, -a, -T\}$: probe of p_T dependent flow magnitude fluctuations

The ratio $v_n\{4\}/v_n[4]$ and R_n could be considered as a tool to probe the p_T dependent flow angle and magnitude fluctuations, nevertheless it cannot distinguish one effect from the other. Another observable, inspired by $SC_{m,n,-m,-n}$, is designed as:

$$\begin{aligned}
&SC\{a, ref, -a, -ref\} \\
&\equiv \langle \cos[n(\varphi_1^a + \varphi_2^\mathrm{ref} - \varphi_3^a - \varphi_4^\mathrm{ref})]\rangle - \langle \cos n(\varphi_1^a - \varphi_2^a)\rangle\langle \cos n(\varphi_1^\mathrm{ref} - \varphi_2^\mathrm{ref})\rangle \\
&= \langle \cos[n(\varphi_1^a - \Psi_n^a) + n(\varphi_2^\mathrm{ref} - \Psi_n^\mathrm{ref}) - n(\varphi_3^a - \Psi_n^a) - n(\varphi_4^\mathrm{ref} - \Psi_n^\mathrm{ref})]\rangle \\
&\ - \langle \cos[n(\varphi_1^a - \Psi_n^a) - n(\varphi_2^a - \Psi_n^a)]\rangle \langle \cos[n(\varphi_1^\mathrm{ref} - \Psi_n^\mathrm{ref}) - n(\varphi_2^\mathrm{ref} - \Psi_n^\mathrm{ref})]\rangle \\
&= \langle v_n(p_\mathrm{T}^a)^2 {v_n^\mathrm{ref}}^2\rangle - \langle v_n(p_\mathrm{T}^a)^2\rangle\langle {v_n^\mathrm{ref}}^2\rangle
\end{aligned} \tag{6.39}$$

By design, non-zero value of $SC\{a, T, -a, -T\}$ suggests the p_T dependent flow magnitude fluctuations. With this observable, we can further investigate the underlying mechanism of anisotropic flow as well as its fluctuations.

Identified particle $v_n\{2\}$ and $v_n[2]$: probe of p_T dependent angle fluctuations

It was found in hydrodynamic calculations that $v_n\{2\}$ and $v_n[2]$ of identified particle are good probe of p_T dependent angle fluctuations. Figure 6.21 shows the $v_n\{2\}$ and $v_n[2]$ of identified particle for 0-5% Pb–Pb collisions at $\sqrt{s_\mathrm{NN}} = 2.76$ TeV in hydrodynamic calculations (VISH2+1) [215]. For pions, there is no difference of $v_n\{2\}$ and $v_2[2]$, flow angle fluctuations are invisible in the shown p_T region for all flow harmonics; for protons, the deviation of $v_2\{2\}$ and $v_2[2]$ appears at low p_T, it's visible for not only v_2 but also v_3 of proton [215]. The only explanation for such results are the minimum of the variance of the flow angle fluctuations is shifted to higher p_{T} for heavier particles, and that quite generally stronger radial flow shifts all anisotropic flow to higher p_{T} values for heavier particles [215]. Therefore, it's extremely interesting to measure $v_2[2]$ for identified particles, especially the heavy particles, and compare to those $v_2\{2\}$ results presented in Chapter 5, to check if the data confirm such a distinct feature predicted by hydrodynamic calculations. It provides probe of p_{T} dependent flow angle fluctuations and sheds more light on the understanding of anisotropic flow as well as its fluctuations, and better constrains the hydrodynamic model.

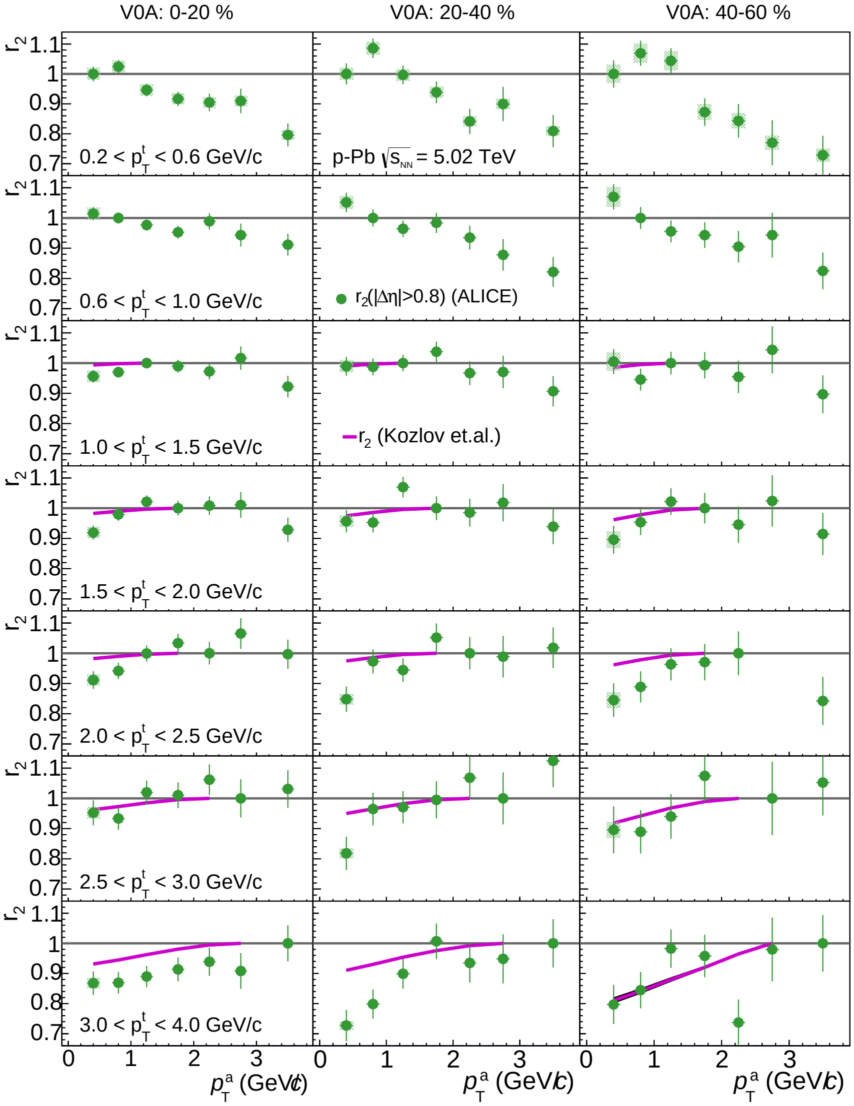

Figure 6.16: Factorization ratio r_2, as a function of p_T^a in bins of p_T^t for multiplicity classes 0-20 %, 20-40 % and 40-60 % in p–Pb collisions at $\sqrt{s_{NN}}$ = 5.02 TeV, are presented by solid magenta circles.

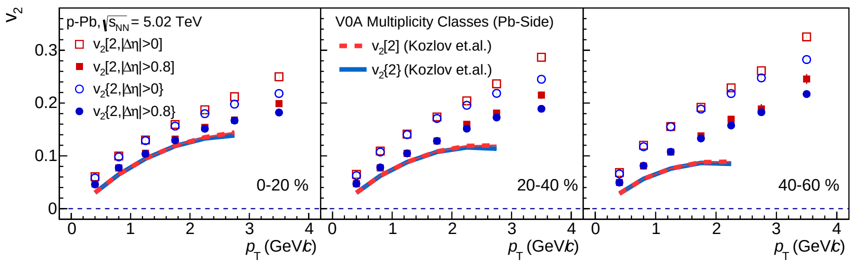

Figure 6.17: The $v_2\{2, |\Delta\eta| > 0\}$, $v_2[2, |\Delta\eta| > 0]$, $v_2\{2, |\Delta\eta| > 0.8\}$ and $v_2[2, |\Delta\eta| > 0.8]$ for various multiplicity classes of p–Pb collisions at $\sqrt{s_{\rm NN}} = 5.02$ TeV.

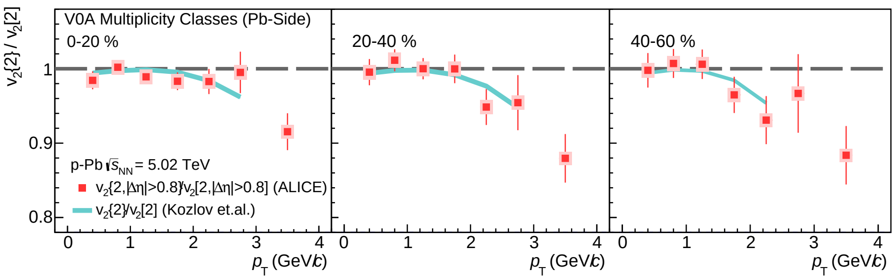

Figure 6.18: The ratio $\frac{v_2\{2,|\Delta\eta|>0.8\}}{v_2[2,|\Delta\eta|>0.8]}$ for various multiplicity classes in p–Pb collisions at $\sqrt{s_{\rm NN}} = 5.02$ TeV.

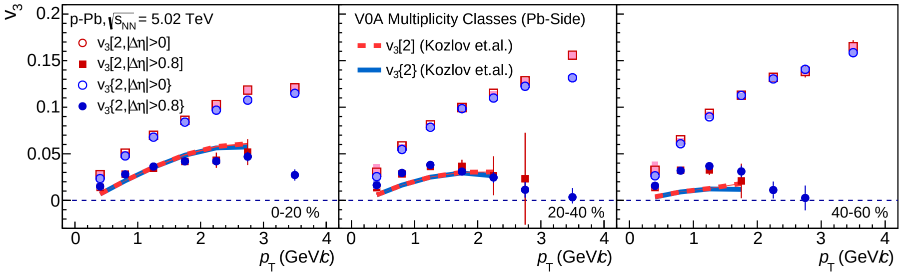

Figure 6.19: The $v_3\{2, |\Delta\eta| > 0\}$, $v_3[2, |\Delta\eta| > 0]$, $v_3\{2, |\Delta\eta| > 0.8\}$ and $v_3[2, |\Delta\eta| > 0.8]$ for various multiplicity classes of p–Pb collisions at $\sqrt{s_{\rm NN}} = 5.02$ TeV.

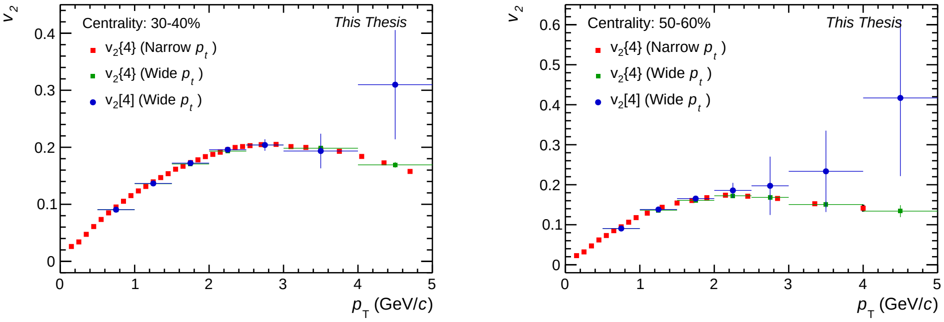

Figure 6.20: p_T-differential $v_2\{4\}$ and $v_2[4]$ in centrality 30-40% (Left) and 50-60% (Right).

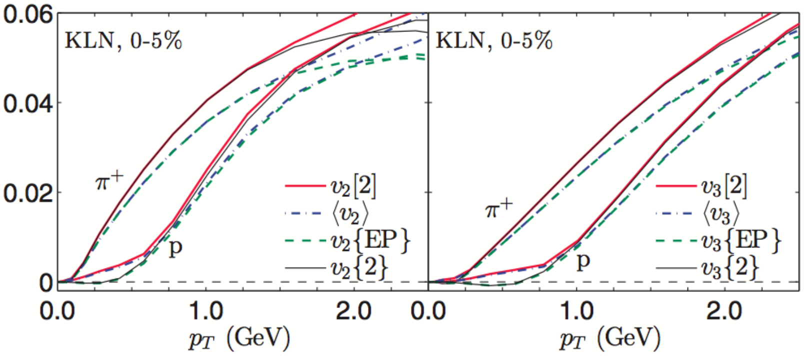

Figure 6.21: $v_{2,3}\{2\}$ and $v_{2,3}[2]$ for pions and protons in central Pb–Pb collisions at $\sqrt{s_{NN}} =$ 2.76 TeV, MC-KLN initial state and $\eta/s = 0.20$. Figure is from [215].

6.3 Correlations of Ψ_n and Ψ_m

The comprehensive understanding of the entire spectrum of anisotropic flow harmonics (v_n) is expected to yield strong constraints on the initial conditions and the dynamics of the system evolution. Systematic studies of v_n at the LHC revealed non-zero v_n values up to $n = 6$. This is in agreement with the expectation of sizable fluctuations in the initial conditions.

The studies of v_n moments and the fits of event-by-event ε_n distributions presented in Section 6.1 provide important information on the underlying *p.d.f.* of the anisotropic flow v_n fluctuations. In addition, the measurements of $v_n\{2\}/v_n[2]$ and r_n presented in Section 6.2 probe the possible p_{T} dependent flow angle and magnitude fluctuations, characterize the reflection of initial geometry fluctuations on the p_{T} differential flow, and how v_n and Ψ_n fluctuate at different p_{T} region. All the above studies broaden our knowledge about fluctuations of each single harmonic, more specifically how v_n and Ψ_n fluctuate event-by-event for each single harmonic. Nevertheless, it is still not clear whether there is a correlation between anisotropic flow v_n and/or participant plane Ψ_n for different harmonics, in other words whether flow vector $\overrightarrow{V}_n = v_n e^{i\,n\Psi_n}$ and $\overrightarrow{V}_m$ are correlated in relativistic heavy-ion collisions. If the initial anisotropy is small and fluctuates randomly, the orientation of each participant plane of a given harmonic n is expected to be uncorrelated to the corresponding orientation for a different harmonic m. However, previous $v_4\{\Psi_2\}$ measurement suggests strong correlations between Ψ_2 and Ψ_4 [124]. In addition, a weak correlation between Ψ_2 and Ψ_3 was measured using 5-particle mixed harmonic cumulant by ALICE [122]. Furthermore, 3- and 4-plane correlations have been examined in the MC-Glauber and MC-KLN model frameworks [215], which show directly the correlations of Φ_n and Φ_m in the initial state.

In this thesis, the 2-, 3- and 4-plane correlations in both initial state and final state will be discussed. The comparison to hydrodynamic calculations and transport model calculations will be presented, which yield valuable insights into the initial conditions and the transport properties of the created mater.

6.3.1 Participant plane correlations in initial state

The initial participant plane correlations can be investigated based on initial state models, where the participant plane could be directly obtained. Several different types of correlations will be discussed in what follows, including 2-plane, 3-plane and 4-plane correlations. The simplest 2-plane correlations are the correlations between n^{th} and $2n^{th}$ order initial participant planes, denoted as (Φ_n, Φ_{2n}), which can be probed via $\langle \cos 2n(\Phi_n - \Phi_{2n}) \rangle$.

Figure 6.22 shows the 2-plane correlations of (Φ_1, Φ_2), (Φ_2, Φ_4) and (Φ_3, Φ_6) predicted by the MC-Glauber model. All these three correlations are negative for the presented centrality classes. The magnitudes of all three correlations increase with increasing centrality percentile. These results could be explained as the interplay between the fluctuations and average shape for the geometry of the overlap area. For instance, in central collisions the system is fluctuation-dominated, which leads to uncorrelated Φ_n and Φ_{2n}, nevertheless the system in peripheral collisions is dominated by geometry,

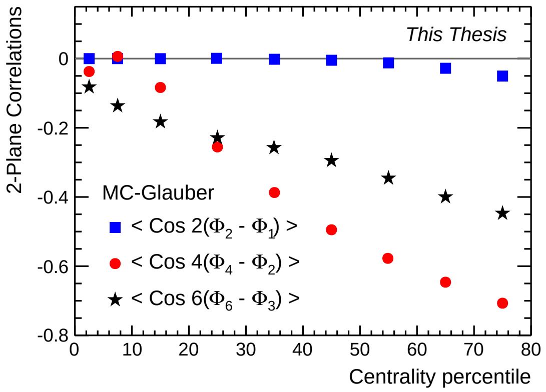

Figure 6.22: Centrality dependence of 2-plane correlations in initial state from MC-Glauber model.

which has ε_{2n} components that are aligned [212], and thus generates the correlations between Φ_n and Φ_{2n} [4].

In addition, results for the 3-plane and 4-plane correlations are also presented in Fig. 6.23 as a function of centrality using the initial state from MC-Glauber model. Negative signs are observed for the presented 3-plane correlations and positive signs are found for the 4-plane correlations. It is interesting to see for instance the strong correlations of (Φ_2, Φ_4, Φ_6), which come from the combinations of correlations of (Φ_2, Φ_4) and (Φ_2, Φ_6), as:

$$2\Phi_2 + 4\Phi_4 - 6\Phi_6 = 4(\Phi_4 - \Phi_2) - 6(\Phi_6 - \Phi_2). \tag{6.40}$$

Although weak correlations of (Φ_2, Φ_3), (Φ_2, Φ_5) and (Φ_3, Φ_5) have been observed so far, a strong correlations among 3-planes are observed in Fig. 6.23 (left), which brings special interest to these correlations. These participant plane correlations are non-zero and reveal novel patterns expected from the average geometry and/or initial state fluctuations. The strong magnitude implies that it is necessary to measure not only 2-plane but also multi-plane correlations to further understand the participant plane correlations. On the other hand, the unique way to confirm and check the sign and magnitude of initial participant plane correlations is via the comparison of final participant plane correlations in experiments and hydrodynamic calculations, which are based on various initial state models and different η/s values. This comparison could shed light on the role of the initial geometry fluctuations and dynamic evolution which might transfer initial participant plane correlations to the final state.

---

[4] We note the magnitude of (Φ_1, Φ_2) correlations in this study is different with those in [212], more investigations are still necessary.

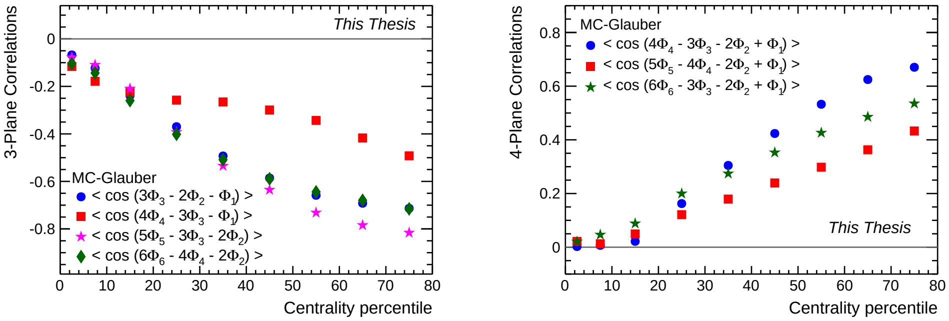

Figure 6.23: Centrality dependence of 3-plane (Left) and 4-plane (Right) correlations in initial state from MC-Glauber model.

6.3.2 Participant plane correlations in the final state via Scalar Product method

Besides the unknown participant planes in initial state, the participant planes in the final state are also unknown in experiment. However, these correlations could be investigated using the Scalar Product (SP) method [222], based on multi-particle correlations technique. If the number of particles in harmonic n is denoted as k_n, the correlations can be generally calculated via:

$$c\{\underbrace{\cdots,n,n,n,\cdots}_{k_n}\} \equiv \frac{\left\langle \prod\limits_{n>0} (q_{nA})^{k_n} \prod\limits_{n<0} (q^*_{nB})^{k_n} \right\rangle}{\sqrt{\prod\limits_{n} \langle (q_{nA})^{k_n} \, (q^*_{nB})^{k_n} \rangle}}, \tag{6.41}$$

with the request $\sum\limits_n nk_n = 0$ by azimuthal symmetry and q_{nA} and q_{nB} are the reduced flow vectors build at sub-events A and B.

A simple example would be 2-plane (Ψ_2, Ψ_4) correlations, which could be achieved by:

$$c\{2,2,-4\} \equiv \frac{\langle q^2_{2A} q^*_{4B} \rangle}{\sqrt{\langle q^2_{2A} q^{2*}_{2B} \rangle}\sqrt{\langle q_{4A} q^*_{4B} \rangle}} = \frac{\langle v_2^2 v_4 \cos\left[4(\Psi_2 - \Psi_4)\right] \rangle}{\sqrt{\langle v_2^4 \rangle}\sqrt{\langle v_4^2 \rangle}} \approx \langle \cos 4(\Psi_4 - \Psi_2) \rangle \,. \tag{6.42}$$

Assuming $\langle v_2^2 v_4 \rangle = \sqrt{\langle v_2^4 \rangle}\sqrt{\langle v_4^2 \rangle}$ (no correlations of v_2 and v_4), $c\{2,2,-4\}$ could be used to probe the (Ψ_2, Ψ_4) correlations.

The centrality dependence of (Ψ_2, Ψ_4) correlations measured by the SP method are presented in Fig. 6.24 (left). A clear difference is observed when two different pseudorapidity gaps are tested with the SP method. As shown in Eq. (6.42), most of the terms are based on 4-particle correlations which are less influenced by non-flow effects, except the 2-particle correlation term $q_{4A}q^*_{4B}$. When the pseudorapidity gap increases, the $q_{4A}q^*_{4B}$

term gives smaller value due to non-flow suppression, and therefore gives bigger value of $c\{2, 2, -4\}$ in the end. For later studies, a $|\Delta\eta| > 0.8$ gap is applied as default. It is also observed that the (Ψ_2, Ψ_4) correlations increase from central to peripheral collisions. This could be understood as coming mainly from the non-linear response of the flow vector $V_n = v_n e^{in\Psi_n}$ to initial anisotropy $\varepsilon_n e^{in\Phi_n}$ in hydrodynamics [203]. The final n^{th} order participant plane Ψ_n is not only driven by initial n^{th} order participant plane Φ_n, but also by contributions from other participant plane(s). For instance, the 4^{th} order harmonic v_4 and its corresponding participant plane Ψ_4 are determined by linear and quadratic response as following:

$$v_4 e^{-i4\Psi_4} = w_4 e^{-i4\Phi_4} + w_{4(22)} e^{-i4\Phi_2}. \tag{6.43}$$

Here w_4 describes the linear response and it is proportional to ε_4; $w_{4(22)}$ describes the non-linear response and is proportional to ε_2^2. The non-linear response couples v_4 to v_2^2. Thus, the increase of v_2 from central to peripheral collisions drives the increasing of the correlations of (Ψ_2, Ψ_4) [222].

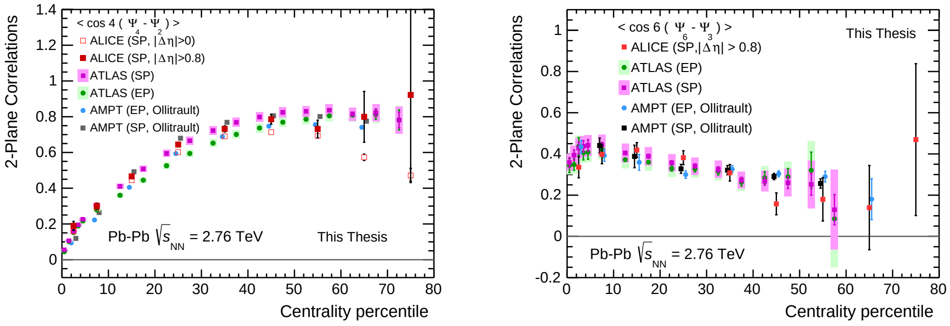

Figure 6.24: (Color online) The centrality dependence of 2-plane correlations at $\sqrt{s_{\rm NN}} = 2.76$ TeV Pb–Pb collisions.

These results of (Ψ_2, Ψ_4) correlations are compared to the measurements from ATLAS [221] using both SP and EP methods. Very good agreement is observed for the results using SP method from ALICE and ATLAS, both show stronger (Ψ_2, Ψ_4) correlations than the one measured by the EP method. The difference between SP and EP measurements was argued to originate from flow fluctuations affecting the event plane resolution correction [222]. In addition, the calculations based on the AMPT model [222] are compared to the experimental measurements in Fig. 6.24 (left). The calculation using SP method describes the ALICE data fairly well, and it also shows a significant difference *w.r.t.* the EP calculations from AMPT model.

Similarly, the 2-plane (Ψ_3, Ψ_6) correlations can be studied by:

$$c\{3, 3, -6\} \equiv \frac{\langle q_{3A}^2 q_{6B}^* \rangle}{\sqrt{\langle q_{3A}^2 q_{3B}^{2*} \rangle}\sqrt{\langle q_{6A} q_{6B}^* \rangle}} \approx \langle \cos 6(\Psi_6 - \Psi_3) \rangle \,. \tag{6.44}$$

The centrality dependence of (Ψ_3, Ψ_6) correlations measured by the SP method are presented in Fig. 6.24 (right). It is seen that the correlations decrease with increasing centrality. This could be understand as contributions from a linear response to $\varepsilon_6\, e^{i6\Phi_6}$ and a non-linear response to $\varepsilon_3^2\, e^{i3\Phi_3}$ of the initial state. At the same time, the (Ψ_3, Ψ_6) correlations measured by SP method from ALICE are consistent with the measurements using both SP and EP methods from ATLAS, within uncertainty. The AMPT model quantitatively agree with the measurements from ALICE and ATLAS, and shows tiny difference of (Ψ_3, Ψ_6) correlations calculated by SP and EP method. This is in agreement with what was observed in SP and EP measurements from ATLAS.

On the other hand, in [204] the authors pointed out the influence of the initial state models and the value of η/s on the participant plane correlations. In general, stronger initial symmetry plane correlations are reflected in stronger correlations of the final state symmetry planes. Furthermore, the calculations using smaller η/s to describe the QGP produced in the hydrodynamic system, generates stronger correlations in the final state. An example is the 3^{rd} and 6^{th} order participant plane correlation presented in Fig. 2 of [204], where similar magnitudes of 3^{rd} and 6^{th} order participant plane correlation in the initial state from MC-Glauber and MC-KLN models can be found. However, the one which uses $\eta/s = 0.08$ generates stronger 3^{rd} and 6^{th} order participant plane correlation compared to the one with $\eta/s = 0.20$ in the final state. Therefore, the measurements of participant plane correlations are proposed as new approaches to constrain the initial conditions and η/s of QGP.

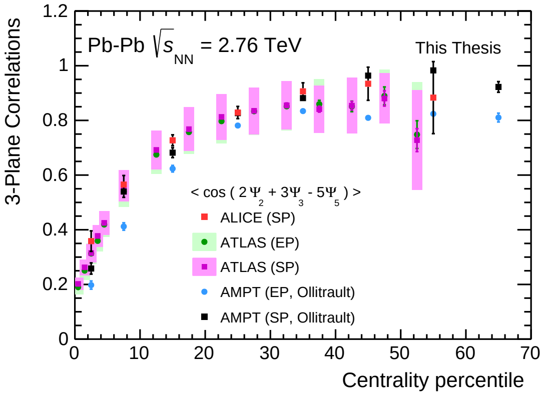

Figure 6.25: (Color online) The centrality dependence of 3-plane correlations at $\sqrt{s_{\rm NN}} = 2.76$ TeV Pb–Pb collisions.

Not only 2-plane but also 3-plane correlations have been measured via the SP method. Following Eq. (6.41), the 3-plane (Ψ_2, Ψ_3, Ψ_5) correlations could be calculated as:

$$c\{2,3,-5\} \equiv \frac{\langle q_{2A} q_{3A} q_{5B}^{*} \rangle}{\sqrt{\langle q_{2A} q_{2B}^{*} \rangle}\sqrt{\langle q_{3A} q_{3B}^{*} \rangle}\sqrt{\langle q_{5A} q_{5B}^{*} \rangle}}. \tag{6.45}$$

The centrality dependence of 3-plane correlation (Ψ_2, Ψ_3, Ψ_5) is plotted in Fig. 6.25. The ALICE measurements, denoted with red full squares, increase from central to peripheral collisions. Although no (or very weak) correlations was found between 2-plane (Ψ_2, Ψ_3)

correlations [122], there is a strong correlation when a third plane Ψ_5 is introduced. In fact, this result can also be explained by the contributions from linear and non-linear response of the form:

$$v_5\, e^{-i5\Psi_5} = w_5\, e^{-i5\Phi_5} + w_{5(23)}\, e^{-i2\Phi_2}\, e^{-i3\Phi_3} \tag{6.46}$$

Here w_5 quantifies the linear response and it is proportional to ε_5, while $w_{5(23)}$ describes the non-linear response and is proportional to $\varepsilon_2\varepsilon_3$. The centrality dependence of $c\{2,3,-5\}$ shown in Fig. 6.25 is driven by the coupling between v_5 and v_2v_3. These results are also compared to ATLAS measurements performed with the EP and the SP methods. It can be seen that there is very small difference of SP and EP measurements in ATLAS, both results are consistent with SP measurements in ALICE. In addition, Fig. 6.25 shows results from the AMPT model extracted with the EP and the SP methods. The AMPT calculations using SP method seem to be in fairly good agreement with experimental measurements. Meanwhile, the calculations using EP method seems to be systematically lower than the measurements. The small difference of 3-plane correlation (Ψ_2, Ψ_3, Ψ_5) using SP and EP methods is not reproduced by the AMPT calculations.

6.3.3 Outlook: Validation of Scalar Product method

A 4-plane $(\Psi_2, \Psi_3, \Psi_4, \Psi_5)$ correlation provides unique way to check the validation of the participant plane correlations via SP method, which has been proposed in [222]. This is because this correlation could be built approximately by the composition of 2-plane (Ψ_2, Ψ_4) correlation and 3-plane (Ψ_3, Ψ_4, Ψ_5) correlation with:

$$\begin{aligned} c\{2,-3,-4,5\} &\approx \langle \cos(2\Psi_2 - 3\Psi_3 - 4\Psi_4 + 5\Psi_5)\rangle \\ &= \langle \cos\left[(2\Psi_2 + 2\Psi_2 - 4\Psi_4) + (-2\Psi_2 - 3\Psi_3 + 5\Psi_5)\right]\rangle \\ &= \langle \cos(2\Psi_2 + 2\Psi_2 - 4\Psi_4)\rangle \cdot \langle \cos(-2\Psi_2 - 3\Psi_3 + 5\Psi_5)\rangle \\ &\approx c\{2,2,-4\} \cdot c\{-2,-3,5\}. \end{aligned} \tag{6.47}$$

Here (Ψ_2, Ψ_4) and (Ψ_3, Ψ_4, Ψ_5) correlations have been measured in Fig. 6.24 (left) and Fig. 6.25. The $c\{2,-3,-4,5\}$ measurement could be used to check the validation of SP method, by comparison to the product of measurements of $c\{2,2,-4\}$ and $c\{-2,-3,5\}$ (or $c\{2,3,-5\}$).

The first look of this 4-plane correlations is shown in Fig. 6.26. The blue circles show the direct measurement of 4-plane correlations $(\Psi_2, \Psi_3, \Psi_4, \Psi_5)$ via SP method while red squares show the calculations from (Ψ_2, Ψ_4) and (Ψ_3, Ψ_4, Ψ_5) correlations. There is a clear difference between the direct measurements and the calculations, which indicates the required improvement of the SP method which we will discuss in next section.

So far the different centrality dependence of $(\Phi_m,\, \Phi_n)$ obtained from MC-Glauber model calculations and $(\Psi_m,\, \Psi_n)$ correlations measured via SP method have been presented. Interesting correlation patterns have been observed in both initial and final states. The participant plane correlations are supposed to be independent of the magnitude of anisotropic flow v_n. Thus, the comparison of the participant plane correlations measured by the SP method and the hydrodynamic calculations will yield new constraints of the initial state conditions as well as η/s of the QGP in hydrodynamic

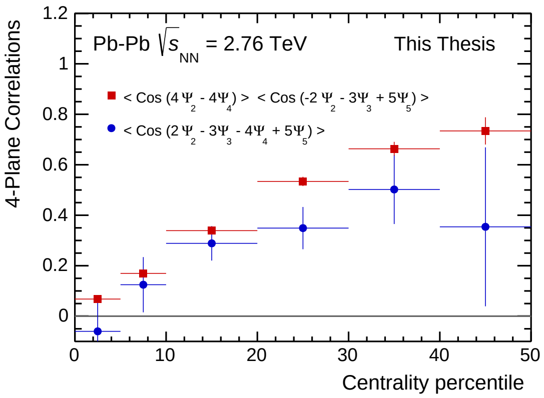

Figure 6.26: (Color online) The centrality dependence of 4-plane correlations at $\sqrt{s_{\rm NN}} = 2.76$ TeV Pb–Pb collisions.

calculations, in addition to previous anisotropic flow studies. Unfortunately, due to the lack of hydrodynamic calculations using the SP method, the apple-to-apple comparison of experimental measurements of participant plane correlations and hydrodynamic calculations are not available yet.

However, as mentioned above, the SP method uses the assumption the multi-particle correlations could be factorized into the product of few-particle correlations. For instance, $\langle v_n^2 v_{2n}\rangle = \sqrt{\langle v_n^4\rangle}\sqrt{\langle v_{2n}^2\rangle}$ or $\langle v_{n_1} v_{n_2} v_{n_3}\rangle = \sqrt{\langle v_{n_1}^2\rangle}\sqrt{\langle v_{n_2}^2\rangle}\sqrt{\langle v_{n_3}^2\rangle}$. If there is a correlation between the event-by-event fluctuations of v_n and v_{2n} (or v_{n_1}, v_{n_2} or v_{n_3}), then this assumption is not valid. Therefore, we should investigate the correlations of v_n and v_m.

6.4 Correlations of v_n and v_m fluctuations

6.4.1 Standard Candles

We now introduce a new type of observable for anisotropic flow analyses, the so-called *standard candles (SC)*:

$$\langle\langle\cos(m\varphi_1+n\varphi_2-m\varphi_3-n\varphi_4)\rangle\rangle \ . \tag{6.48}$$

In the case $m = n$, Eq. (6.48) gives back $v_n\{4\}$ measured with 4-particle cumulants. If $m \neq n$, then the isotropic part of the corresponding four-particle cumulant is given by:

$$\begin{aligned}\langle\langle\cos(m\varphi_1+n\varphi_2-m\varphi_3-n\varphi_4)\rangle\rangle_c &= \langle\langle\cos(m\varphi_1+n\varphi_2-m\varphi_3-n\varphi_4)\rangle\rangle \\ &\quad - \langle\langle\cos[m(\varphi_1-\varphi_2)]\rangle\rangle\,\langle\langle\cos[n(\varphi_1-\varphi_2)]\rangle\rangle \\ &= \left\langle v_m^2 v_n^2\right\rangle - \left\langle v_m^2\right\rangle\left\langle v_n^2\right\rangle . \end{aligned} \tag{6.49}$$

Due to the definition, any dependence on the participant planes Ψ_m and Ψ_n is canceled. A lot of terms which appear in the general cumulant expansion, for instance

$\langle\langle\cos(m\varphi_1 - n\varphi_2)\rangle\rangle$, are non-isotropic, therefore average to zero for a detector with uniform acceptance. For fixed values of v_m and v_n over all events, the four-particle cumulant as defined in Eq. (6.49) is zero by definition. This observable is also less sensitive to non-flow correlations, which should be strongly suppressed in 4-particle cumulants. In fact, the four-particle cumulant is equal to zero not only when v_m and v_n are fixed for all events, but also when there is no correlations of event-by-event fluctuations of v_m and v_n. Thus, the $SC_{m,n,-m,-n}$ measurement is non-zero if there is correlations of v_n and v_m. By measuring $SC_{m,n,-m,-n}$ we will know whether finding v_m larger than $\langle v_m\rangle$ in an event will enhance or reduce the probability of finding v_n larger than $\langle v_n\rangle$ in that event, which is not constrained by any measurement performed yet. Recently, by using different observables and methodology, these correlations between fluctuations of various harmonics have been studied in [206, 207].

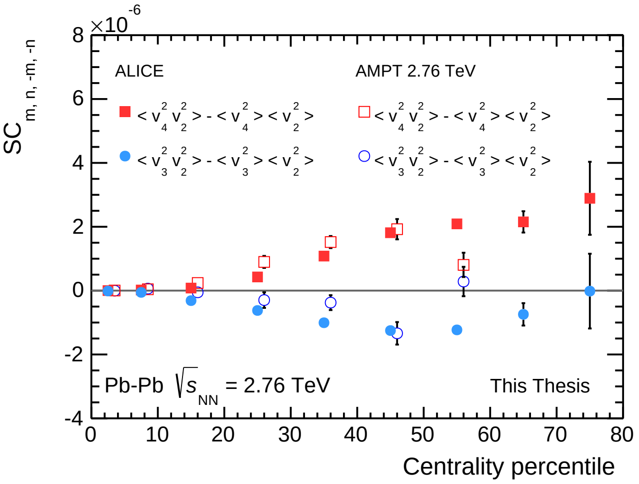

Figure 6.27: (Color online) The centrality dependence of standard candles $SC_{4,2,-4,-2}$ (red markers) and $SC_{3,2,-3,-2}$ (blue markers) at $\sqrt{s_{\rm NN}}$ = 2.76 TeV Pb–Pb collisions by ALICE. The AMPT calculations are presented by open markers.

In Fig. 6.27 we see a clear non-zero value for both $SC_{4,2,-4,-2}$ (red markers) and $SC_{3,2,-3,-2}$ (blue markers) in Pb–Pb collisions at $\sqrt{s_{\rm NN}}$ = 2.76 TeV. The positive results of $SC_{4,2,-4,-2}$ suggest a positive correlation between the event-by-event fluctuations of v_2 and v_4, which indicates that finding v_2 larger than $\langle v_2\rangle$ in an event enhances the probability of finding v_4 larger than $\langle v_4\rangle$ in that event. On the other hand, the negative results of $SC_{3,2,-3,-2}$ imply that finding v_2 larger than $\langle v_2\rangle$ enhances the probability of finding v_3 smaller than $\langle v_3\rangle$.

To better understand the results of $SC_{m,n,-m,-n}$ measured in experiments, the$SC_{m,n,-m,-n}$ have been obtained in initial state. The calculations are performed via $\left\langle \varepsilon_n^2 \varepsilon_m^2 \right\rangle - \left\langle \varepsilon_n^2 \right\rangle \left\langle \varepsilon_m^2 \right\rangle$ using the MC-Glauber model. The centrality dependence of $SC_{4,2,-4,-2}$ and $SC_{3,2,-3,-2}$ are presented as red squares and blue circles in Fig. 6.28. Positive and increasing trend from central to peripheral collisions has been observed for $SC_{4,2,-4,-2}$,

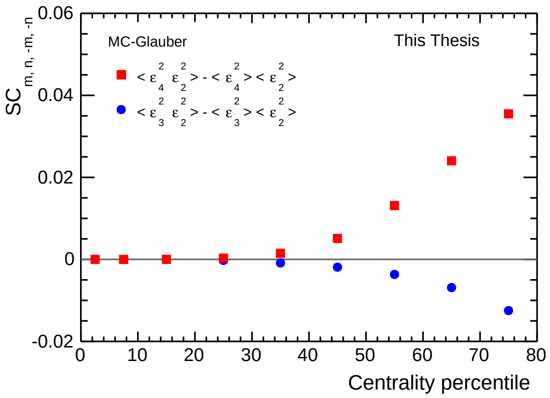

Figure 6.28: (Color online) The centrality dependence of standard candles $SC_{4,2,-4,-2}$ (red markers) and $SC_{3,2,-3,-2}$ (blue markers) in initial state from MC-Glauber model.

in contrast, negative and decreasing trend was observed for $SC_{3,2,-3,-2}$ in MC-Glauber model calculations. This shows that finding ε_2 larger than $\langle\varepsilon_2\rangle$ in an event enhances the probability of finding ε_4 larger than $\langle\varepsilon_4\rangle$, while in parallel enhancing the probability of finding ε_3 smaller than $\langle\varepsilon_3\rangle$ in that event. In addition, the positive $SC_{4,2,-4,-2}$ and negative $SC_{3,2,-3,-2}$ calculated in initial state agree with the positive $SC_{4,2,-4,-2}$ and negative $SC_{3,2,-3,-2}$ measured in experiments. This might indicate that the correlations of ε_n and ε_m in initial state leads to the correlations of v_n and v_m. Furthermore, the calculations of AMPT model in final state qualitatively describe the centrality dependence of $SC_{m,n,-m,-n}$ measurements at LHC, while in initial state the results of $SC_{m,n,-m,-n}$ from AMPT is compatible with MC-Glauber calculations (not shown here). These results further suggest the initial ε_n and ε_m correlations as the origin of v_n and v_m correlations in the final state.

6.4.2 Outlook: Modified Scalar Product method for the Ψ_n and Ψ_m correlations

From the study of correlations between different flow harmonics (v_n and v_m), we find the assumption that multi-particle correlations could be factorized into the product of few-particle correlations sometimes does not hold. Therefore, the participant plane correlations measured by the SP method might be biased measurements, due to the correlations of v_n and v_m.

To better understand the participant plane correlations measured via the SP method, it is crucial to investigate to what extent the assumption:

$$\frac{\left\langle v_2^2\, v_4 \cos\left[4\left(\Psi_2 - \Psi_4\right)\right]\right\rangle}{\sqrt{\langle v_4^2\rangle}\sqrt{\langle v_2^4\rangle}} = \left\langle\cos\left[4\left(\Psi_2 - \Psi_4\right)\right]\right\rangle , \tag{6.50}$$

is valid, more specifically, how big is the difference of $\langle v_2^2 v_4\rangle$ and $\sqrt{\langle v_4^2\rangle}\sqrt{\langle v_2^4\rangle}$. The

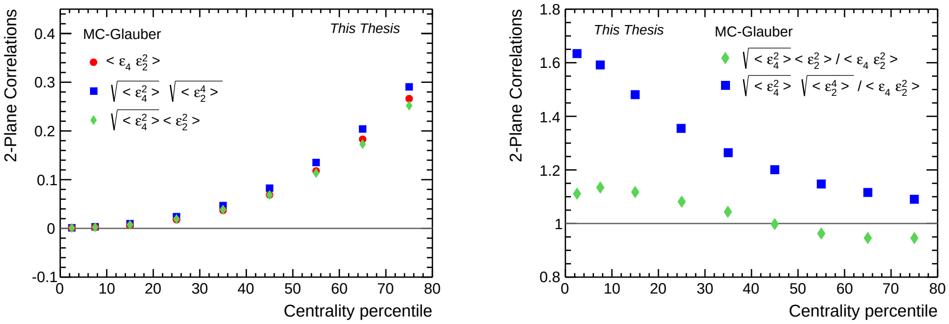

Figure 6.29: (Color online) Centrality dependence of correlations of event-by-event fluctuations of ε_2 and ε_4 in MC-Glauber model.

possible difference will show the bias of the measurements from SP method w.r.t. the true value of participant plane correlations. Assuming $v_n \propto \varepsilon_n$, if we have $\langle v_4 v_2^2 \rangle = \sqrt{\langle v_4^2 \rangle}\sqrt{\langle v_2^4 \rangle}$, we should also have $\langle \varepsilon_4 \varepsilon_2^2 \rangle = \sqrt{\langle \varepsilon_4^2 \rangle}\sqrt{\langle \varepsilon_2^4 \rangle}$.

Figure 6.29 (left) presents the centrality dependence of $\langle \varepsilon_4 \varepsilon_2^2 \rangle$ (red circle), $\sqrt{\langle \varepsilon_4^2 \rangle}\sqrt{\langle \varepsilon_2^4 \rangle}$ (blue square) and $\sqrt{\langle \varepsilon_4^2 \rangle \langle \varepsilon_2^2 \rangle}$ (green diamond) from MC-Glauber calculations. To make the difference of these three calculations more clear, the ratios of $\sqrt{\langle \varepsilon_4^2 \rangle \langle \varepsilon_2^2 \rangle}$ to $\langle \varepsilon_4 \varepsilon_2^2 \rangle$ (green diamond) and $\sqrt{\langle \varepsilon_4^2 \rangle}\sqrt{\langle \varepsilon_2^4 \rangle}$ to $\langle \varepsilon_4 \varepsilon_2^2 \rangle$ (blue square) are shown in Fig. 6.29 (right). It is found that $\sqrt{\langle \varepsilon_4^2 \rangle}\sqrt{\langle \varepsilon_2^4 \rangle}$ is dramatically higher than $\langle \varepsilon_4 \varepsilon_2^2 \rangle$ for the entire centrality classes, it exceeds 60 % in the most central collisions. It indicates that the (Ψ_2, Ψ_4) correlations measured via SP method, which are based on the assumption $\langle v_4 v_2^2 \rangle = \sqrt{\langle v_4^2 \rangle}\sqrt{\langle v_2^4 \rangle}$, might be biased strongly due to the correlations of event-by-event fluctuations of v_2 and v_4. That the calculation of $\sqrt{\langle \varepsilon_4^2 \rangle \langle \varepsilon_2^2 \rangle}$ is closed to $\langle \varepsilon_4 \varepsilon_2^2 \rangle$, within 10 % for presented centrality classes as seen in Fig. 6.29 (right). This result implies that compared to $\sqrt{\langle v_2^4 \rangle}\sqrt{\langle v_4^2 \rangle}$ used in Eq. (6.42), $\langle v_2^2 \rangle \sqrt{\langle v_4^2 \rangle}$ is a better estimation of $\langle v_2^2 \, v_4 \rangle$. Therefore, a modified SP method, defines the new (Ψ_2, Ψ_4) as:

$$C\{2,2,-4\} \equiv \frac{\left\langle \frac{Q_{2A}^2 Q_{4B}^*}{M_A^2 M_B} \right\rangle}{\left\langle \frac{Q_{2A} Q_{2B}^*}{M_A M_B} \right\rangle \sqrt{\left\langle \frac{Q_{4A} Q_{4B}^*}{M_A M_B} \right\rangle}} = \frac{\langle v_2^2 v_4 \cos\left[4(\Psi_2 - \Psi_4)\right] \rangle}{\langle v_2^2 \rangle \sqrt{\langle v_4^2 \rangle}} \tag{6.51}$$

It should give more precise measurement of (Ψ_2, Ψ_4) correlations compared to the previous one defined in Eq. (6.42).

Furthermore, if we assume that $v_n \propto \varepsilon_n$, we have $\frac{\langle v_2^2 v_4 \rangle}{\langle v_2^2 \rangle \sqrt{\langle v_4^2 \rangle}} \frac{\langle \varepsilon_2^2 \rangle \sqrt{\langle \varepsilon_4^2 \rangle}}{\langle \varepsilon_2^2 \varepsilon_4 \rangle} = 1$. Then we can scaled the $C\{2,2,-4\}$ with $\frac{\langle \varepsilon_2^2 \rangle \sqrt{\langle \varepsilon_4^2 \rangle}}{\langle \varepsilon_2^2 \varepsilon_4 \rangle}$ and in the end obtain:

$$C\{2,2,-4\}_{scaled} = C\{2,2,-4\} \frac{\langle \varepsilon_2^2 \rangle \sqrt{\langle \varepsilon_4^2 \rangle}}{\langle \varepsilon_2^2 \varepsilon_4 \rangle} \approx \langle \cos\left[4(\Psi_2 - \Psi_4)\right] \rangle \tag{6.52}$$

Such observable might be less influenced by the correlations of event-by-event fluctuations of v_2 and v_4, then previous proposed observable $c\{2, 2, -4\}$ with SP method, although the measurements depend on the initial model we apply.

In summary, a new tool, the correlations among different orders of flow vector $\overrightarrow{V}_n$ are investigated. More specifically, both the correlations between participant plane Ψ_n and Ψ_m as well as the correlations between their corresponding harmonic flow v_n and v_m, are emerging with a promise to shed addition light on the initial state phenomena and dynamical evolution of the medium created in heavy ion collisions.

Chapter 7

Summary

In this thesis, detailed anisotropic flow measurements obtained in Pb–Pb collisions at $\sqrt{s_{\mathrm{NN}}} = 2.76$ TeV as well as p–Pb collisions at $\sqrt{s_{\mathrm{NN}}} = 5.02$ TeV were presented. The main goal of these measurements was to understand the nature of anisotropic flow and its response to the initial geometry of the created system as well as its fluctuations.

Since 2000, systematic studies of anisotropic flow in both experiments and theory have been performed. Studies of anisotropic flow at RHIC revealed that the system created in heavy-ion collisions behaves as an almost perfect liquid. This picture did not change after the first measurements at the LHC, i.e. the system at the LHC still behaves as an almost perfect liquid. Further analysis of LHC data showed clearly that not only even but also odd harmonics develop and become significant in heavy-ion collisions. The sizable triangular flow v_3 and pentagonal flow v_5 measurements could be understood as a consequence of the event-by-event fluctuations of initial spatial distributions of the created hot and dense matter. These higher harmonics provide a natural explanation of the double hump structure in two-particle correlations, which was interpreted up to that moment as a Mach cone response to fast partons. In addition, these higher harmonics provide new constraints on both the initial conditions and the shear viscosity to entropy density ratio η/s via hydrodynamic calculations. Although there is still a long way to go before we can claim to have full knowledge of the initial conditions and η/s of the QGP. However, the comparison between data and various hydrodynamic calculations suggest that IP-Glasma initial conditions and η/s =0.20 by far gives the best descriptions of data. Details are discussed in Section 5.2.

The anisotropic flow of not only charged particles but also identified particles have been measured by ALICE. Systematic measurements of elliptic flow of identified particles, including the ϕ meson, have been discussed in Section 5.3. In the low p_{T} region, schematically defined by $p_{\mathrm{T}} <$ 2-3 GeV/c, a mass ordering is observed, with heavier particles exhibiting lower v_2 values for fixed p_{T}. This could be understood as the interplay between radial flow and elliptic flow, which pushes heavier particles to lower v_2 at low p_{T}. The comparison to hydrodynamic calculations coupled to a hadronic cascade model shows that this model fails to reproduce quantitatively the v_2 for the majority of heavy particles. In particular for the ϕ-meson, the comparison suggests that a bigger hadronic cross sections needs to be used in transport model calculations. At intermediate p_T, the results show clearly that the number of constituent quark scaling does not hold precisely, which might conflict with expectations from a simple quark coalescence mechanism. Most importantly, it was found that the ϕ meson v_2 seems to follow, within uncertainties, the flow of baryons in central collisions, and shifts progressively to the flow of mesons for peripheral collisions, at intermediate p_T. Combined with the p_T distributions of the p/ϕ ratio, these results suggest that not only the number of quarks but also the particle mass is a key ingredient also in this transverse momentum range.

In chapter 6, detailed measurements of flow fluctuations were presented. The search of the underlying probability density function ($p.d.f.$) for event-by-event v_n distributions has been discussed via the measurements of different order cumulants of v_n. In addition, the initial anisotropy ε_n distributions were studied and their event-by-event distributions were fitted with various types of functions. It was found that the Elliptic-Power function is the most promising candidate of the underlying $p.d.f.$ of v_n distributions. This function quantitatively reproduces both the ε_2 and ε_3 distributions simultaneously in all centrality classes, and predicts non-zero values of higher order cumulants of v_3 and ε_3. Furthermore, the p_T dependent fluctuations of the flow angle (Ψ_n) and the magnitude (v_n) have been studied by the $v_n\{2\}/v_n[2]$ and r_n measurements. These results indicate that the p_T dependent flow angle and magnitude fluctuations, are limited within 10% in non-central collisions, while being more pronounced in most central collisions at the presented p_T range. There is no indication of p_T dependent flow angle and magnitude fluctuations of higher harmonics so far, within the large statistical uncertainty of the measurements. The comparison with two hydrodynamic calculations shows that our data favour the description of hydrodynamic calculations with MC-KLN (CGC) initial conditions and $\eta/s = 0.20$ over MC-Glauber initial conditions and $\eta/s = 0.08$. However, both of these two calculations overestimate the possible p_T dependent effects. Several new observables, using multi-particle techniques, are proposed to probe the p_T dependent flow angle and magnitude fluctuations. These observables are less sensitive to non-flow effects and will allow to further probe the p_T dependent flow angle fluctuations and p_T dependent flow magnitude fluctuations separately. See Section 6.2 for more details. Finally, in Section 6.3 and 6.4, interesting correlation pattens are observed between Ψ_n, Ψ_m and v_n, v_m. The measurements of participant plane correlations could be nicely explained by a non-linear hydrodynamic response to the initial ε_n and Φ_n. Even though a direct, quantitative comparison of experimental measurements and hydrodynamic calculations using the same technique is still missing, the qualitatively comparison already shows that these new observables promise to provide additional constraints on the initial state phenomena and dynamical evolution of the medium created in heavy ion collisions.

Chapter 8

Summary

In dit proefschrift zijn gedetailleerde metingen van anisotrope flow in Pb–Pb botsingen gepresenteerd bij botsingsenergieën van $\sqrt{s_{\rm NN}} = 2.76$ TeV in p–Pb botsingen bij $\sqrt{s_{\rm NN}} = 5.02$ TeV. Het voornaamste doel van deze metingen is het beter begrijpen van de eigenschappen van anisotrope flow en de invloed hierop van de initiële geometrie van het gecreëerde systeem, alsmede van de schommelingen.

Sinds 2000 is anisotrope flow systematisch bestudeerd, zowel vanuit de theorie als in experimenten. Onderzoek naar anisotrope flow, gedaan bij RHIC, heeft aangetoond dat de materie die gecreëerd wordt bij zware-ionenbotsingen zich gedraagt als een vrijwel perfecte vloeistof. De eerste metingen van de LHC hebben dit beeld niet veranderd: het systeem gedraagt zich in de LHC nog steeds als een vrijwel perfecte vloeistof. Verder onderzoek bij de LHC echter, heeft duidelijk laten zien dat niet alleen even, maar ook oneven harmonische coëfficiënten zich ontwikkelen in zware-ionenbotsingen, en hier ook een belangrijke rol spelen. De waargenomen driehoeks- (v_3) en vijfhoeksflow (v_5) kunnen verklaard worden vanuit variaties in de initiële ruimtelijke verdeling van de hete, zeer dichte materie die in botsingen ontstaat. Deze hogere harmonische coëfficiënten geven een natuurlijke verklaringen voor de 'twee bulten structuur' die gezien wordt in tweedeeltjes correlaties; eerder werd dit toegeschreven aan de Mach-trechter respons van snelle partonen. Voorts begrenzen hogere harmonische coëfficiënten de initiële toestand en het quotiënt van dynamische viscositeit en entropie, η/s, door middel van voorspellingen vanuit de hydrodynamica. Er moet echter vermeld worden dat er nog een lang weg te gaan is voordat volledig begrip van de intiële toestand en η/s van het QGP geclaimd kan worden. Een vergelijking met diverse hydrodynamische modellen suggereert echter dat een IP-Glasma initële toestand met $\eta/s = 0.20$ veruit de beste vergelijking met de meetgegevens geeft. Details hierover worden gegeven in Sec. 5.2.

ALICE heeft, behalve van geladen deeltjes, ook anisotrope flow van geïdentificeerde deeltjes gemeten. Metingen van de elliptische flow van deze geïdentificeerde deeltjes, waaronder het ϕ-meson, zijn besproken in 5.3. Voor deeltjes met een lage transversale impuls ($p_{\rm T} <$ 2-3 GeV/c) wordt een ordening van flow naar massa waargenomen: zwarte deeltjes hebben bij gelijke pt lagere v_2 waarden dan lichte deeltjes. Dit kan verklaard worden uit een samenspel van radiële flow en elliptische flow, dat de elliptische flow van zware deeltjes onderdrukt bij lage p_{T}. Berekeningen vanuit hydrodynamica, gekoppeld aan een hadronisch cascademodel, kunnen v_2 niet kwalitatief reproduceren voor het merendeel van de zware deeltjes. De vergelijking toont dat, in het bijzonder voor het ϕ-meson, de werkzame hadronische doorsnede van belang is en meegenomen moet worden in transportmodelberekeningen. Bij tussenliggende pt wordt zichtbaar dat een precies schalen van v_2 met het aantal valentiequarks niet gevonden wordt, hetgeen niet overeenstemt met verwachtingen van een simpel quarkbotsingsmechanisme. De meest opmerkelijke observatie is dat v_2 van het ϕ-meson binnen de meetonzekerheden, in centrale botsingen eenzelfde flow heeft als de baryonen, welke, bij tussenliggende pt, langzaam verschuift naar flow van mesonen voor perifere botsingen. Dit, samen met de pt verdeling van de p/ϕ ratio, suggereert dat niet slechts het aantal valentiequarks, maar ook de deeltjesmassa een belangrijke invloed op v_2 heeft in dit pt interval.

In hoofdstuk 6 zijn gedetailleerde metingen van flowschommelingen gepresenteerd. De zoektocht naar de onderliggende waarschijnlijkheidsdichtheid (*p.d.f.*) van de botsing-tot-botsing verdeling van v_n is besproken aan de hand van meetgegevens van verscheidene cumulanten van de v_n verdeling. Bijkomend zijn de initiële anisotropie ε_n verdelingen bestudeerd. De bijbehorende botsing-per-botsing verdelingen zijn beschreven met verscheidene functies; de ‘elliptic-power’ functie is de meest belovende keuze als beschrijving van de onderliggende waarschijnlijkheidsdichtheid van de v_n verdelingen. Deze functie reproduceert kwalitatief zowel de ε_2 en ε_3 verdeling gelijktijdig in alle centraliteitsklassen en voorspelt eindige waarden voor de hogere orde cumulanten van v_3 en ε_3.

Verder zijn p_{T}-afhankelijke schommelingen van de flowhoek (Ψ_n) en flowgrootte (v_n) bestudeerd door middel van $v_n\{2\}/v_n[2]$ en r_n metingen. De resultaten geven aan dat p_{T}-afhankelijke schommelingen in de flowhoek en grootte maximaal 10% bedragen in niet-centrale botsingen, maar meer uitgesproken zijn in centrale botsingen. Er zijn, binnen de statistische onzekerheden op de metingen, geen aanwijzingen voor dergelijke schommelingen bij hogere harmonische coëfficiënten. Vergelijkingen met twee hydrodynamische voorspellingen laten zien dat de meetgegevens beter overeenstemmen met een MC-KLN (CGC) initiële toestand met $\eta/s = 0.20$ dan met een MC-Glauber initiële toestand met $\eta/s = 0/02$. Beide voorspellingen echter overschatten mogelijke p_{T}-afhankelijke effecten. Diverse nieuwe waarnemingen, gebaseerd op meer-deeltjes technieken, worden voorgesteld om de schommelingen in flowhoek en grootte te onderzoeken. Deze metingen zullen minder gevoelig zijn voor non-flow effecten en bieden de mogelijkheid om schommelingen in de flowhoek en grootte onafhankelijk van elkaar te meten (zie Sec. 6.2 voor meer details). In Sec. 6.3 en 6.4 worden interessante correlatiepatronen tussen Ψ_n, Ψ_m en v_n, v_m waargenomen. De metingen van correlaties tussen de participantenvlakken kunnen geïnterpreteerd worden als een niet-lineare hydrodynamische reactie op ε_n en Φ_n. Hoewel een direct kwantitatieve vergelijking van meetgegevens en hydrodynamische voorspellingen gebaseerd op gelijke technieken nog niet beschikbaar is, toont de kwalitatieve vergelijking reeds dat deze nieuwe waarnemingen nieuwe grenzen zullen stellen aan de initiële toestand en de dynamische ontwikkeling van de materie die gecreëerd wordt in zware-ionenbotsingen.

Bibliography

[1] Quantum Chromodynamics, W. Greiner et al., Springer (2002).

[2] K. G. Wilson, Phys. Rev. D **10**, 2445 (1974).

[3] D. J. Gross and F. Wilczek, Phys. Rev. Lett. **30**, 1343 (1973).

[4] K. A. Olive *et al.* [Particle Data Group Collaboration], Chin. Phys. C **38**, 090001 (2014).

[5] C. L. Bennett *et al.* [WMAP Collaboration], Astrophys. J. Suppl. **208**, 20 (2013) [arXiv:1212.5225 [astro-ph.CO]].

[6] P. A. R. Ade *et al.* [Planck Collaboration], arXiv:1303.5062 [astro-ph.CO].

[7] A. Bazavov *et al.* [HotQCD Collaboration], arXiv:1407.6387 [hep-lat].

[8] J. Adams *et al.* [STAR Collaboration], Nucl. Phys. A **757**, 102 (2005) [nucl-ex/0501009].

[9] A. Andronic, P. Braun-Munzinger and J. Stachel, Phys. Lett. B **673**, 142 (2009) [Erratum-ibid. B **678**, 516 (2009)] [arXiv:0812.1186 [nucl-th]].

[10] F. Becattini and R. Fries, arXiv:0907.1031 [nucl-th].

[11] J. Cleymans and K. Redlich, Phys. Rev. Lett. **81**, 5284 (1998) [nucl-th/9808030].

[12] P. Braun-Munzinger, K. Redlich and J. Stachel, In *Hwa, R.C. (ed.) et al.: Quark gluon plasma* 491-599 [nucl-th/0304013].

[13] A. Andronic, P. Braun-Munzinger, K. Redlich and J. Stachel, Nucl. Phys. A **904-905**, 535c (2013) [arXiv:1210.7724 [nucl-th]].

[14] M. Floris, arXiv:1408.6403 [nucl-ex].

[15] C. Adler *et al.* [STAR Collaboration], Phys. Rev. Lett. **87**, 182301 (2001) [nucl-ex/0107003].

[16] C. Adler *et al.* [STAR Collaboration], Phys. Rev. C **66**, 034904 (2002)

[17] P. Huovinen, P. F. Kolb, U. W. Heinz, P. V. Ruuskanen and S. A. Voloshin, Phys. Lett. B **503**, 58 (2001) [hep-ph/0101136].

[18] P. Huovinen, P. F. Kolb, U. W. Heinz, P. V. Ruuskanen and S. A. Voloshin, Phys. Lett. B **503**, 58 (2001) [hep-ph/0101136].

[19] M. Luzum and P. Romatschke, Phys. Rev. C **78**, 034915 (2008) [Erratum-ibid. C **79**, 039903 (2009)] [arXiv:0804.4015 [nucl-th]].

[20] M. Luzum and P. Romatschke, Phys. Rev. Lett. **103**, 262302 (2009) [arXiv:0901.4588 [nucl-th]].

[21] C. Gale, S. Jeon, B. Schenke, P. Tribedy and R. Venugopalan, Phys. Rev. Lett. **110**, 012302 (2013) [arXiv:1209.6330 [nucl-th]].

[22] G. Aad *et al.* [ATLAS Collaboration], Phys. Rev. C **86**, 014907 (2012) [arXiv:1203.3087 [hep-ex]].

[23] G. Aad *et al.* [ATLAS Collaboration], JHEP **1311**, 183 (2013) [arXiv:1305.2942 [hep-ex]].

[24] S. Afanasiev *et al.* [PHENIX Collaboration], Phys. Rev. C **80**, 024909 (2009) [arXiv:0905.1070 [nucl-ex]].

[25] B. Alver *et al.* [PHOBOS Collaboration], Phys. Rev. C **81**, 034915 (2010) [arXiv:1002.0534 [nucl-ex]].

[26] B. I. Abelev *et al.* [STAR Collaboration], Phys. Rev. C **77**, 054901 (2008) [arXiv:0801.3466 [nucl-ex]].

[27] B. I. Abelev *et al.* [STAR Collaboration], Phys. Rev. C **81**, 044902 (2010) [arXiv:1001.5052 [nucl-ex]].

[28] Y. Bai,

[29] "Hot and Dense QCD Matter, Unraveling the Mysteries of the Strongly Interacting Quark-Gluon-Plasma".

[30] D. d'Enterria, arXiv:0902.2011 [nucl-ex].

[31] X. N. Wang and M. Gyulassy, Phys. Rev. Lett. **68**, 1480 (1992).

[32] M. M. Aggarwal *et al.* [WA98 Collaboration], Eur. Phys. J. C **23**, 225 (2002)

[33] A. Adare *et al.* [PHENIX Collaboration], Phys. Rev. Lett. **101**, 232301 (2008)

[34] J. Adams *et al.* [STAR Collaboration], Phys. Rev. Lett. **91**, 172302 (2003)

[35] K. Aamodt *et al.* [ALICE Collaboration], Phys. Lett. B **696**, 30 (2011)

[36] S. Chatrchyan *et al.* [CMS Collaboration], Eur. Phys. J. C **72**, 1945 (2012)

[37] A. Dainese, C. Loizides and G. Paic, Eur. Phys. J. C **38**, 461 (2005) [hep-ph/0406201].

[38] I. Vitev and M. Gyulassy, Phys. Rev. Lett. **89**, 252301 (2002) [hep-ph/0209161].

[39] C. A. Salgado and U. A. Wiedemann, Phys. Rev. D **68**, 014008 (2003) [hep-ph/0302184].

[40] N. Armesto, A. Dainese, C. A. Salgado and U. A. Wiedemann, Phys. Rev. D **71**, 054027 (2005) [hep-ph/0501225].

[41] T. Renk, H. Holopainen, R. Paatelainen and K. J. Eskola, Phys. Rev. C **84**, 014906 (2011) [arXiv:1103.5308 [hep-ph]].

[42] G. Roland, K. Safarik and P. Steinberg, Prog. Part. Nucl. Phys. **77**, 70 (2014).

[43] F.Carminati, (Ed.) *et al.* [ALICE Collaboration], J. Phys. G **G30** (2004) 1517-1763.

[44] E. V. Shuryak, Zh. Eksp. Teor. Fiz. **74** (1978) 408.

[45] Shuryak, Edward: Structure of Strongly Coupled Quark-Gluon Plasma. Stock, R. (ed.). SpringerMaterials - The Landolt-Brnstein Database (http://www.springermaterials.com). Springer-Verlag Berlin Heidelberg, 2010. DOI: $10.1007/978 - 3 - 642 - 01539 - 7_{1}9$.

[46] T. D. Lee, G. C. Wick, Phys. Rev. **D9** (1974) 2291.

[47] K. H. Ackermann *et al.* [STAR Collaboration], "Elliptic flow in Au + Au collisions at (S(NN))**(1/2) = 130 GeV," Phys. Rev. Lett. **86** (2001) 402-407.

[48] T. Hirano, N. van der Kolk, A. Bilandzic, Lect. Notes Phys. **785** (2010) 139-178. [arXiv:0808.2684 [nucl-th]].

[49] http://www.bnl.gov/bnlweb/pubaf/pr/PR_display.asp ?prID=05-38.

[50] L.D. Landau, E.M. Lifshitz: *Fluid Mechanics*, (Pergamon Press, New York, 1959), Sections 133–136.

[51] C. Eckart: Phys. Rev. **58**, 919 (1940).

[52] T. Hirano, *"Hydrodynamics and Flow"*, pages 13-14, http://tkynt2.phys.s.u-tokyo.ac.jp/∼hirano/presentation/08YITPlecture/hirano_2nd.ppt .

[53] U. W. Heinz, in 'Relativistic Heavy Ion Physics', Landolt-Boernstein New Series, I/23, edited by R. Stock (Springer Verlag, New York,2010) Chap. 5 [arXiv:0901.4355 [nucl-th]].

[54] J. D. Bjorken: Phys. Rev. D **27**, 140 (1983).

[55] P. Kovtun, D. T. Son and A. O. Starinets: Phys. Rev. Lett. **94**, 111601 (2005).

[56] A. Nakamura and S. Sakai: Phys. Rev. Lett. **94**, 072305 (2005).

[57] D. Kharzeev, K. Tuchin, JHEP **0809** (2008) 093.

[58] F. Karsch, D. Kharzeev and K. Tuchin: Phys. Lett. B **663**, 217 (2008).

[59] M. Mizutani, S. Muroya and M. Namiki: Phys. Rev. D **37**, 3033 (1988).

[60] W. A. Hiscock, L. Lindblom, Phys. Rev. **D31** (1985) 725-733.

[61] G. S. Denicol, T. Kodama, T. Koide, P. .Mota, J. Phys. G **G35** (2008) 115102.

[62] C. Cattaneo: Atti. Sem. Mat. Univ. Modena **3**, 83 (1948)

[63] http://cdsweb.cern.ch/record/1165534/files/CERN-Brochure-2009-003-Eng.pdf .

[64] CERN public pages (http://public.web.cern.ch/public/) .

[65] ALICE public pages (http://aliceinfo.cern.ch/Public/Welcome.html) .

[66] ATLAS public pages (http://atlas.ch) .

[67] CMS public pages (http://cms.web.cern.ch/cms/index.html) .

[68] LHCb public pages (http://lhcb-public.web.cern.ch/lhcb-public/) .

[69] CERN public pages (http://public.web.cern.ch/public/en/LHC/LHCf-en.html) .

[70] TOTEM public pages (http://totem.web.cern.ch/Totem/) .

[71] F. Retiere and M. A. Lisa, Phys. Rev. C **70**, 044907 (2004) [nucl-th/0312024].

[72] A. Adare *et al.* [PHENIX Collaboration], Phys. Rev. Lett. **98**, 162301 (2007)

[73] U. Heinz, C. Shen and H. -C. Song, AIP Conf. Proc. **1441**, 766 (2012)

[74] C. Adler *et al.* [STAR Collaboration], Phys. Rev. C **66**, 034904 (2002)

[75] A. M. Poskanzer and S. A. Voloshin, Phys. Rev. C **58**, 1671 (1998)

[76] A. Adare *et al.* [PHENIX Collaboration], Phys. Rev. C **85**, 064914 (2012)

[77] K. Aamodt *et al.* [ALICE Collaboration], JINST **3** (2008) S08002.

[78] G. Dellacasa *et al.* [ALICE Collaboration], “ALICE: Technical design report of the time projection chamber.”

[79] GAlessandro, (Ed.) *et al.* [ALICE Collaboration], J. Phys. G **G32** (2006) 1295-2040.

[80] G. Dellacasa *et al.* [ALICE Collaboration], “ALICE technical design report of the inner tracking system (ITS).”

[81] ALICE collaboration, ALICE Inner Tracking System (ITS): Technical Design Report, CERN-LHCC-99-012, http://edms.cern.ch/file/398932/1.

[82] ALICE Collaboration, ALICE Time-Of-Flight system (TOF): Technical Design Report, CERN-LHCC-2000-012, http://cdsweb.cern.ch/record/430132; ALICE Time-Of Flight system (TOF): addendum to the technical design report, CERN-LHCC-2002-016, http://cdsweb.cern.ch/record/545834.

[83] A. Akindinov *et al.*, Particle identification with the ALICE TOF detector at very high particle multiplicity, Eur. Phys. J. C 32 (2004) s165.

[84] PCortese *et al.* [ALICE Collaboration], "ALICE technical design report on forward detectors: FMD, T0 and V0."

[85] G. Dellacasa *et al.* [ALICE Collaboration], "ALICE technical design report of the zero degree calorimeter (ZDC)."

[86] J. Y. Ollitrault, Phys. Rev. D **46** (1992) 229.

[87] S. Voloshin and Y. Zhang, Z. Phys. C **70** (1996) 665.

[88] P. F. Kolb, Phys. Rev. **C68** (2003) 031902.

[89] S. A. Voloshin, A. M. Poskanzer, A. Tang, G. Wang, Phys. Lett. **B659** (2008) 537-541.

[90] E. Butkov, "Mathematical Physics", Addison-Wesley Series in Advanced Physics, 1968.

[91] H. Heiselberg and A. M. Levy: Phys. Rev. C **59**, 2716 (1999).

[92] H. Sorge: Phys. Rev. Lett. **82**, 2048 (1999).

[93] S. A. Voloshin and A. M. Poskanzer: Phys. Lett. B **474**, 27 (2000).

[94] R. J. Glauber, *Lectures in Theoretical Physics*, ed. WE Brittin, LG Dunham, 1:315. New York: Interscience (1959) .

[95] M. L. Miller, K. Reygers, S. J. Sanders, P. Steinberg, Ann. Rev. Nucl. Part. Sci. **57** (2007) 205-243.

[96] M. Miller and R. Snellings: arXiv:nucl-ex/0312008.

[97] Z. Qiu and U. W. Heinz, Phys. Rev. C **84** (2011) 024911 [arXiv:1104.0650 [nucl-th]].

[98] X. l. Zhu, M. Bleicher and H. Stoecker: Phys. Rev. C **72**, 064911 (2005).

[99] H. J. Drescher and Y. Nara: Phys. Rev. C **75**, 034905 (2007).

[100] R. Andrade, F. Grassi, Y. Hama, T. Kodama and O. Socolowski Jr.: Phys. Rev. Lett. **97**, 202302 (2006).

[101] W. Broniowski, P. Bozek and M. Rybczynski: Phys. Rev. C **76**, 054905 (2007).

[102] B. Alver *et al.*: Phys. Rev. C **77**, 014906 (2008).

[103] P. F. Kolb, U. W. Heinz, In *Hwa, R.C. (ed.) et al.: Quark gluon plasma* 634-714.

[104] P. F. Kolb, J. Sollfrank and U. W. Heinz: Phys. Rev. C **62**, 054909 (2000).

[105] C. Alt *et al.* [NA49 Collaboration]: Phys. Rev. C **68**, 034903 (2003).

[106] N. Borghini, P. M. Dinh, J. -Y. Ollitrault, Phys. Rev. **C63** (2001) 054906.

[107] N. Borghini, P. M. Dinh, J. -Y. Ollitrault, Phys. Rev. **C64** (2001) 054901.

[108] N. Borghini, P. M. Dinh, J. -Y. Ollitrault, [nucl-ex/0110016].

[109] C. Adler *et al.* [STAR Collaboration], Phys. Rev. C **66**, 034904 (2002).

[110] A. M. Poskanzer, S. A. Voloshin, Phys. Rev. **C58** (1998) 1671-1678. [nucl-ex/9805001].

[111] A. Bilandzic, R. Snellings, S. Voloshin, Phys. Rev. **C83** (2011) 044913.

[112] R. S. Bhalerao, N. Borghini, J. Y. Ollitrault, Phys. Lett. **B580** (2004) 157-162.

[113] R. S. Bhalerao, N. Borghini and J. Y. Ollitrault Nucl. Phys. A **727** (2003) 373.

[114] R. S. Bhalerao, N. Borghini and J. Y. Ollitrault J. Phys. G **30** (2004) S1213.

[115] A. Bilandzic, N. van der Kolk, J. -Y. Ollitrault, R. Snellings, Phys. Rev. **C83** (2011) 014909.

[116] S. Wang, Y. Z. Jiang, Y. M. Liu, D. Keane, D. Beavis, S. Y. Chu, S. Y. Fung, M. Vient *et al.*, Phys. Rev. **C44** (1991) 1091-1095.

[117] S. A. Voloshin, arXiv:nucl-th/0606022.

[118] R. Kubo, "Generalized Cumulant Expansion Method," Journal of the Physical Society of Japan, Vol. 17, No. 7, (1962).

[119] G. Cowan, "Statistical data analysis," *Oxford, UK: Clarendon (1998) 197 p*.

[120] S. Brandt, "Statistical and Computational Methods in Data Analysis," *Amsterdam 1976, 414p*.

[121] Aamodt *et al.* [The ALICE Collaboration], Phys. Rev. Lett. **105** (2010) 252302.

[122] K. Aamodt *et al.* [ALICE Collaboration], Phys. Rev. Lett. **107**, 032301 (2011) [arXiv:1105.3865 [nucl-ex]].

[123] B. Abelev *et al.* [ALICE Collaboration], Phys. Lett. B **719**, 18 (2013) [arXiv:1205.5761 [nucl-ex]].

[124] J. Adams *et al.* [STAR Collaboration], Phys. Rev. Lett. **92**, 062301 (2004).

[125] N. Borghini, P. M. Dinh and J. Y. Ollitrault, Phys. Rev. C **66**, 014905 (2002).

[126] I. Selyuzhenkov and S. A. Voloshin Phys. Rev. C **77** (2008) 034904 .

[127] S. A. Voloshin, A. M. Poskanzer, and R. Snellings, in Landolt-Boernstein, Relativistic Heavy Ion Physics Vol. 1/23 (Springer-Verlag, Berlin, 2010), pp 554.

[128] A. Andronic *et al.* [FOPI Collaboration], Phys. Lett. **B612** (2005) 173-180.

[129] "ALICE Offline pages", http://aliweb.cern.ch/Offline/ .

[130] "ROOT System", http://root.cern.ch/ .

[131] M. Ballintijn, R. Brun, F. Rademakers and G. Roland "Distributed Parallel Analysis Framework with PROOF," Proc. TUCT004 (2004) .

[132] H-U. Bengtsson, T. Sjostrand (1987) Comput. Phys. Commun. **46** 43 (http://www.thep.lu.se/ torbjorn/Pythia.html) .

[133] X-N. Wang, M. Gyulassy (1991) Phys. Rev. D 44 3501 , M. Gyulassy, X-N. Wang (1994) Comput. Phys. Commun. 83 30731 , (http://www-nsdth.lbl.gov/ xnwang/hijing/) .

[134] R. Brun, F. Bruyant, M. Maire, A.C. McPherson, P. Zanarini (1985) GEANT3 User Guide CERN Data Handling Division DD/EE/84-1 (http://wwwinfo.cern.ch/asdoc/geantold/GEANTMAIN.html) .

[135] J. Conrad *et al* "Minimum bias triggers in proton-proton collisions with VZERO and pixel detectors" ALICE Internal Note ALICE-INT-2005-025, http://cdsweb.cern.ch/record/960438 .

[136] A. T. f. Collaboration, arXiv:1107.1973 [nucl-ex].

[137] B. Abelev *et al.* [The ALICE Collaboration], Phys. Rev. Lett. **105** (2010) 252301 .

[138] M. Krzewicki, PhD thesis, *"Anisotropic flow measurements in ALICE at the Large Hadron Collider,"* Nikhef and Utrecht University, 2012.

[139] A. Bilandzic, PhD thesis, *"Anisotropic flow of identifed hadrons in heavy-ion collisions at the LHC — from detector alignment and calibration to measurement,"* Nikhef and Utrecht University, 2011.

[140] A. Kisiel, T. Taluc, W. Broniowski and W. Florkowski, Comput. Phys. Commun. **174**, 669 (2006) .

[141] P. Bozek, M. Chojnacki, W. Florkowski and B. Tomasik, Phys. Lett. B **694**, 238 (2010) .

[142] R. S. Bhalerao, M. Luzum and J. Y. Ollitrault, [arXiv:1104.4740 [nucl-th]].

[143] Y. Bai, Ph.D. thesis, Nikhef and Utrecht University, 2007.

[144] B. I. Abelev *et al.* [STAR Collaboration], Phys. Rev. C **77** (2008) 054901 .

[145] B. Schenke, S. Jeon, C. Gale, [arXiv:1102.0575 [hep-ph]].

[146] G. Kestin, U. W. Heinz, Eur. Phys. J. **C61** (2009) 545-552.

[147] H. Masui, J-Y. Ollitrault, R. Snellings, A. Tang, Nucl. Phys. **A830** (2009) 463C-466C.

[148] M. Luzum, P. Romatschke, Phys. Rev. Lett. **103** (2009) 262302.

[149] T. Hirano, P. Huovinen, Y. Nara, Phys. Rev. **C83** (2011) 021902.

[150] T. Hirano, U. W. Heinz, D. Kharzeev, R. Lacey, Y. Nara, Phys. Lett. **B636** (2006) 299-304.

[151] H. -J. Drescher, A. Dumitru, J. -Y. Ollitrault, [arXiv:0706.1707 [nucl-th]].

[152] P. Billor, "Track Fitting with Multiple Scattering: A New Method," NIM **A225**, 352-366 (1984) .

[153] M. Luzum and J. -Y. Ollitrault, Phys. Rev. C **87**, 044907 (2013) [arXiv:1209.2323 [nucl-ex]].

[154] J. -Y. Ollitrault, A. M. Poskanzer and S. A. Voloshin, Phys. Rev. C **80**, 014904 (2009) [arXiv:0904.2315 [nucl-ex]].

[155] B. Alver, B. B. Back, M. D. Baker, M. Ballintijn, D. S. Barton, R. R. Betts, R. Bindel and W. Busza *et al.*, Phys. Rev. C **77**, 014906 (2008) [arXiv:0711.3724 [nucl-ex]].

[156] C. Adler *et al.* [STAR Collaboration], Phys. Rev. C **66**, 034904 (2002) [nucl-ex/0206001].

[157] R. S. Bhalerao, J. -Y. Ollitrault and S. Pal, arXiv:1307.0980 [nucl-th].

[158] Y. Zhou "QC with eta gap"

[159] R. Snellings, New J. Phys. **13**, 055008 (2011) [arXiv:1102.3010 [nucl-ex]].

[160] G. -L. Ma and X. -N. Wang, Phys. Rev. Lett. **106**, 162301 (2011) [arXiv:1011.5249 [nucl-th]].

[161] B. Alver and G. Roland, Phys. Rev. C **81**, 054905 (2010) [Erratum-ibid. C **82**, 039903 (2010)] [arXiv:1003.0194 [nucl-th]].

[162] P. Kovtun, D. T. Son and A. O. Starinets, Phys. Rev. Lett. **94**, 111601 (2005) [hep-th/0405231].

[163] B. Alver *et al.* [PHOBOS Collaboration], Phys. Rev. Lett. **98**, 242302 (2007) [nucl-ex/0610037].

[164] R. S. Bhalerao, J. -Y. Ollitrault and S. Pal, Phys. Rev. C **88**, 024909 (2013) [arXiv:1307.0980 [nucl-th]].

[165] H. Masui and A. Schmah, arXiv:1212.3650 [nucl-ex].

[166] N. Borghini and J. Y. Ollitrault, Phys. Rev. C **70**, 064905 (2004)

[167] F. Retiere and M. A. Lisa, Phys. Rev. C **70**, 044907 (2004)

[168] B. B. Abelev *et al.* [ALICE Collaboration], arXiv:1307.6796 [nucl-ex].

[169] K. H. Ackermann *et al.* [STAR Collaboration], Phys. Rev. Lett. **86**, 402 (2001) [nucl-ex/0009011].

[170] J. -Y. Ollitrault, Phys. Rev. D **46**, 229 (1992).

[171] B. H. Alver, C. Gombeaud, M. Luzum and J. -Y. Ollitrault, Phys. Rev. C **82**, 034913 (2010)

[172] ALICE Collaboration, Phys. Rev. Lett. **00**, (2014)

[173] K. Aamodt *et al.* [ALICE Collaboration], Phys. Lett. B **708**, 249 (2012)

[174] J. Adams *et al.* [STAR Collaboration], Nucl. Phys. A **757**, 102 (2005) [nucl-ex/0501009].

[175] I. Arsene *et al.* [BRAHMS Collaboration], Nucl. Phys. A **757**, 1 (2005) [nucl-ex/0410020].

[176] K. Adcox *et al.* [PHENIX Collaboration], Nucl. Phys. A **757**, 184 (2005) [nucl-ex/0410003].

[177] A. Shor, Phys. Rev. Lett. **54**, 1122 (1985).

[178] S. Okubo, Phys. Lett. **5**, 1975 (1963); G. Zweig, CERN Report No.8419/TH412 (1964); J. Iizuka, Prog. Theor. Phys. Suppl. 37, 38 (1966).

[179] H. Song, S. Bass and U. W. Heinz, Phys. Rev. C **89**, 034919 (2014) [arXiv:1311.0157 [nucl-th]].

[180] P. Huovinen, P. F. Kolb, U. W. Heinz, P. V. Ruuskanen and S. A. Voloshin, Phys. Lett. B **503**, 58 (2001) [hep-ph/0101136].

[181] D. Teaney, J. Lauret and E. V. Shuryak, Phys. Rev. Lett. **86**, 4783 (2001) [nucl-th/0011058].

[182] B. Abelev *et al.* [ALICE Collaboration], Phys. Rev. C **88**, 044910 (2013) [arXiv:1303.0737 [hep-ex]].

[183] B. B. Abelev *et al.* [ALICE Collaboration], arXiv:1404.0495 [nucl-ex].

[184] U. Heinz and R. Snellings, Ann. Rev. Nucl. Part. Sci. **63**, 123 (2013) [arXiv:1301.2826 [nucl-th]].

[185] J. Adams *et al.* [STAR Collaboration], Phys. Rev. Lett. **92**, 052302 (2004) [nucl-ex/0306007].

[186] P. Kovtun, D. T. Son and A. O. Starinets, Phys. Rev. Lett. **94**, 111601 (2005) [hep-th/0405231].

[187] S. Afanasiev *et al.* [PHENIX Collaboration], Phys. Rev. Lett. **99**, 052301 (2007) [nucl-ex/0703024 [NUCL-EX]].

[188] S. A. Voloshin, Phys. Rev. C **55**, 1630 (1997) [nucl-th/9611038].

[189] P. Huovinen, P. F. Kolb, U. W. Heinz, P. V. Ruuskanen and S. A. Voloshin, Phys. Lett. B **503**, 58 (2001) [hep-ph/0101136].

[190] A. Adare *et al.* [PHENIX Collaboration], Phys. Rev. C **85**, 064914 (2012) [arXiv:1203.2644 [nucl-ex]].

[191] J. Adams *et al.* [STAR Collaboration], Phys. Rev. Lett. **95**, 122301 (2005) [nucl-ex/0504022].

[192] B. Abelev *et al.* [ALICE Collaboration], Phys. Rev. Lett. **110**, 032301 (2013) [arXiv:1210.3615 [nucl-ex]].

[193] D. Molnar and S. A. Voloshin, Phys. Rev. Lett. **91**, 092301 (2003) [nucl-th/0302014].

[194] J. Xu and C. M. Ko, Phys. Rev. C **83**, 034904 (2011) [arXiv:1101.2231 [nucl-th]].

[195] Y. Zhou [ALICE Collaboration], Acta Phys. Polon. Supp. **5**, 407 (2012) [arXiv:1112.1256 [nucl-ex]].

[196] M. L. Miller, K. Reygers, S. J. Sanders and P. Steinberg, Ann. Rev. Nucl. Part. Sci. **57**, 205 (2007) [nucl-ex/0701025].

[197] H. -J. Drescher and Y. Nara, Phys. Rev. C **75**, 034905 (2007) [nucl-th/0611017].

[198] B. Alver *et al.* [PHOBOS Collaboration], Phys. Rev. C **81**, 034915 (2010) [arXiv:1002.0534 [nucl-ex]].

[199] G. Agakishiev *et al.* [STAR Collaboration], Phys. Rev. C **86**, 014904 (2012) [arXiv:1111.5637 [nucl-ex]].

[200] A. Bilandzic [ALICE Collaboration], Nucl. Phys. A **904-905**, 515c (2013) [arXiv:1210.6222 [nucl-ex]].

[201] A. Bilandzic [ALICE Collaboration], J. Phys. G **38**, 124052 (2011) [arXiv:1106.6209 [nucl-ex]].

[202] R. S. Bhalerao, J. -Y. Ollitrault and S. Pal, Phys. Rev. C **88**, 024909 (2013) [arXiv:1307.0980 [nucl-th]].

[203] D. Teaney and L. Yan, Phys. Rev. C **86**, 044908 (2012) [arXiv:1206.1905 [nucl-th]].

[204] Z. Qiu and U. Heinz, Phys. Lett. B **717**, 261 (2012) [arXiv:1208.1200 [nucl-th]].

[205] H. Niemi, G. S. Denicol, H. Holopainen and P. Huovinen, Phys. Rev. C **87**, 054901 (2013) [arXiv:1212.1008 [nucl-th]].

[206] P. Huo, J. Jia and S. Mohapatra, arXiv:1311.7091 [nucl-ex].

[207] H. Niemi, G. S. Denicol, H. Holopainen and P. Huovinen, Phys. Rev. C **87**, 054901 (2013) [arXiv:1212.1008 [nucl-th]].

[208] B. Abelev *et al.* [ALICE Collaboration], Phys. Rev. C **88**, no. 4, 044909 (2013) [arXiv:1301.4361 [nucl-ex]].

[209] C. Loizides, f. t. A. collaboration, “Charged-particle multiplicity and transverse energy in Pb-Pb collisions at sqrt(snn) = 2.76 TeV with ALICE,” [arXiv:1106.6324 [nucl-ex]].

[210] Krein, M.G. (1945), ”On an extrapolation problem due to Kolmogorov”, Doklady Akademii Nauk SSSR 46: 306309.

[211] J. Stoyanov, Section 3 in “Determinacy of distributions by their moments”, proceedings for *International Conference on Mathematics & Statistical Modelling*, 2006.

[212] J. Jia and S. Mohapatra, Eur. Phys. J. C **73**, 2510 (2013) [arXiv:1203.5095 [nucl-th]].

[213] L. Xu, L. Yi, D. Kikola, J. Konzer, F. Wang and W. Xie, Phys. Rev. C **86**, 024910 (2012) [arXiv:1204.2815 [nucl-ex]].

[214] F. G. Gardim, F. Grassi, M. Luzum and J. -Y. Ollitrault, Phys. Rev. C **87**, no. 3, 031901 (2013) [arXiv:1211.0989 [nucl-th]].

[215] U. Heinz, Z. Qiu and C. Shen, Phys. Rev. C **87**, no. 3, 034913 (2013) [arXiv:1302.3535 [nucl-th]].

[216] B. Abelev *et al.* [ALICE Collaboration], Phys. Lett. B **719**, 29 (2013) [arXiv:1212.2001 [nucl-ex]].

[217] S. Chatrchyan *et al.* [CMS Collaboration], Phys. Lett. B **724**, 213 (2013) [arXiv:1305.0609 [nucl-ex]].

[218] G. Aad *et al.* [ATLAS Collaboration], Phys. Lett. B **725**, 60 (2013) [arXiv:1303.2084 [hep-ex]].

[219] B. B. Abelev *et al.* [ALICE Collaboration], arXiv:1406.2474 [nucl-ex].

[220] H. Niemi, K. J. Eskola and P. V. Ruuskanen, Phys. Rev. C **79**, 024903 (2009) [arXiv:0806.1116 [hep-ph]].

[221] G. Aad *et al.* [ATLAS Collaboration], arXiv:1403.0489 [hep-ex].

[222] R. S. Bhalerao, J. Y. Ollitrault and S. Pal, Phys. Rev. C **88**, 024909 (2013) [arXiv:1307.0980 [nucl-th]].

[223] L. Yan, J. Y. Ollitrault and A. M. Poskanzer, Phys. Rev. C **90**, 024903 (2014) [arXiv:1405.6595 [nucl-th]].

[224] L. Yan and J. Y. Ollitrault, Phys. Rev. Lett. **112**, 082301 (2014) [arXiv:1312.6555 [nucl-th]].

Appendix A

Mixed harmonic correlations

A.1 Participant plane correlations in the final state via mixed-harmonic correlations

The initial participant plane correlations have been investigated in Section 6.3.1, while the final state participant plane correlations are measured via SP method which have been discussed in Section 6.3.2. It was realised that we can not simply cancel the v_n or v_m contributions from SP method, due to the correlations of v_n and v_m. Alternatively, the participant planes can be still investigated by using multi-particle correlations technique [142]. This is a direct calculation which taking the self-correlation (auto-correlation) into account and no need to apply any pseudorapidity gap but using multi-particle correlations technique, it is defined as following:

$$\langle \cos(c_1\varphi_1 + c_2\varphi_2 + \cdots + c_l\varphi_l) \rangle = \langle v_{|c_1|} v_{|c_2|} \cdots v_{|c_l|} \cos(c_1\Psi_{|c_1|} + c_2\Psi_{|c_2|} + \cdots + c_l\Psi_{|c_l|}) \rangle \tag{A.1}$$

where c_1, $\cdots$, c_l are integers, φ_1, $\cdots$, φ_l are azimuthal angles of particles belonging to the same event, and the angular brackets denote average over multiplets of particles and events in a centrality interval. The only measurable correlations have azimuthal symmetry: $c_1 + c_2 + \cdots + c_l = 0$. These multi-particle correlations can be evaluated via mixed-harmonic multi-particle cumulant method [138, 200].

2-Plane Correlations

For the correlations of different order participant planes, the simplest case is the 2-plane correlations via 3-particles cumulant. For the n^{th} and m^{th} order participant plane correlations (when $m = 2n$) in the final state, the (Ψ_n,Ψ_m) correlations, we follow Eq. (A.1).

$$\langle \cos\left[n\left(2\phi_1 - \phi_2 - \phi_3\right)\right] \rangle = \langle v_{2n} v_n^2 \cos\left[n(2\Psi_{2n} - 2\Psi_n)\right] \rangle \tag{A.2}$$

This observable can be directly calculated in terms of a three-particle cumulant $\mathrm{QC}\{3\}_{\mathrm{2n,-n,-n}}$ defined as:

$$\begin{aligned}\langle\cos[n(2\phi_1-\phi_2-\phi_3)]\rangle &= \mathrm{QC}\{3\}_{\mathrm{2n,-n,-n}} \\ &= [Q_{2n}Q_n^*Q_n^* - 2\cdot|Q_n|^2 - |Q_{2n}|^2 + 2M]/ \\ &\quad [M(M-1)(M-2)].\end{aligned} \tag{A.3}$$

where Q is the flow-vector and M is the multiplicity.

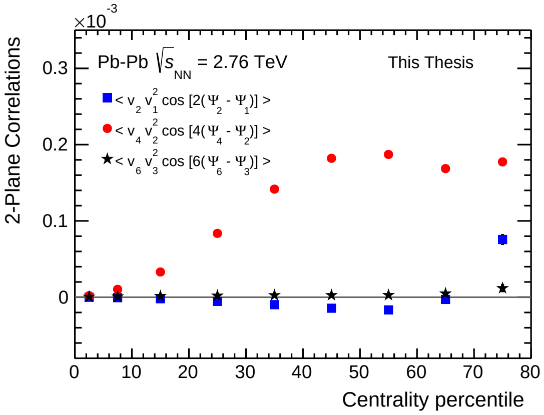

Figure A.1: Centrality dependence of 2-plane correlations measured by ALICE.

Inserting $n = 1, 2, 3$ into Eq. (A.1), the correlations of (Ψ_2,Ψ_1), (Ψ_4,Ψ_2) and (Ψ_6,Ψ_3) can be evaluated via:

$$\langle\cos(2\phi_1-\phi_2-\phi_3)\rangle = \langle v_2 v_1^2\cos(2\Psi_2-2\Psi_1)\rangle \tag{A.4}$$

$$\langle\cos(4\phi_1-2\phi_2-2\phi_3)\rangle = \langle v_4 v_2^2\cos(4\Psi_4-4\Psi_2)\rangle \tag{A.5}$$

$$\langle\cos(6\phi_1-3\phi_2-3\phi_3)\rangle = \langle v_6 v_3^2\langle\cos(6\Psi_6-6\Psi_3)\rangle \tag{A.6}$$

We find in Fig. A.1 that the (Ψ_4, Ψ_2) correlation measured via $\langle v_4 v_2^2\cos[4(\Psi_4-\Psi_2)]\rangle$ shows a positive sign and increases with centrality. Since both v_2 and v_4 are positive, the positive $\langle v_4 v_2^2\cos[4(\Psi_4-\Psi_2)]\rangle$ suggests positive correlations of (Ψ_4, Ψ_2). In contrast, the initial (Φ_4, Φ_2) correlation shown in Fig. 6.22 has a negative sign and decreases with increasing centrality from MC-Glauber calculations. Figure A.1 also shows that 6th− and 3rd−order participant planes correlations in the final state (Ψ_6, Ψ_3) are consistent with 0. This is different from the expectation from MC-Glauber model presented in Fig. 6.22, where the initial 6th− and 3rd−order participant planes are anti-correlated (negative). Similar results which also observed from AMPT calculations presented in Fig. A.2.

At the same time, Fig. A.1 shows the centrality dependence of (Ψ_2, Ψ_1) correlation measured via $\langle v_2 v_1^2\cos[2(\Psi_2-\Psi_1)]\rangle$. This result has a negative sign from central to 60-70% centrality classes, with a dramatic sign change appears in most peripheral collisions.

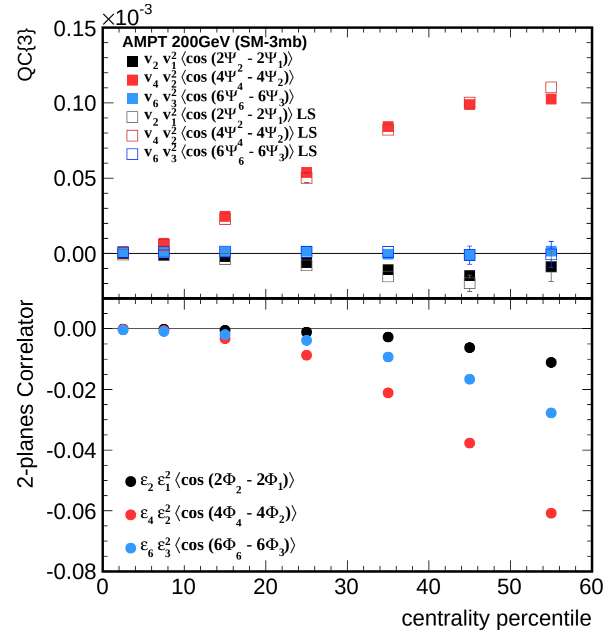

Figure A.2: Centrality dependence of 2-plane correlations in initial state from AMPT model at $\sqrt{s_{\rm NN}} = 200$ GeV.

However, the initial (Φ_1, Φ_2) correlation exhibits a negative sign for all centrality classes in initial state (from MC-Glauber model).

Considering the initial anisotropy ε_n and the final anisotropic flow v_n have the same sign (both are positive), there are three possible explanations for the different sign of participant plane correlations in the initial state and final state. Either the sign of the cosine component in the right hand side of Eq. (refeq:2pc) changes during the system evolution; or the sign of $(\Phi_4,\ \Phi_2)$ correlations calculated in MC-Glauber model is wrong, or the non-flow effects might bias the particle plane correlations measurements in the final state.

In order to check these explanations, the transport model AMPT, which provides the information of both initial state and final state, was utilized to investigate the connection between initial and final state participant plane correlations within one framework. The initial $(\Phi_n,\ \Phi_{2n})$ correlations are studied via $\langle \varepsilon_n \varepsilon_2 n \cos\left[2n\left(\Phi_2 n - \Phi_n\right)\right]\rangle$ which are presented in Fig. A.2 (bottom). Negative $(\Phi_n,\ \Phi_{2n})$ correlations has been observed for the presented centrality classes, which agrees the MC-Glauber calculations presented in Fig. 6.22. Meanwhile the $(\Psi_n,\ \Psi_{2n})$ correlations in the final state are studied via calculations of $\mathrm{QC}\{3\}_{\rm 2n,-n,-n}$. We observe positive $(\Psi_2,\ \Psi_4)$ correlations shown in Fig. A.2 (top), which is in agreement with the experimental measurements presented in Fig A.1. There is a clear sign change of 4$^{\rm th}$ order and 2$^{\rm nd}$ order participant planes correlations during the collision system evolution in AMPT model (negative in the initial state whereas positive in the final state). Such sign changes of 4^{th} order and 2^{nd} order participant planes correlations was also confirmed by hydrodynamic calculations [204]. To test potential influence from non-flow effects, the results from like-sign particles (i.e. open markers) are compared to the points from the charge independent analysis (i.e. filled markers). The comparison indicates that for all centralities there is little if no difference between the open and the full markers. This in turns can be interpreted as little if no influence of short-range non-flow effects to the participant plane correlations in the final state. The sign change of the participant plane correlations could not be explained by non-flow effects solely.

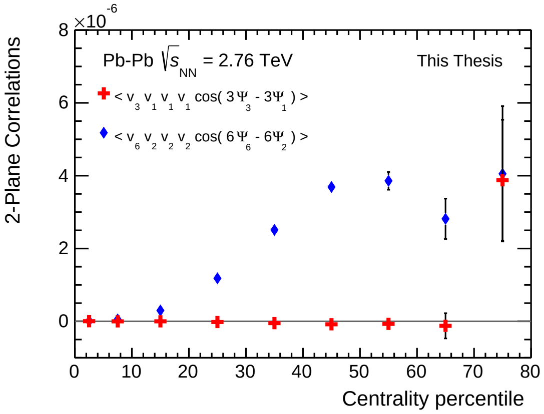

Figure A.3: Centrality dependence of 2-plane correlations using 4-particle correlations measured by ALICE.

Therefore, the study based on AMPT model suggests that the sign changing of cosine component, instead of wrong estimation of initial participant plane correlations in MC-Glauber model or non-flow effects, is responsible for the different sign of 2^nd and 4^th order participant plane correlations in the initial state and final state. The 1^{st} order and 2^{nd} order participant plane correlations, and 3^{rd} order and 6^{th} order participant plane correlations, in both initial state and final state of AMPT model, are studied in Fig. A.2. The calculations in the initial state of AMPT model agrees MC-Glauber calculations presented in Fig. 6.22 while the final state calculations qualitatively reproduce the measurements of participant plane correlations in experiments. The initial participant plane Φ_n, and final participant plane Ψ_n, might not be the same. The assumption $\Phi_n = \Psi_n$ in the 'participant plane flow v_n' calculations which correlate the particle azimuthal angle with respect to the initial participant plane presented in [160, 161] can be thus questioned.

The $\text{QC}\{3\}_{2n,-n,-n}$ are the simplest 2-plane correlations, using 3-particle cumulants. In addition, the (Ψ_n, Ψ_{3n}) correlation could be evaluated with 4-particle cumulant $\text{QC}_{3n,-n,-n,-n}$ via:

$$\langle \cos\left[n(3\varphi_1 - \varphi_2 - \varphi_3 - \varphi_4)\right]\rangle = \langle v_{3n} v_n^3 \cos\left[n(3\Psi_{3n} - 3\Psi_n)\right] . \tag{A.7}$$

In the case $n = 1$, the QC$\{3\}_{3,-1,-1,-1}$ measures the correlations between Ψ_1 and Ψ_3; the QC$\{3\}_{6,-2,-2,-2}$ probes the (Ψ_2, Ψ_6) correlations when $n = 2$.

Multi-Plane Correlations

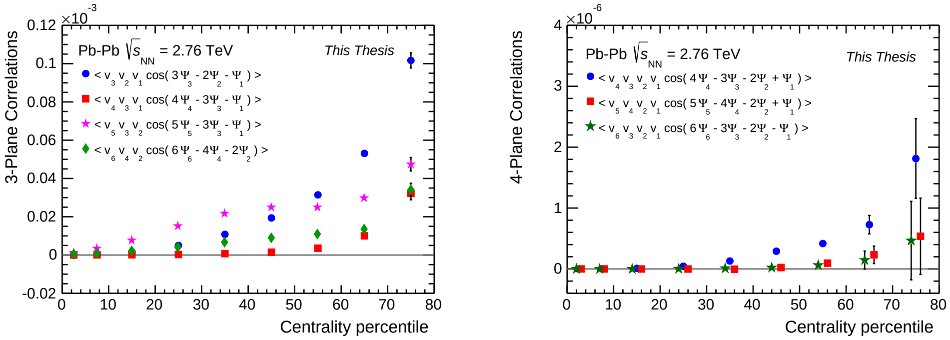

Figure A.4: Centrality dependence of 3-plane (Left) and 4-plane (Right) correlations measured by ALICE (Right).

Following Eq. (A.1), not only 2-plane but also 3-plane correlations in the final state could be measured via mixed harmonic correlations using at least 3-particle correlations:

$$\langle \cos\left[(n_1+n_2)\varphi_1 - n_1\varphi_2 - n_2\varphi_3\right]\rangle = \langle v_{n_1} v_{n_2} v_{n_1+n_2} \cos\left[(n_1+n_2)\Psi_{n_1+n_2} - n_1\Psi_{n_1} - n_2\Psi_{n_2}\right]\rangle \tag{A.8}$$

The centrality dependence of 3-plane correlations are presented in Fig. A.4. Opposite signs for all 3-plane correlations in initial state and final state are observed. In contrast, 4-plane correlations in the initial state and final state show the same sigh.

Although using mixed harmonic correlations method can not quantify the strength of the essential correlations of participant planes, however, the results will not be biased by the correlations of v_n and v_m in an uncontrolled way. Thus, it is suggested to apply mixed harmonic correlations in hydrodynamic calculations, which have described the magnitudes of v_n (for 2<n< 6) nicely.

Appendix B

SC in AMPT

B.1 Standard Candles in AMPT model

Considering the AMPT model can quantitatively describe flow measurements at the LHC [194,195] and generate reasonable centrality dependence of SC measurements, we further investigate the SC with various scenarios of AMPT model: (a) 3 mb; (b) 10 mb; (c) 10 mb, no rescattering [1]. A similar centrality dependence of $SC_{4,2,-4,-2}$ and $SC_{3,2,-3,-2}$ are found for all three scenarios at the RHIC energy, see Fig. **??**. It was shown in [**?**] that the relative flow fluctuations of v_2 do not depend on the partonic interactions and only relate to the initial eccentricity fluctuations. Therefore, the expectation is that $SC_{4,2,-4,-2}$ and $SC_{3,2,-3,-2}$ do not depend on the magnitudes of v_2 or v_4 (which depend on both partonic interactions and hadronic interactions), but depend only on the initial correlations of event-by-event fluctuations of ε_2 and ε_4. Thus, both $SC_{4,2,-4,-2}$ and $SC_{3,2,-3,-2}$ remain the same for different configurations, since the initial state was kept the same each time. However, we find that when the partonic cross section is decreasing from 10 mb (lower shear viscosity, see [194]) to 3 mb (higher shear viscosity), the strength of $SC_{4,2,-4,-2}$ decreases. Additionally, the '10mb, no rescattering' setup seems to give slightly smaller magnitudes of $SC_{4,2,-4,-2}$ and $SC_{3,2,-3,-2}$.

---

[1] details of AMPT model and various scenarios could be found in Appendix **??**

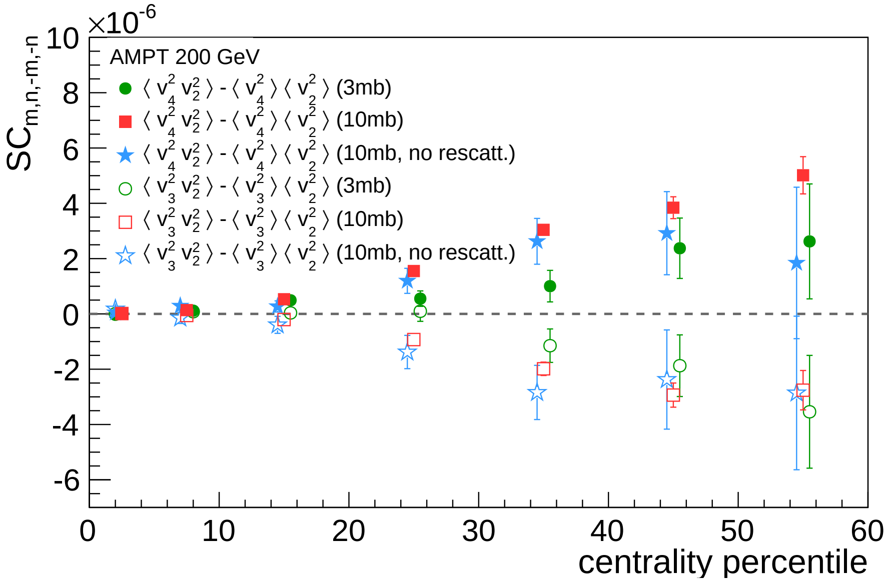

Figure B.1: (Left) Centrality dependence of $SC_{m,n,-m,-n}$ in AMPT model with various scenarios.

Appendix C

Curriculum Vitae

Personal Information

DATE OF BIRTH:	24 July 1985
GENDER:	Male
NATIONALITY:	Chinese
CURRENT POSITION:	Postdoctoral Researcher at Niels Bohr Institute (NBI)
ADDRESS:	Blegdamsvej 17, 2100 Copenhagen Ø, Denmark
EMAIL1:	you.zhou@cern.ch
EMAIL2:	yzhou.cern@gmail.com

Education

2010.8 - 2014.11	PhD Researcher at National Institute for Subatomic Physics (Nikhef) and Institute of Subatomic Physics, Utrecht University. PROMOTOR: Prof. Dr. Raimond Snellings SUPERVISOR: Dr. Panos Christakoglou PhD THESIS TITLE: *"Anisotropic Flow and Flow Fluctuations at the Large Hadron Collider"*
2007.9 - 2010.7	MASTERS IN PHYSICS, Central China Normal University, China. SUPERVISORS: Prof. Dr. Feng Liu Master THESIS TITLE: *"Charged Particle ratio fluctuation and higher moments of net-baryon distribution in relativistic heavy ion collisions"*

Academic activity

2015.1 - now: Coordination of Physics Analysis Group FLOW (FLOW-PAG), the ALICE Collaboration

2015.9 - now: Co-supervisor of one PhD student at Niels Bohr Institute.

2013: Daily co-supervisor of two summer school students at CERN.

2011-2013: Co-supervisor of two master students at Utrecht University.

2011-2013: Co-supervisor of two bachelor students at Utrecht University.

2011-2013: Teaching Assistant for Subatomic Physics course at Utrecht University.

2011: Daily supervisor of one summer school student at Nikhef.

Research visits

Oct. 2015 - Oct. 2015: Academic Visitor, Institute of Theoretical Physics, Peking University, China, P.R.China

Nov. 2014 - Dec. 2014: Academic Visitor, Institute of Theoretical Physics, Peking University, China, P.R.China

Jan. 2011 - present: ALICE Collaboration, CERN, Geneva, Switzerland (half year stationed at CERN).

Conferences/Invited Talks and Posters

1. Measurements of Correlations of Anisotropic Flow Harmonics in Pb–Pb Collisions with ALICE, You Zhou on behalf of the ALICE Collaboration, **International Conference on Ultra-relativistic Nucleus-Nucleus Collisions (Quark Matter 2015)** - Kobe, Japan.
2. Overview of Anisotropic Flow Measurements from ALICE, You Zhou on behalf of the ALICE Collaboration, **12th International Conference on Nucleus-Nucleus Collisions (NN2015)** - Catania, Italy.
3. Anisotropic Flow: probe of the perfect liquid, You Zhou, invited seminar at School of Mathematics and Physics, China University of Geosciences - Wuhan, P.R.China.
4. Collective Expansion at the LHC: Anisotropic flow and flow fluctuations, You Zhou, invited seminar at Institute of Particle Physics, Central China Normal University - Wuhan, P.R.China.

5. Anisotropic Flow Measurements at the LHC, You Zhou, invited seminar at Institute of Theoretical Physics, Peking University - Beijing, P.R.China.
6. Searches for p_{T} dependent fluctuations of flow angle and magnitude in Pb–Pb and p–Pb collisions, You Zhou on behalf of the ALICE Collaboration, **International Conference on Ultra-relativistic Nucleus-Nucleus Collisions (Quark Matter 2014)** - Darmstadt, Germany.
7. Event Plane Correlations, You Zhou, invited talk at ALICE Physics Club Seminar - CERN, Switzerland.
8. Anisotropic flow of identified particles in Pb–Pb collisions at 2.76 TeV with the ALICE detector, You Zhou on behalf of the ALICE Collaboration, **International Conference on Strangeness in Quark Matter (SQM2013)** - Birmingham, United Kingdom.
9. Anisotropic flow of identified particles in $\sqrt{s_{\mathrm{NN}}} = 2.76$ TeV, You Zhou on behalf of the ALICE collaboration, **Dutch National High Energy Physics Conference (Nederlandse Natuurkundige Vereniging 2012)** - Lunteren, the Netherlands.
10. Azimuthal correlations in Pb–Pb and pp collisions measured by the ALICE detector, You Zhou on behalf of the ALICE Collaboration, **Critical point and onset of deconfinement (CPOD2011)** - Wuhan, China.
11. Anisotropic flow at $\sqrt{s_{\mathrm{NN}}} = 200$ GeV in Au+Au collisions in AMPT model, Kai Xiao, You Zhou et. al., **Critical point and onset of deconfinement (CPOD2011)** - Wuhan, China.
12. Higher harmonic anisotropic flow measurements of charged particles at 2.76 TeV with the ALICE detector, You Zhou on behalf of the ALICE Collaboration, **International Conference on Strangeness in Quark Matter (SQM2011)** - Krakow, Poland.

Poster Presentations

1. Investigation of collective behaviors in pp and p-Pb collisions at the LHC energies, Xiangrong Zhu, You Zhou, Pengfei Li and Huichao Song, **International Conference on Ultra-relativistic Nucleus-Nucleus Collisions (Quark Matter 2015)** - Kobe, Japan.
2. Hadronic “flow” in p-Pb collisions at the Large Hadron Collider? You Zhou, Xiangrong Zhu, Pengfei Li and Huichao Song, **12th International Conference on Nucleus-Nucleus Collisions (NN2015)** - Catania, Italy.
3. Generic equations for anisotropic flow analysis with multi-particle azimuthal correlations, A. Bilandzic, C. Christensen, K. Gulbrandsen, A. Hansen and Y. Zhou, **International Conference on Ultra-relativistic Nucleus-Nucleus Collisions (Quark Matter 2014)** - Darmstadt, Germany.

4. Anisotropic flow of ϕ meson in Pb–Pb collisions at $\sqrt{s} = 2.76$ TeV with the ALICE detector, You Zhou on behalf of the ALICE Collaboration, **International Conference on Ultra-relativistic Nucleus-Nucleus Collisions (Quark Matter 2012)** - Washington DC, USA.

Publications (in past five years)

ALICE Publications

Being a member of the ALICE collaboration since January 2011, I have co-authored above 100 ALICE publications. The following are the ALICE publications of which I am one of the the primary authors:

1. K. Aamodt et al. [ALICE Collaboration], *Higher Harmonic Anisotropic Flow Measurements of Charged Particles in Pb-Pb Collisions at* $\sqrt{s_{\rm NN}} = 2.76$ *TeV*, Phys. Rev. Lett. 107, 032301 (2011) [cited by $\geq$ 310 records].
2. B. Abelev et al. [ALICE Collaboration], *Elliptic flow of identified hadrons in Pb–Pb collisions at* $\sqrt{s_{\rm NN}} = 2.76$ *TeV*, Journal of High Energy Physics 06 (2015) 190 [cited by 42 records].
3. B. Abelev et al. [ALICE Collaboration], *Searches for transverse momentum dependent fluctuations of flow angle and magnitude in Pb–Pb collisions at* $\sqrt{s_{\rm NN}} = 2.\ 76$ *TeV*, in preparation for JHEP.
4. B. Abelev et al. [ALICE Collaboration], *Measurement of correlations between event-by-event fluctuations of flow harmonics in Pb-Pb Collisions at* $\sqrt{s_{\rm NN}} = 2.76$ *TeV*, in preparation for Phys. Rev. Lett.
5. B. Abelev et al. [ALICE Collaboration], *Anisotropic flow of charged particles in Pb-Pb collisions at* $\sqrt{s_{\rm NN}} = 5.02$ *TeV*, in preparation for Phys. Rev. Lett.

Other Publications

1. Y. Zhou et al., *Anisotropic distributions in a multi-phase transport model*, arXiv:1508.03306, submitted to Phys. Rev. C.
2. Y. Zhou et al., *Investigation of possible hadronic flow in* $\sqrt{s_{\rm NN}} = 5.02$ *TeV p-Pb collisions*, Phys. Rev. C, 91, 064908 (2015).
3. A. Bilandzic, C. Christensen, K. Gulbrandsen, A. Hansen and Y. Zhou, *Generic equations for anisotropic flow analysis with multi-particle azimuthal correlations*, Phys. Rev. C, 89, 064904 (2014).
4. K. Xiao, Y. Zhou et. al. *Effects of elliptic flow and resonance decay process on the Kurtosis of net baryon distributions*, C. Phys. C, 35 (5), 467 (2011).
5. Y. Zhou et. al. *Higher Moments of Net-Baryon Distribution as Probes of QCD Critical Point*, Phys. Rev. C, 82, 014905 (2010).

Conference Proceedings

1. Y. Zhou et al., *Is hadronic flow produced in p–Pb collisions at the Large Hadron Collider?*, arXiv:1508.06160, to be published in Eur. Phys. J. Web of Conferences.
2. Y. Zhou [ALICE Collaboration], *Searches for* p_{T} *dependent fluctuations of flow angle and magnitude in Pb–Pb and p–Pb collisions*, Nucl. Phys. A 931 (2014) 949-953.
3. Y. Zhou [ALICE Collaboration], *Anisotropic flow of identified particles in Pb–Pb collisions at* $\sqrt{s_{\mathrm{NN}}} = 2.76$ *TeV with the ALICE detector*, J. Phys. Conf. Ser. 509 (2014) 012029.
4. Y. Zhou [ALICE Collaboration], *Azimuthal correlations in Pb-Pb and pp collisions measured with the ALICE detector*, arXiv:1201.4671 (2012).
5. Y. Zhou [ALICE Collaboration], *Higher harmonic anisotropic flow measurements of charged particles at 2.76 TeV with the ALICE detector*, Acta Phys. Polon. Supp. 5 (2012) 407-412.
6. Y. Zhou et. al. *Event-by-event fluctuation of net-baryon distribution and its higher order cumulants*, Int. J. of Mod. Phys. E 19, 1866 (2010).
7. Y. Zhou et. al. *Charged particle fluctuation in Au+Au collision*, Chinese Phys. C 34 (9), 1436 (2010).

Acknowledgments

First and foremost I would like to thank my promotor and supervisor Prof. Dr. Raimond Snellings for guiding me through my PhD years. He was always patient with my silly and naive questions about flow, and many not-smart-at-all ideas I had. I still remember the 'glory days' in the beginning of my PhD when he taught me everything about flow. Later on he became more busy but still the discussions with him always helped me a lot! It's my pleasure to work with a flow expert like him. I hope that I too will one day be as good researcher as he is.

I would also like to thank Dr. Panos Christakoglou for acting as my supervisor in the final stage of my PhD. I know it's a hard work and I have no doubt that the thesis will not be there without your supervision, no need to mention many meetings on the thesis at Saturday nights. From you, I also learn how to be a good physicist and father at the same time.

I can not forget another 'supervisor' Dr. Ante Bilandzic (Mr. B) who answered all my questions in mathematics. Thanks for teaching me how to write code (perhaps my programming could be better if ...), and how to use Q-Cumulant and Generic framework. I was glad to have you as an officemate twice (in Amsterdam and Copenhagen) and also have you as my best friend (although we almost disagree with each other for everything).

Thanks for the reading committee members, namely Dr. Paul Kuijer, Prof. Dr. Marcel Merk, Prof. Dr. Thomas Peitzmann, Prof. Dr. Bert Schellekens. Many thanks also go to my colleagues and friends at Nikhef and Utrecht University. Thanks to my formal master students Redmer, who worked with me for the ϕ meson flow analysis and proved that he could get ALICE Preliminary during his master! Late on he also does a great job on jet v_2 analysis, which is another excellent work. Thanks Zhan for many nice discussions on everything, and the nice Blast-wave codes which are widely used in ALICE now.

Thanks to Allessandro, Alberto, Alex, Alis, Andre, Andrea, Astrid, Carlos, Chiara, Davide, Deepa, Emy, Geert-Jan, Grazia, Hongyan, Jacopo, Kees, Marco, Marek, Marta, Martijn, Michiel, Merijn, Mikolaj, Misha, Naghmeh, Naomi, Raoul, Sandro, Sarah, Thomas and Ton.

Special thanks go to Jurgen, Sergei, Ilya, Constantin, Michael, Jan Fiete, Anthony, Francesco, Ionut, Jaap for many helpful discussions in Flow Physics Analysis Group in ALICE.

Thanks to Prof. Nu Xu, Prof. Feng Liu, Prof. Daicui Zhou for many great discussions. Thanks to the other colleagues and friends in Wuhan for many great chats and discussions. Thanks to Dr. Huichao Song, Dr. Xiangrong Zhu for the collaborates. I would like to thanks Dr. Jean-Yves Ollitrault and Prof. Ulrich Heinz for the discussions on hydrodynamic calculations.

Many thanks to Jens-Jørgen (JJ) for offered me a great job and life in Copenhagen, thanks to Hans, Annette, Børge, Ian, Christian (coding magician), Kris, Valentina, Xi-

aoren, Christian (II), Katarina, Lais for allowing me to work as a postdoctoral researcher for a year without a phd. Working environment could not be better to have you around.

Thanks to all my friends whose names are not listed here.

At the end, most importantly, thanks to Li and Yudie for their infinite supports. Thanks to my parents for your love.